EFFECT OF PHONON TRANSPORT ON THE SEEBECK COEFFICIENT AND THERMAL CONDUCTIVITY OF SILICON NANOWIRE ARRAYS

BY

JYOTHI SWAROOP SADHU

DISSERTATION

Submitted in partial fulfillment of the requirements
for the degree of Doctor of Philosophy in Mechanical Engineering
in the Graduate College of the
University of Illinois at Urbana-Champaign, 2014

Urbana, Illinois

Doctoral Committee:

Professor Placid Ferreira, Chair
Professor Sanjiv Sinha, Director of Research
Professor David G. Cahill
Professor Xiuling Li

ABSTRACT

Thermoelectrics enable solid-state conversion of heat to electricity by the Seebeck effect, but must provide scalable and cost-effective technology for practical waste heat harvesting. This dissertation explores the thermoelectric properties of electrochemically etched silicon nanowires through experiments, complemented by charge and thermal transport theories. Electrolessly etched silicon nanowires show anomalously low thermal conductivity that has been attributed to the increased scattering of heat conducting phonons from the surface disorder introduced by etching. The reduction is below the incoherent limit for phonon scattering at the boundary, the so-called Casimir limit. A new model of partially coherent phonon transport shows that correlated multiple scattering of phonons off resonantly matched rough surfaces can indeed lead to thermal conductivity below the Casimir limit. Using design guidelines from the theory, silicon nanowires of controllable surface roughness are fabricated using metal-assisted chemical etching. Extensive characterization of the nanowire surfaces using transmission electron microscopy provides surface roughness parameters that are important in testing transport theories. The second part of the dissertation focuses on the implications of increased phonon scattering on the Seebeck coefficient, which is a cumulative effect of non-equilibrium amongst charge carriers and phonons. A novel frequency-domain technique enables simultaneous measurements of the Seebeck coefficient and the thermal conductivity of nanowire arrays. The frequency response measurements isolate the parasitic contributions thus improving upon existing techniques for cross-plane thermoelectric measurements. While the thermal conductivity of nanowires reduces significantly with increased roughness, there is also a significant reduction in the Seebeck coefficient over a wide range of doping. Theoretical fitting of the data reveals that such reduction results from the annihilation of phonon drag in nanowires due to phonon boundary scattering. By exploring the effect of surface roughness

and employing lattice non-equilibrium theories, the measurements are able to distinguish between long wavelength phonons that contribute to phonon drag and shorter wavelengths that contribute to heat conduction near room temperature. Phonon drag quenching in nanostructures has implications beyond silicon and this thesis paves the way toward spectrally selective phonon scattering for improving nanoscale thermoelectrics.

ACKNOWLEDGMENTS

I would like to thank my research advisor, Prof. Sanjiv Sinha for positively impacting my life, both on academic and personal fronts. I feel extremely fortunate to have shared good rapport with such gifted individual that paved way for a fruitful and satisfying graduate career. I thank Prof. Sinha for always having confidence in me amidst the inevitable impediments that accompany experimental research. I greatly appreciate him for taking time to meet with me regularly that ensured I never got bogged down at any step in my thesis work. I am greatly indebted to Prof. David G. Cahill for helping me inculcate 'old school' principles of sound scientific research. His critical appraisal of my work and the positive feedback he provided were valuable in greatly improving the quality of my thesis. I would like to thank my PhD dissertation committee members Prof. Placid Ferreira and Prof. Xiuling Li for their direct involvement in my research projects and taking interest in my progress.

I was also fortunate to be a part of well-organized and highly collaborative research group. I want to thank Tian Hongxiang whose contribution was instrumental in keeping my project work rolling. I could not thank him enough for the many all-nighters we pulled off in cleanroom for my projects, reminiscent of Walt-Jesse bonding from the series 'Breaking Bad'. I will always treasure my interactions with Marc Ghossoub who immensely helped me with understanding the fundamentals when I was relatively new to the field. My discussions with Marc were always marked with intellectual resonances. I want to acknowledge the support of Jun and Krishna who were very cooperative with troubleshooting various processing bottlenecks I faced in my research. Special acknowledgements to my fellow graduate students who worked with me during the course of ARPA-e project - Karthik Balasundaram, Bruno Azeredo, Keng Hsu, Joseph Feser. I was lucky to have the

opportunity to work alongside this interdisciplinary team of self-driven and highly intelligent individuals.

I want to acknowledge my social support group who made my life at UIUC immensely enjoyable. I will cherish the company of Nishanth and Sushil in our several cross-country road trips, summer cricket and Jerusalem gossips. I am indebted to the 'Jerusalem guy' (I do not know his name) who fed me daily for four years. A consummate graduate life should always have arts married to technical research. And for that, I would like to acknowledge my dance partners Honey and Foxy for joyful social outings.

Finally, dissertation acknowledgments are not complete without thanking parents. My parents have been always supportive of my brave decision to dive into PhD. I consider their biggest contribution to my PhD was to never ask uncomfortable questions that a PhD student does not enjoy to answer.

TABLE OF CONTENTS

LIST OF FIGURES viii

CHAPTER 1 NANOSTRUCTURED THERMOELECTRICS 1
1.1 Motivation and Background 1
1.2 Size effects on thermal conductivity of silicon 4
1.3 Thermal conduction in rough wires below the Casimir limit . . 8
1.4 Seebeck effect in silicon 9
1.5 Organization 13

CHAPTER 2 MODELING OF PHONON TRANSPORT IN SURFACE DISORDERED NANOSTRUCTURES 15
2.1 Multiple Scattering theory 17
2.2 Dispersion models in nanowires 20
2.3 Multiple scattering in rough nanowires 23
2.4 Thermal conductance of rough nanowires 30
2.5 Results and Discussion 32
2.6 Effects of two-dimensional roughness 36
2.7 Conclusion 41

CHAPTER 3 ROUGHENED NANOWIRE ARRAYS USING METAL ASSISTED CHEMICAL ETCHING 43
3.1 Process overview 44
3.2 Nanowire Roughening 46
3.3 MacEtch on degenerate silicon 49
3.4 Doping control of NWAs 51

CHAPTER 4 FREQUENCY DOMAIN MEASUREMENTS OF THERMOELECTRIC PROPERTIES 57
4.1 Introduction 57
4.2 Principle of Measurement 58
4.3 Limitations in high diffusivity media 60

CHAPTER 5 THERMOELECTRIC MEASUREMENTS OF NANOWIRE ARRAYS 64
5.1 Thermal conductivity with roughness 64

5.2 Differential measurements of NWAs 67
5.3 Data reduction and fitting 69
5.4 S and k measurements on bulk Si 73
5.5 S and k measurements of rough SiNWs 74
5.6 Electrical measurements of SiNWs 77
5.7 Discussion 81

CHAPTER 6 THEORY OF THERMOPOWER AND PHONON DRAG 83
6.1 Formal theory using Boltzmann transport equation 83
6.2 Diffusion component of S 85
6.3 Phonon Drag using Π-approach 86
6.4 Effect of boundary scattering on drag 91

CHAPTER 7 CONCLUSIONS AND FUTURE WORK 94

APPENDIX A HEAT DIFFUSION SOLUTION AT INTERFACES . 98
A.1 Line Heater assumption 100

REFERENCES 102

LIST OF FIGURES

1.1 (a) Schematic of thermoelectric module with p-type and n-type junction operating as a heat engine. (b) Conversion of the thermoelectric figure of merit ZT to efficiency as a function of source temperatures. 2
1.2 Summary of enhancements in ZT of nanostructured materials since 1993. Reproduced from Ref. [1] 3
1.3 (a) Spectral distribution of phonons showing the density of states in silicon (b) Dependence of phonon mean free path with phonon frequency for different phonon scattering processes. 5
1.4 The mean free paths of electrons and phonons contributing to cumulative electrical and thermal conductivity respectively in silicon at room temperature. 5
1.5 Experimentally measured thermal conductivity of silicon patterned into various nano-architectures. The dotted line represents the Casimir limit of thermal conductivity in Si. . . 7
1.6 (a) The power factor peaks at a carrier concentration $\sim 10^{19}$ cm^{-3} in silicon. (b) Strategies for enhancing the diffusion component of Seebeck coefficient. 11

2.1 Transmission electron micrographs of the surface of (a) a smooth nanowire and (b) a roughened nanowire, both fabricated using metal assisted chemical etching. The scale of TEM micrographs is 10 nm. Phonons in the smooth wire are diffusely scattered at the boundary. The enhanced roughness in the roughened wire leads to partially coherent transport where the scattered wave fronts undergo multiple interactions. 16
2.2 Multiple scattering problem for two point scatterers located at r_1 and r_2 17

2.3 (a) Lowest lying transverse modes of a 3 nm nanowire calculated by lattice dynamics. (b) Density of modes calculate from complete LD simulations are compared with the parabolic dispersion equation in Eqn. 2.19. (c) The ratio of sound velocity in NWs to bulk shows the confinement effects are not significant for NW diameter >10 nm. (d) Casimir limit of thermal conductivity of SiNWs calculated using parabolic approximation closely match the calculation from LD from Ref. [2]. 22
2.4 Acoustic phonon dispersion for the lowest-lying modes under rigid (in red) and stress-free (in blue) conditions at the nanowire surface. 23
2.5 (a) The logarithm of attenuation length plotted on phonon dispersion plot shows (A) quasi-ballistic transport for modes near fundamental branches (B) diffuse modes and (C) non-conducting modes near the zone center with high transverse wavenumbers. (b) The boundary scattering transmission coefficient for longitudinal modes averaged over number of modes is shown for wire 1 (σ=0.8 nm, L_c=300 nm), wire 2 (σ=2.5 nm, L_c=90 nm) and wire 3 (σ=2.5 nm, L_c=30 nm) for a 50 nm wire representing transition from smooth to very rough surface. The Casimir transmission ($=d/L$) and the Umklapp transmission($=\Lambda_u/L$) are also shown. 28
2.6 Dependence of thermal conductivity at 300 K on (a) roughness height at different correlation lengths (b) correlation length at different roughness heights for a 50 nm wire, 2μm in length 33
2.7 Temperature trend of thermal conductivity of EE SiNW for 50 nm (σ = 2.2 nm, L_c = 21 nm), 98 nm (σ = 2.2 nm, L_c = 70 nm) and 115 nm (σ = 2 nm, L_c = 86 nm) diameter wires. The experimental data is from Ref [3]. 34
2.8 Temperature trend of thermal conductivity of EBL wires using σ = 7.4 nm and L_c = 400 nm for Wire-1 (120$\times$ 41 nm^2 and $L = 4\mu m$) and Wire-2 (86$\times$62 nm^2 and $L = 7\mu m$). The data is from Ref [4]. (*Inset:* Temperature trend of thin VLS wires compared against data from Ref [5]) using $\sigma = 1$ nm, $L_c = 80$ nm). 35
2.9 Schematic of the the longitudinal section (a) and the cross-section (b) of a rough nanowire showing the relevant roughness scales used in the model. 37

2.10 The effect of longitudinal roughness correlation length (L_c) and the circumferential roughness correlation angle (Φ_c) on thermal conductivity of a 40 nm diameter wire at 300 K. The RMS height of roughness is assumed to be 2 nm and wire length to be 2 μm with a Dirichlet boundary condition . 39
2.11 Effective transmission of the phonon spectrum $N(\omega)\overline{T}(\omega)$ for the cases L_c/a=2 and L_c/a=4. Solid lines represent angular correlation of $\Phi_c = 22.5^0$ while dashed lines represent $\Phi_c = 60^0$. The RMS height is fixed at 1.5 nm with the diameter at $a = 40$ nm. 40
2.12 The effect of circumferential roughness correlation on thermal conductivity of a wire. The RMS height of roughness is 2 nm, longitudinal correlation length is 80 nm and wire length of 2 μm. The contribution of LA modes (in dash-dot lines) and TA modes (in dashed lines) are also shown for the two cases. 41

3.1 (a) Thermal dewetting pattern of silver droplets after annealing 10 nm Ag film for 350^0C for 4 hours. (b) The gold mesh fabricated by Ag lift off serves as pattern for subsequent etching. (c) Etching in the solution of HF and H_2O_2 produces vertically aligned nanowire array (d) The Au droplets are sputtered on the nanowire sidewalls and a subsequent etching for short time produces controllable surface roughness on the nanowires as shown in HR-TEM images. The scale bars represent a length of (a) 500 nm (b) 2 μm (c) 2 μm (d) 2 nm 45
3.2 Bright field transmission electron micrographs of nanowires obtained by post-roughening process (etch times increasing from left to right: 2, 10, 16 and 20 seconds respectively); the scale bar is 10 nm). 47
3.3 (a) The surface roughness profiles of wires for different etching times is obtained by stitching several HR-TEM images (b) Average RMS height of post-roughened nanowires as a function of etching time. Different symbols represent the wires from different batches. (c) Height-height correlation function $G(\rho)$ for three different roughness profiles. . . . 48
3.4 The degree of porosity of degenerately p-doped NWs decreases with dilution of HF solution as indicated in low mag and corresponding HRTEM images for [HF]:[H_2O_2] of (A) 10:1 (B) 20:1 (C) 30:1. A non-porous crystalline nanowire (D) is shown as comparison. 50

3.5 The porosity of the wire progressively decreases along the etching direction. (I) shows the low-magnification images of the wire from wire tip (d) to bottom (a). (II) shows the corresponding HRTEM images with (d) to (a) representing the etch direction. We also observe the boundary becomes smoother towards the bottom of the wire. The scale bars in (I) and (II) are 50 nm and 5 nm respectively. 51
3.6 Schematic showing the dopant depth profiling of nanowire arrays. The etching ions are is Cesium or oxygen ions for profiling n-type or p-type NWs respectively. 53
3.7 The SIMS depth profile of the boron-doped nanowire arrays, doped with PECVD barrier layer of thickness labeled against each profile. The arrows represent the length of NW array measured from SEM before the profiling. 54
3.8 (a) SEM image showing the nanowire tips exposed after RIE etching of spin-on glass spun over the NW array. The scale bar is 1μm. (b) SIMS depth profile of NW array of length 850 nm. 55
3.9 (a) Electrical resistance measurements before (a) and after (b) tip-doping shows improvement in contact resistivity by four orders. 56

4.1 Principle of differential measurements shown in (a) schematic and (b) simulation of temperature and voltage signals for 'ref' and 'NW' samples. 59
4.2 (a) Steady periodic temperature simulation in 'ref' and 'NW' sample in highly diffuse substrate. (b) The penetration depth in silicon as a function of temperature at heating frequency of 200 Hz. (c) The measured data of power normalized Seebeck voltage at several temperatures. . . 61
4.3 Simulations showing the deviation in temperature rise of heater using line heater assumption relative to finite heater of length 600μm at (a) 300 K and (b) 80 K. The deviation in the fits produced by line heater assumption to the measured data of (c) heater temperature rise and (d) Seebeck voltage. 63

5.1 (a) Thermal conductivity of SiNWs measured using time-domain thermoreflectance as the function of RMS roughness height of the nanowires. The Casimir limit of thermal conductivity for the NWs of average diameter 100 nm - 150 nm is also shown. (b) Thermal conductivity of single nanowire with various roughness statistics measured using microfabricated platform. 65

5.2 Schematic showing the fabrication flow of measurement platform on SOG-filled NW arrays; each step detailed in Sec. 5.2.1 67
5.3 Schematic showing the platform for the simultaneous measurement of Seebeck coefficient and thermal conductivity on the spin-on glass filled nanowires 68
5.4 (a) The response of the temperature rise of the heater with heating current frequency at 300 K and 80 K. The sample with nanowire array is labeled 'NW' and the sample on substrate is labeled Ref. The heating power P used at these temperatures is also shown. (b) The response of the measured Seebeck voltage with heating current frequency at 300 K and 80 K. 69
5.5 The frequency response of heater temperature (T_h) and measured Seebeck voltage (V_s) for bulk Si. The simulated temperature rise at substrate (T_{sub})is used to fit the Seebeck voltage trend. 70
5.6 The measured Seebeck voltage across several temperatures with heating current frequency. The solid lines represent the fits produced by $V_s = S_{sub}T_{sub}$. 71
5.7 The heater temperature rise and the Seebeck voltage for bulk silicon of different carrier types (a) n-type and (b) p-type. 71
5.8 Seebeck coefficient of (a) non-degenerate Si (N_a= 2×10^{17} cm^{-3}) and (b) degenerate Si (N_a= 2×10^{17} cm^{-3}) is shown in solid squares. The diffusion component calculated from Eqn. 5.3 is represented in solid line and the phonon drag extracted is shown in solid triangles. The open symbols in (a) show comparison with classic literature [6, 7] 75
5.9 The Seebeck coefficient of NW arrays with different surface morphology at similar doping concentrations. The theoretical fits were obtained using Eqn. 5.3 using the doping concentration obtained from SIMS. (Inset shows the thermal conductivity of the NW arrays). 76
5.10 Surface depletion model for SiNWs showing the radius of undepleted region (r_{elec}) in comparison to their physical radius (r_{phys}) against dopant concentration. The shaded region indicates the NW doping range studied in this paper. We extracted the data in this figure from Ref. [8]. 78
5.11 (a) SEM micrograph of single NW measurement platform. The scale bar is 3 μm. (b) 4-point probe electrical measurements on single nanowire. 79
5.12 Extracted mobility from the two-point resistivity measurements of porous SiNW arrays. The literature values for porous Si mobility are taken from Ref.[9] 80

5.13 The Seebeck coefficient of NW arrays measured across several doping concentrations. The dashed lines represent the diffusion component, S_d calculated theoretically using Eqn. 5.3. The open symbols represent data for bulk Si. 81
5.14 The Seebeck coefficient (only the diffusion component S_d and the power factor ($S^2\sigma$T)across various doping levels. . . . 82

6.1 (a) Energy level diagram of n-type Si with carrier concentration $N_d = 5 \times 10^{19}$ cm^{-3}. The effective density of states (represented by filled region) is calculated using $g(E)f(E)$ (b) The exact scattering rates at this doping level (only ADP and II processes are shown here) are fitted for the power law dependence r. 87
6.2 Spectral dependence of the rate of momentum exchange R($\mathbf{q}$) by electron-phonon interactions calculated using Eqn. 6.17. 90
6.3 Spectral dependence of the net crystal momentum change in bulk Si for degenerate and non-degenerately doped Si calculated using Eqn. 6.18. 91
6.4 The radial distribution of crystal momentum in wires of radii 10μm, 1μm and 100 nm calculated using Eqn. 6.21. The color bar shows the magnitude of crystal momentum relative to crystal momentum P_0 in absence of boundaries. . . 93
6.5 The effect of boundary scattering on the transfer of total crystal momentum $\langle P \rangle$ in comparison to that in the absence of boundaries $\langle P_0 \rangle$ with varying wire radius. 93

A.1 Schematic of n-layered medium for frequency domain measurements. The origin of the coordinate system is located at the heater. 98

CHAPTER 1

NANOSTRUCTURED THERMOELECTRICS

1.1 Motivation and Background

The second law of thermodynamics states that it is impossible to build a perfect heat engine which converts all the available energy from a heat source into useful work. All irreversible heat engines between two heat reservoirs are less efficient than an ideal Carnot engine operating between the same reservoirs. Thus, every heat engine in the world rejects energy in the form of heat, with the quantity of rejected heat dependent on the reservoir temperatures. Heat engines that produce 90% of the world's power typically only convert less than 40% into electricity or useful work. The US Department of energy estimates that ∼57% of the annual energy produced in the US alone is rejected in the form of waste heat. Over 2 TW of such wasted energy is available as low quality heat sources (40^0C-250^0C). These heat sources are available at every scale - from microprocessors to car engine exhausts and even as geothermal energy a few miles beneath the earth's surface. Assuming a Carnot engine of 30% efficiency operating between a heat source at 150^0C and a sink at room temperature, 0.6 TW of work can be ideally recovered from waste heat. Thus, reclaiming even few percent of the energy in waste heat provides a compelling pathway toward energy efficiency.

Converting low quality heat into electricity presents a difficult technical problem since proven steam-based Rankine cycles are no longer operable at these temperatures. Compared to vapor cycles, thermoelectric materials enable solid state conversion of heat to electricity and can operate at the low temperatures relevant for waste heat harvesting. Thermoelectric materials utilize Seebeck effect to convert a temperature gradient to electric voltage. Silicon based thermoelectrics is technologically advantageous in that silicon

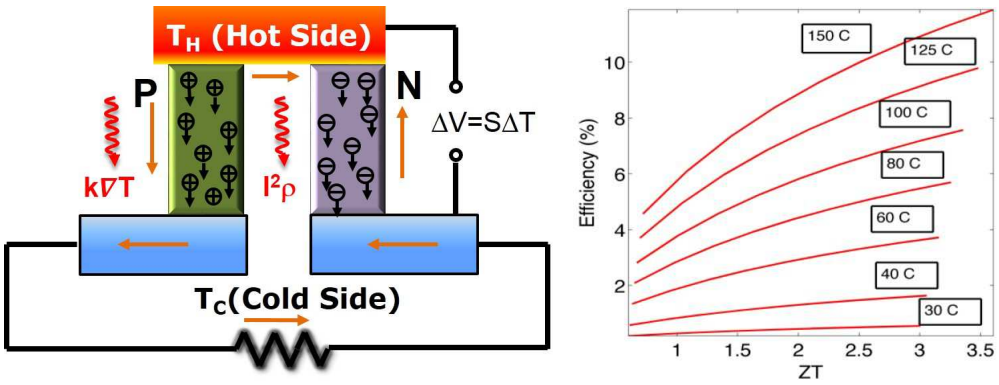

(a) (b)

Figure 1.1: (a) Schematic of thermoelectric module with p-type and n-type junction operating as a heat engine. (b) Conversion of the thermoelectric figure of merit ZT to efficiency as a function of source temperatures.

enjoys an economy of scale and an established processing knowhow. However a poor conversion efficiency ($< 1\%$) compared to vapor-based heat engines has hampered the use of silicon as thermoelectric materials. This poor efficiency in silicon stems from the high thermal conductivity of silicon which makes it difficult to sustain a temperature gradient big enough to generate a useful voltage. Thermoelectric efficiency is generally quantified by the thermoelectric figure of merit ZT [10], defined as $S^2\sigma T/k$ where S is the Seebeck coefficient, σ is the electrical conductivity and k is the thermal conductivity at temperature T. The figure of merit ZT signifies that a 'good' thermoelectric material should have high Seebeck coefficient with minimal irreversible losses in form of Joule heating ($\sim 1/\sigma$) and heat conduction across the material ($\sim k$). Figure 1.1 (a) shows a typical thermoelectric heat engine made of two dissimilar materials (p-type and n-type semiconductors as an example) highlighting the energy losses. For bulk silicon at optimal doping, ZT at room temperature is as low as 0.03 due of its high thermal conductivity (140 W/mK) rendering it useless for thermoelectrics. The conversion of ZT to thermoelectric efficiency is given in Fig. 1.1 (b).

The challenge in developing efficient thermoelectrics lies in the fact that the three thermoelectric properties (S, ρ and k) are mutually related. In bulk materials, for instance, increase in the carrier density n leads to an increase in electrical conductivity, but reduces the Seebeck coefficient. Thus, inde-

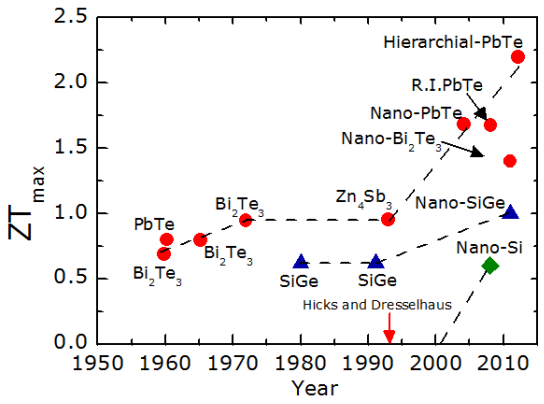

Figure 1.2: Summary of enhancements in ZT of nanostructured materials since 1993. Reproduced from Ref. [1]

pendent control of the thermoelectric properties is the primary requisite for efficient thermoelectrics. The seminal work by Hicks and Dresselhaus [11, 12] in 1993 theoretically claimed that nanostructured materials have enhanced thermoelectric figure of merit due to increased power factor $S^2\sigma$. This independent control of power factor derives from the modification of electronic density of states in quantum confined structures. These important findings spurred extensive research on the possibility of using sub-10 nm structures for thermoelectrics, but the experimental realization of the enhanced power factor is still debated [13, 14, 15]. However, nanostructures have mainly benefited from the reduced lattice thermal conductivity by increased scattering of heat conducting phonons from nanoscale boundaries. Henceforth, the widely pursued strategy for developing efficient thermoelectrics has been to reduce the lattice thermal conductivity by nanostructuring without affecting the power factor. Several review articles summarized the progress of nanostructured thermoelectrics over the past decade in the material systems that include II-VI based nanostructures [16, 17], silicon-germanium alloys [18], bulk nanostructured materials [19], superlattices and nanoparticle embedded semiconductors [20]. We discuss the advances in silicon-based thermoelectrics in the next section with a specific focus on the reduction in the lattice thermal conductivity of silicon with nanostructuring.

1.2 Size effects on thermal conductivity of silicon

In this section, we briefly discuss the fundamentals of phonon transport pertinent to thermal conductivity of silicon. In Si, the lattice vibrations (phonons) contribute to majority of the heat conduction. The phonon thermal conductivity is given by

$$k = \frac{1}{3} \sum_{\alpha} \int_{\omega} C_{\omega} v_{\omega} \Lambda_{\omega} \, d\omega \tag{1.1}$$

where C is the specific heat of the phonon mode, v is the phonon group velocity and Λ is the phonon mean free path, all parameters are function of phonon frequency. The summation is over all possible phonon mode polarizations (α) that include transverse acoustic (TA), longitudinal acoustic (LA), transverse optical (TO) and longitudinal optical phonon modes (LO). The specific heat capacity is given by $C_{\omega} = \hbar\omega D(\omega) dN/dT$ where $D(\omega)$ is phonon density of states and N is the phonon population of mode (ω,$\mathbf{k}$). Figure 1.3 shows the spectral distribution of the phonon density of states in silicon, distinguishing the frequency regimes of acoustic and optical phonons. The density of states for low frequency acoustic phonons $\propto \omega^2$ in bulk Si. The phonon group velocity v depends on the dispersion relation of phonons. For nanostructures of critical size greater than 30 nm, the specific heat capacity and the group velocity of the phonon modes remain close to bulk silicon [2].

The mean path of phonons varies widely with phonon frequency [21] and the understanding of phonon mean free path is evolving over the past two decades. The initial understanding of the 'dominant' mean free path of phonons that contribute to the thermal conductivity was based on the kinetic model. Using the linear Debye dispersion ($\omega = c\mathbf{k}$) and thermal conductivity data of bulk Si, the kinetic model estimates the dominant phonon mean free path ~43 nm at room temperature [22]. The critical drawback of the kinetic model lies in its assumption of frequency independent phonon mean free path, also called the grey approximation. The kinetic model severely underestimates the MFPs of the phonons for several reasons (a) Debye dispersion model overpredicts the average group velocity of phonons and (b) the Debye cut-off frequency used for heat capacity C overpredicts the contribution of optical phonons to the thermal conductivity at room temperature. Ju et.al.[23] estimated the effective MFP of phonons ~300 nm at room temperature using

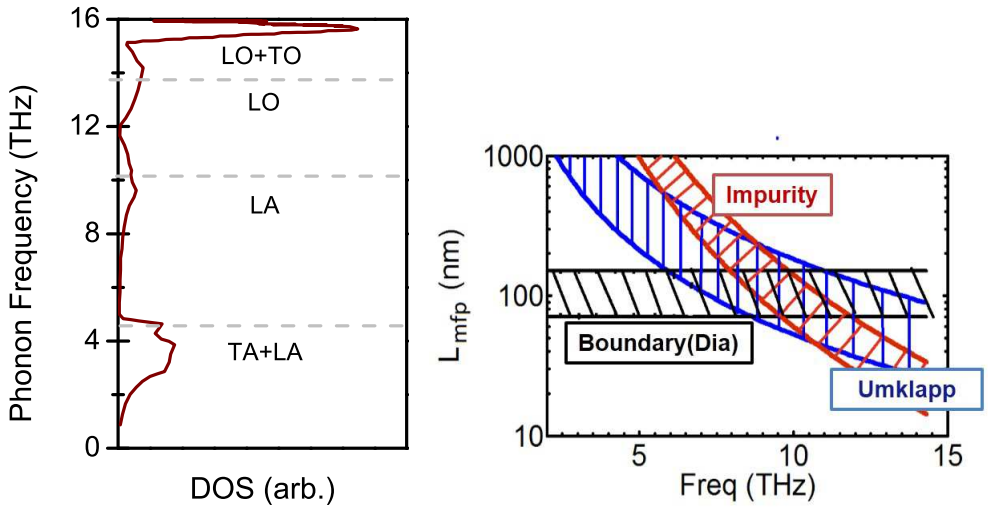

Figure 1.3: (a) Spectral distribution of phonons showing the density of states in silicon (b) Dependence of phonon mean free path with phonon frequency for different phonon scattering processes.

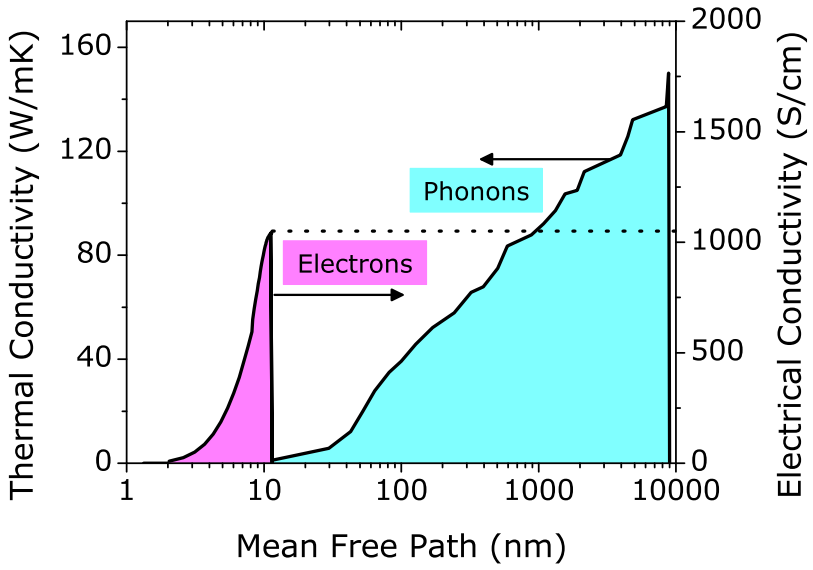

Figure 1.4: The mean free paths of electrons and phonons contributing to cumulative electrical and thermal conductivity respectively in silicon at room temperature.

thin-film thermal conductivity data and complete phonon dispersion models. In 2011, the first-principles calculation of phonon mean free path by Esfarjani et. al. [24] showed that the MFPs span over five orders of magnitude from 1 nm to 100μm in Si at room temperature. This work showed that about half of the thermal conductivity comes from MFPs larger than 1 μm. Several recent thermal conductivity spectroscopic measurements [25, 26, 27] confirm the broadband distribution of MFPs of heat conducting phonons and are in quantitative agreement with the first-principles calculations.

Figure 1.4 plots the cumulative thermal conductivity and electrical conductivity as a function of phonon MFP and electron MFP in Si at room temperature. The specific contributions of phonon MFPs to the thermal conductivity is obtained from first-principles calculations from Ref. [24]. The electrical conductivity as a function of electron MFPs in doped Si ($N = 1 \times 10^{19}$ cm^{-3}) is calculated using the validated electron scattering rates from the device physics literature [28, 29]. From Fig. 1.4, we observe that by introducing nanoscale boundaries of $\sim$100 nm, the phonons of larger MFPs can be suppressed by boundary scattering without critically affecting the electronic MFPs. Thus, nanostructuring provides independent control of the thermal conductivity and the electrical conductivity in silicon paving the way to efficient silicon-based thermoelectrics.

1.2.1 Casimir limit of thermal conductivity

In low dimensional structures, the mean free path of phonons is suppressed by phonon boundary scattering. Figure 1.3 (b) plots the mean free path of individual phonon scattering processes as a function of phonon frequency. We observe that the MFPs of acoustic phonons responsible for majority of heat conduction at room temperature are predominantly limited by the size of crystal.

Completely incoherent scattering of phonon modes from the boundaries leads to the limit of thermal conductivity in low dimensional structures called the Casimir limit [30]. This limit of phonon boundary scattering assumes complete thermalization of incident phonons at the boundaries of a crystal

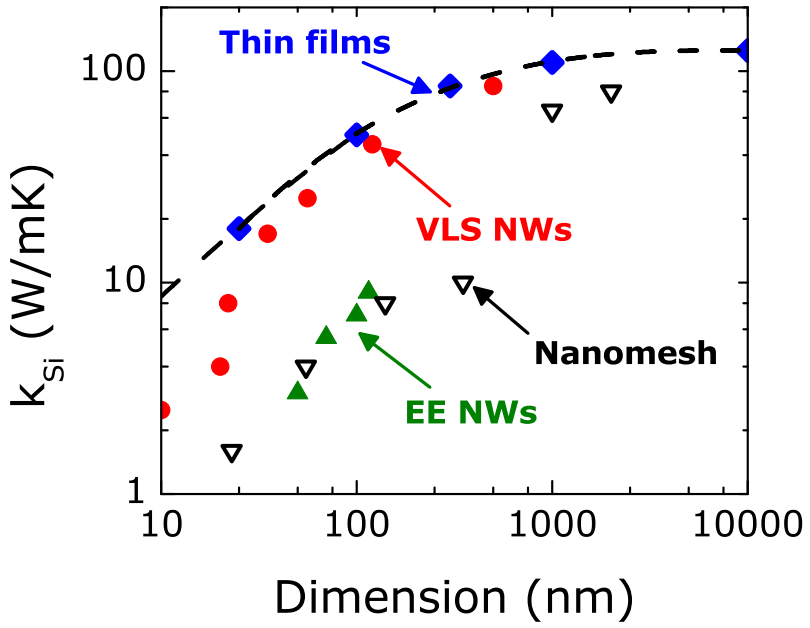

Figure 1.5: Experimentally measured thermal conductivity of silicon patterned into various nano-architectures. The dotted line represents the Casimir limit of thermal conductivity in Si.

yielding a phonon mean free path comparable with the crystal dimensions. For a wire geometry, the theory yields a phonon mean free path equal to the wire diameter. This limit of thermal conductivity assumes all phonon modes, independent of their frequency, have MFP due to the boundary scattering that equals the critical dimension of the structure. The dotted line in Fig 1.5 shows the Casimir limit as a function of crystal dimension. The experimentally measured thermal conductivity data of thin films [31, 32] and VLS nanowires [33, 5] shown in Fig. 1.5 adhere to the Casimir limit of the thermal conductivity. The critical dimensions in the thin films and the nanowires are the film thickness and the wire diameter respectively. Recent measurements on electrolessly etched nanowires [3, 4, 34] and nanomeshes [35, 36, 37] however show a significant reduction in the thermal conductivity, several times below the Casimir limit and two order reduction from bulk silicon. Eventhough these results can be seen as a remarkable breakthrough for silicon thermoelectrics, the anomalously low thermal conductivity values suggesting the breakdown of Casimir limit in these structures is puzzling. We discuss the case of reduction in k of the electrolessly etched nanowires in the next section.

1.3 Thermal conduction in rough wires below the Casimir limit

Recent measurements of the thermal conductivity of electrolessly etched silicon nanowires [3, 4, 34] claim a thermal conductivity as low as ~ 3 W/mK at room temperature for a 50 nm diameter wire. This intriguing fifty-folds reduction from the value for the bulk is well below the Casimir limit [30] and close to the amorphous limit of $\sim$1 W/mK for silicon. What is even more puzzling is that measurements on wires fabricated using electron-beam lithography and roughened using reactive-ion etching [4] do not exhibit the anomalously low thermal conductivities as the electrolessly etched wires even though their surface roughness exceeds that of the electrolessly etched wires. While further measurements are still needed to verify these results, these initial experiments draw attention to a deeper examination of the validity of the Casimir limit in nanostructures. A 50 nm diameter single-crystal silicon wire is expected to have a thermal conductivity of $\sim$20 W/mK at room temperature at the Casimir limit of boundary scattering, much higher than that reported for electrolessly etched wires.

Existing theoretical work [38, 5, 39, 40, 41] explain the reduction in thermal conductivity using different approaches. Phonon transport in the rough nanowires has been extensively studied using perturbative approaches [38, 40, 42, 43] to detailed atomistic simulations using molecular dynamics [39, 44], non-equilibrium Green function techniques [45, 46, 47] and Boltzmann transport equations [48]. Atomistic simulations [39] show that the low thermal conductivity arises due to non-propagating vibrational modes. The computations are restricted to diameters of 4 nm and do not facilitate a direct comparison with experimental data. Monte Carlo modeling of phonon transport [40] using frequency dependent surface scattering matches reasonably with data but predicts a continuously decreasing thermal conductivity with increasing roughness amplitude and contradicts the measurements on the electron-beam defined wires [4]. A subtle issue in the formulation is the use of a scattering cross-section [49] that is valid for bulk disorder. The wires, especially at a low doping, do not appear to possess any bulk disorder according to the available TEM evidence. The model also counts surface scattering twice by including the frequency independent Casimir limit along with the

frequency dependent scattering. Thus, it is difficult to ascertain if the fit to experimental data is fortuitous rather than physical.

A third model [38, 5, 41] approaches the problem through an examination of coherent effects. This applies Morse's results [50] for a disordered linear chain to obtain a mean free path for surface scattering and uses it along the lines of the DMPK theory [51]. The results explain low temperature data satisfactorily but do not address the room temperature behavior. In this dissertation, we build on such coherent transport theories [38, 41, 42] to consider multiple scattering from the boundaries in conjunction with the incoherent Umklapp scattering to understand room temperature thermal conductivity of rough silicon nanowires.

1.4 Seebeck effect in silicon

In this section, we review the understanding of the Seebeck coefficient in silicon. The practical importance of the Seebeck coefficient stems from its quadratic dependence in the power factor, $S^2\sigma$ for thermoelectric energy conversion, where σ is the electrical conductivity. The Seebeck coefficient is a measure of the open-circuit voltage generated across a material in response to a temperature difference across its ends. The voltage results both from the intrinsic diffusion of charge carriers from the hot to the cold side as well as a drag imposed on the carriers by the accompanying diffusion of phonons. The total Seebeck coefficient, S is generally expressed as the sum of the carrier diffusion (S_d) and the phonon drag (S_{ph}) components [6, 52]. We will discuss each phenomenon separately.

1.4.1 Diffusion component

The diffusion component of the Seebeck coefficient is the average energy transported by the carriers relative to the Fermi level.

$$\begin{aligned} S_d &= \frac{1}{eT}\left(\frac{\langle \tau E\rangle}{\langle \tau\rangle} - E_F\right) \\ &= \frac{1}{eT}\left[\frac{\int_{E_b}^{\infty} E g(E) v(E) \Lambda(E) \frac{df_0}{dE} dE}{\int_{E_b}^{\infty} g(E) v(E) \Lambda(E) \frac{df_0}{dE} dE} - E_F\right] \end{aligned} \tag{1.2}$$

where E_F is the reduced Fermi-level (energy at the band edge E_b is considered zero), $g(E)$ is 3D density of states, $v(E)$ is the carrier velocity and f_0 is the equilibrium Fermi-dirac distribution at temperature T. The first term in Eqn. 1.2 depends on the dominant scattering mechanism of the electrons. The electron mean-free path is generally considered proportional to the energy through the 'scattering exponent' r ($\Lambda_{e-e} \propto E^r$ or $\tau \propto E^{r-1/2}$). Increase in the scattering exponent r increases S_d. The second term in Eqn. 1.2, E_F depends on the carrier concentration. For non-degenerate Si, $E_F < -2k_bT$ and for degenerate Si, $E_F > 30k_bT$. Using these approximations, Eqn. 1.2 reduces to

$$S_d = -\frac{1}{e}\left(\frac{E_F}{T} - k_b\left(r + \frac{5}{2}\right)\right) \quad \text{when} \quad E_F < -2k_bT \tag{1.3}$$

$$S_d = \frac{\pi^2\left(r+\frac{3}{2}\right)T}{3eE_F} \quad \text{when} \quad E_F > 30k_bT \tag{1.4}$$

The Fermi level moves close the band edge (conduction band in n-type and valence band in p-type) with increase in the carrier concentration (n) reducing S_d. Figure 1.6 (a) shows the decrease of S and the increase of electrical conductivity σ with n and the power factor $S^2\sigma$ peaks at an optimal n in the semiconductors. In silicon, the power factor peaks close to a carrier concentration of 10^{19} cm^{-3}.

We now outline two strategies to enhance S_d. Changing the electronic density of states $g(E)$ by quantum confinement of carriers in one-dimensional nanostructures significantly enhances S_d [11, 12]. A second approach for enhancing S_d is selective electron filtering [53, 54, 55]. With a hot electron filter (potential barrier in a heterostructure, for instance), the 'cold' electrons are

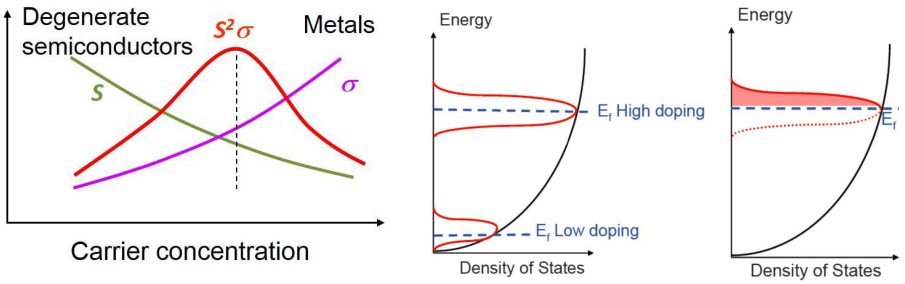

(a) (b)

Figure 1.6: (a) The power factor peaks at a carrier concentration $\sim 10^{19}$ cm^{-3} in silicon. (b) Strategies for enhancing the diffusion component of Seebeck coefficient.

selectively scattered, thereby increasing in the asymmetry between 'hot' and 'cold' electrons. This asymmetry enhances S_d by overcoming the conventional trade-off between electrical conductivity and the Seebeck coefficient. The nomenclature of 'hot' and 'cold' electrons is defined based on the electron energies above and below the Fermi level respectively as shown in Fig. 1.6 (b).

1.4.2 Phonon Drag

Amidst the advances in enhancing S_d, the role of lattice non-equilibrium in the Seebeck effect has not attracted much attention. Since the Seebeck effect arises under a temperature difference, the resulting gradient must also transport phonons. Theory considering simultaneous non-equilibrium amongst electrons and phonons shows that phonon transport enhances S through a second contribution termed the phonon drag [52, 6, 56]. The dominance of S_{ph} to the thermoelectric power was first observed in the Seebeck coefficient at low temperatures in single-crystal bulk Ge [52, 56] and Si [6, 7]. In order to explain this phenomenon, several theories on crystal momentum exchange between electrons and phonons were proposed to model the phonon drag. However, the theory of drag remains incomplete partially due to the scarce experimental data on phonon drag. Perhaps, further due to the notion that drag is inconsequential at room temperature [57] especially at the relatively

high doping of practical relevance to thermoelectrics, phonon drag remains an obscure phenomenon.

For a simple explanation of phonon drag, consider a gas of phonons with an average energy density E_{ph}/V . Using kinetic theory, the phonon gas exerts a pressure of $P = E_{ph}/3V$ on the electron gas. In presence of a temperature gradient in x-direction, the electrons experience a force

$$\frac{F_x}{V} = -\frac{dP}{dx} = -\frac{1}{3V}\left(\frac{dE_{ph}}{dT}\right)\frac{dT}{dx} \tag{1.5}$$

Under zero current conditions, this force should equal the force on the electrons by the electric field E_x, such that $F_x/V = neE_x$ where n is the carrier density. Now using the definition of the Seebeck coefficient for an open circuit system, we derive phonon drag as

$$S_{ph} = \frac{E_x}{dT/dx} = -\frac{1}{3enV}\frac{dE_{ph}}{dT} = \frac{C_{ph}}{3ne} \tag{1.6}$$

where C_{ph} is the specific heat capacity of the phonon mode per unit volume.

While this simple treatment of drag is sufficient for metals, the derivation ignores two effects pertinent to the semiconductor transport - (a) all phonons do not interact with the electron gas, unlike in the metals. Only the long wavelength phonons (λ_{ph}) that exceed half of the thermal wavelength of electrons (λ_e) satisfy the wavevector conservation for electron-phonon coupling. (b) The phonon-lattice interactions were ignored in the simple derivation. If the phonons interact with the lattice by phonon-phonon and phonon-defect scattering processes, the drift velocity of the phonons is less than that of the electron gas.

Hence, including the frequency dependent of electron-phonon (relaxation rate τ_e) and phonon-lattice interactions (relaxation rate τ_p), we can modify Eqn. 1.6 to

$$S_{ph} = \frac{1}{3ne}\int_{\omega} C_{\omega}\frac{\tau_p(\omega)}{\tau_p(\omega)+\tau_e(\omega)}\, d\omega \tag{1.7}$$

Equation 1.7 is obtained by equating the rate of momentum transfer from the electrons into a frequency group of phonons to the rate at which it is

removed by the other processes.

From Eqn. 1.7, we infer that the phonon drag is quenched with the onset of anharmonic umklapp scattering (τ_p) at higher temperatures leading to the rapid thermalization of phonons. Similarly, we expect the phonon impurity scattering to further quench phonon drag in highly doped semiconductors. Thus, a common narrative is that at room temperature and at the relatively high doping level required for practical thermoelectric energy conversion $S_{ph} << S_d$[57]. Such a narrative ignores a key attribute of the original theory of phonon drag that distinguishes between long wavelength phonons that contribute to drag and shorter wavelengths that contribute to heat conduction at room temperature. The second focus of this dissertation is to quantitatively determine the magnitude of drag in bulk silicon and in nanowires with different surface roughness scales, to identify the spectral contribution of phonons to drag.

1.5 Organization

The dissertation is organized into six chapters as follows.
In Chapter 2, we study the thermal conduction in rough silicon nanowires using a partially coherent boundary scattering model. We specifically study the correlated multiple scattering of phonons from statistically rough surfaces. Using several statistical models of roughness, we explore the effects of roughness scales on the thermal conductivity of the nanowires. Finally, we compare the existing experimental measurements with the theory.

In Chapter 3, we discuss the fabrication of roughened silicon nanowires using metal assisted chemical etching. By employing several characterization techniques, the chapter outlines the process development for controllable roughness and doping in the nanowires.

In Chapter 4, we introduce the frequency domain methods to simultaneously measure the thermal conductivity and the Seebeck coefficient of nanowire arrays. We validate the technique by measurements on bulk sil-

icon and also discuss the validity limits of the frequency domain methods.

In Chapter 5, we report the thermoelectric measurements of the silicon nanowires. We explore the dependence of thermoelectric properties with surface roughness, doping and the morphology of the nanowires.

In Chapter 6, we formally develop the theory of thermopower in silicon and separately discuss the diffusion and the drag components of the Seebeck coefficient. Using the theory of phonon drag, we explain the measured data of Seebeck coefficient in bulk silicon and nanowires. Chapter 7 summarizes our conclusions and present future directions of research for designing highly efficient silicon based thermoelectrics.

CHAPTER 2

MODELING OF PHONON TRANSPORT IN SURFACE DISORDERED NANOSTRUCTURES

Nanowires with roughened surfaces show severely lowered thermal conductivity than that predicted using Casimir's model [30] of diffuse boundary scattering. In this work, we develop a frequency dependent boundary scattering model to gain better understanding of the thermal transport in rough silicon nanowires. In this work, we build on a coherent transport theory [38, 41, 42] to consider roughness dependent multiple scattering in conjunction with Umklapp scattering. Figure 2.1 provides a visual explanation of surface scattering from nanowire surfaces. Shown are the high-resolution transmission electron micrographs of a smooth and a rough NW, typically observed electroless etched wires. As depicted schematically, the atomic scale roughness on the smooth wire scatters phonons diffusely consistent with Casimir's model. On roughening, multiple scattering events become probable especially if the roughness wave length is comparable to the phonon wave length. Figure 2.1(b) schematically depicts scattered phonon wave fronts.

While the coherent transport models are used for treating surface scattering of phonons, it should be noted that the anharmonic phonon scattering (Umklapp scattering) will destroy the coherence. The consideration of Umklapp scattering is necessary for predicting room temperature behavior but introduces the complexity of treating coherent and incoherent scattering simultaneously. Our model handles this by separating transport into distinct frequency dependent regimes where coherent or incoherent scattering dominate. We find that the multiple scattering of phonons from correlated points on the wire surface lead to strong attenuation. The mean free path from multiple scattering is shorter than that from Umklapp scattering across a range of frequencies, even at room temperature. Such scattering leads to conductivity well below the Casimir limit for high frequency phonons. However, it is not just the roughness amplitude but also the roughness correlation that

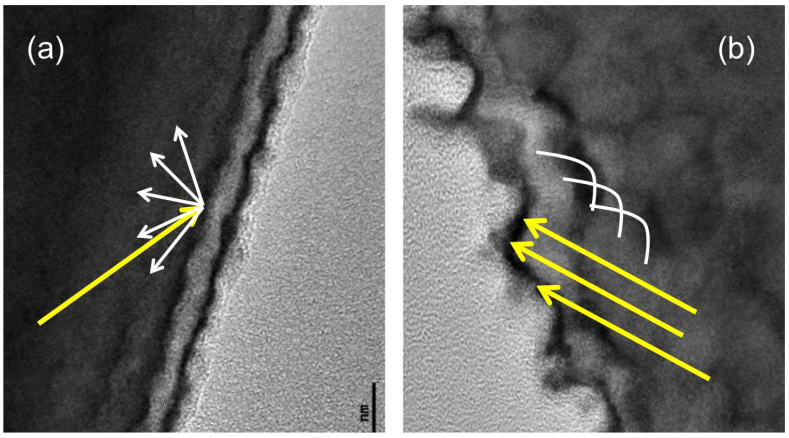

Figure 2.1: Transmission electron micrographs of the surface of (a) a smooth nanowire and (b) a roughened nanowire, both fabricated using metal assisted chemical etching. The scale of TEM micrographs is 10 nm. Phonons in the smooth wire are diffusely scattered at the boundary. The enhanced roughness in the roughened wire leads to partially coherent transport where the scattered wave fronts undergo multiple interactions.

decides the overall conductivity [58, 59].

In this chapter, we start with a brief overview of multiple scattering theory in quantum mechanical systems in Section 2.1. Since, accurate phonon dispersion relations should be used in modeling transport in one-dimensional systems, we discuss the complete solution of phonon dispersion in NWs using several models in Section 2.2. We then proceed by applying multiple scattering theory to study the transmission of the propagating phonons in a rough waveguide in Section 2.3. For this section, we consider the statistical roughness only in the longitudinal direction. We then calculate the thermal conductance in the NWs for various roughness statistics in Section 2.4 and compare the theoretical results to the available experimental data in Section 2.5. Finally, we extend our theory to include the effect of azimuthal roughness and examine the effects of this two-dimensional roughness on the phonon transmission and in turn, the thermal conductance in Section 2.6.

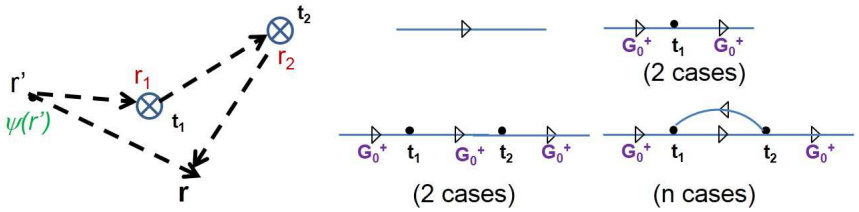

Figure 2.2: Multiple scattering problem for two point scatterers located at r_1 and r_2

2.1 Multiple Scattering theory

In this section, a brief review of multiple scattering theory is presented, a framework which will be later used to solve phonon scattering in rough waveguides in Sec. 2.3. The evolution of a wavefunction ψ propagating in free space from point r' to r with a free-space Green function operator G_0^+ is given by

$$\psi(r) = \int dr' G_0^+(r - r')\psi(r') \tag{2.1}$$

2.1.1 Point scatterers

Now consider a point scatterer of scattering strength t_1 at position $r = r_1$. The wave can travel from r' to some point r either without scattering or by scattering at r=r_1. Thus the wavefunction evolution at r is written as sum of these events as

$$\psi(r) = \int dr' G_0^+(r - r')\psi(r') + \int dr' G_0^+(r - r_1)t_1 G_0^+(r_1 - r')\psi(r') \tag{2.2}$$

In presence of two point scatterers, the wave can reach r in several possible ways as listed in Fig. 2.2. One of the ways is the wave scatters at r_1 and then at r_2 and come back to the scattering center r_1. These processes are classified as multiple scattering events since the wave interacts with the same scatterer several times. Hence, for a system of n discrete scatterers, the final wavefunction is infinite summation of all multiple scattering events given by

$$|\psi\rangle = |\phi\rangle + G_0^+ \hat{T} |\phi\rangle \tag{2.3}$$

where

$$\hat{T} = \sum_i t^i + \sum_i \sum_{j \neq i} t^i G_0^+ t^j + \sum_i \sum_{j \neq i} \sum_{k \neq j} t^i G_0^+ t^j G_0^+ t^k + \dots \tag{2.4}$$

2.1.2 Continous potentials

Instead of discrete scatterers, now consider the scattering potential V is continuous over the space. Let the wavefunction (w.f.) propagation in the space is defined by Helmoltz equation

$$\begin{aligned} (\nabla^2 + k^2)\chi(r) &= 0 \\ (\nabla^2 + k^2)\psi(r) &= V(r)\psi(r) \end{aligned} \tag{2.5}$$

where k is the wavevector, χ is the unperturbed w.f. while ψ is the w.f. in presence of perturbing potential V. Defining the Green's function G_0 for Helmoltz equation in Eqn. 2.5 as

$$(\nabla^2 + k^2)G_0(r, r') = \delta(r - r') \tag{2.6}$$

we can write express the perturbed w.f. as

$$\psi(r) = \chi(r) + \int G_0(r, r')V(r')\psi(r')\ d^3r' \tag{2.7}$$

This equation is called Lippman-Schwinger equation. Substituting Eqn. 2.7 back in place of $\psi(r')$ in the RHS of Eqn. 2.7, we get an iterative solution for the perturbed w.f. as

$$\begin{aligned} \psi(r) &= \chi(r) + \int G_0(r, r')V(r')\psi(r')\ d^3r' \\ &+ \int\int G_0(r, r')V(r')G_0(r', r'')V(r'')\psi(r'')\ d^3r'\ d^3r'' + \dots \end{aligned} \tag{2.8}$$

This equation represents the integral form of multiple scattering for continuous scattering potentials.

2.1.3 Scattering Formalism

We now apply the multiple scattering theory to quantum mechanical systems in a formal way. Again, let the unpertubed and perturbed w.f. satisfy the Schrodinger equations with Hamiltonian H_0 and eigenvalues E, given by

$$H_0|\chi\rangle = E|\chi\rangle \tag{2.9}$$

$$(H_0 + V)|\psi\rangle = E|\psi\rangle \tag{2.10}$$

we can write the Lipmann Schwinger equations in bra-ket notation as

$$|\psi\rangle = |\chi\rangle + G_0 V|\psi\rangle \tag{2.11}$$

Defining the scattering matrix T such that $T|\chi\rangle = V|\psi\rangle$, we obtain

$$|\psi\rangle = |\chi\rangle + G_0 T|\chi\rangle \tag{2.12}$$

$$T_{\alpha\alpha'} = \langle\chi_\alpha|V|\psi'_\alpha\rangle \tag{2.13}$$

Similarly, the iterative form of Eqn. 2.11 is written as

$$|\psi\rangle = |\chi\rangle + G_0V|\chi\rangle + G_0VG_0V|\chi\rangle + G_0VG_0VG_0V|\chi\rangle + \ldots \tag{2.14}$$

$$T_{\alpha\alpha'} = \langle\chi_\alpha|(V + VG_0V + \ldots)|\psi'_\alpha\rangle \tag{2.15}$$

where the matrix T defines the scattering events given by an infinite series generally called Born series. If the series is truncated only at the first term V (single point scattering), its referred to as the first Born approximation. The summation of the series in Eqn. 2.15 can be written as Eqn. 2.16 called Dyson equation

$$T = (1 - VG_0)^{-1}V \tag{2.16}$$

In Sec. 2.3, we use the framework presented in this section to study phonon scattering in rough surface waveguide. The perturbation of the w.f. (ψ)in this case is a random potential created by rough surface over an unperturbed smooth waveguide (χ). Before proceeding to this problem, we should first identify the phonons that propagate in a nanowire system and obtain the phonon dispersion relations.

2.2 Dispersion models in nanowires

It is imperative to calculate complete phonon dispersion relations in nanowires for accurate modeling of NW thermal conductivity [2]. Several atomistic models like lattice dynamics (LD) yield the closest approximation to complete dispersion when appropriate interatomic potentials are taken into account [60]. Lattice dynamics calculations, however are computationally cumbersome for NWs of diameters > 10 nm. This limits the application of LD simulations to model NWs of diameter > 50 nm, the range pertinent to our study. Hence, we start with LD calculations on sub-10 nm NWs and calculate the deviations from the bulk Si dispersion to quantify the size effects in NWs.

The complete details of LD simulations can be found in several textbooks like Ref.[61, 60]. Briefly, LD simulations consider atoms in Si lattice interacts with their nearest neighboring atoms through a harmonic potential with Si–Si bond stiffness K_s and three-body bond angle stifness K_ϕ. The total potential Ψ of the lattice system with N Si atoms is written as

$$\Psi(\mathbf{u}) = \sum_{i,j}^{N} \frac{1}{2} K_s [\vec{r_{ij}}.(u_i - u_j)]^2 + \sum_{ijk,k<i}^{N} \frac{1}{2} K_\phi (\theta_{ijk} - \theta_0)^2 \tag{2.17}$$

where the vector $\mathbf{u}$ represents the coordinates of the atomic positions, r_{ij} is position vector between atoms i and j and θ represents the bond angle. Using Eqn. 2.17, we construct the dynamic matrix $\mathbf{D}$, a $3N \times 3N$ matrix (each atom has 3 degrees of freedom) as

$$\mathbf{D_{mn}} = -\frac{\partial \Psi(\mathbf{u})}{\partial u_m \partial u_n} \tag{2.18}$$

We construct the dynamic matrix for atoms in an unit cell of dimension $D \times D \times a$ where D is nanowire diameter and a is the lattice constant as shown in Fig. 2.3 (a). Finally applying the Bloch periodic condition by forcing the condition $u_j = exp(j\vec{k}.\vec{r_{ij}})u_i$, we obtain an eigenvalue problem $\mathbf{D}(\tilde{\mathbf{k}})\tilde{\mathbf{u}} = M\omega^2\tilde{\mathbf{u}}$. Since the periodicity condition in NWs is only the longitudinal direction, $\vec{k} = (0, 0, k_z)$. Here, the matrix M is a diagonal matrix consisting of atomic masses, ω is the frequency of the eigenmodes. The eigenvalue problem has $3N$ eigenvalues with the lowest eigenvalue ω=0 when k_z=0 when the boundary atoms in x and z are free to move (stress-free condtion).

Figure 2.3 (a) shows the LD solution for lowest lying transverse modes in a nanowire of diameter 3 nm. Considering the sound velocity in NW (v_{NW}) as slope of the lowest mode (passing through ω=0 at k=0), we present the values of v_{NW}/v_{bulk} for diameters upto 10 nm. Transverse velocity of sound in bulk v_{bulk} is taken as 5400 m/s. We find the quantum confinement effects are negligible for D> 10 nm. Hence, we proceed by approximating each branch in LD solution with parabolas, which we call the parabolic approximation. Specifically, in a square wire of side D, we can fit discrete number of wavelengths in x and y direction such that $k_x = m\pi/D$ and $k_y = n\pi/D$ where m and n are integers. Hence using the simple dispersion $\omega = c\mathbf{k}$, we express the parabolic approximation of phonon dispersion as

$$\omega = c\sqrt{k_z^2 + \left(\frac{m\pi}{D}\right)^2 + \left(\frac{n\pi}{D}\right)^2} \tag{2.19}$$

For a circular wire of diameter D, the parabolic approximation transforms to

$$\omega = c\sqrt{k_z^2 + \left(\frac{2\mu_m^n}{D}\right)^2} \tag{2.20}$$

where μ_m^n is the n^{th} zero of Bessel function of order m. We calculate the thermal conductivity of NWs using Casimir limit for boundary scattering [30] using both the complete dispersion relations from lattice dynamics [2] and the parabolic approximation. We artificially truncate the phonon frequencies at 3.6 THz for transverse modes and 10 THz for longitudinal modes in order to match density of modes as shown in Fig. 2.3 (b). We find a very close match of thermal conductivity using either models shown in Fig. 2.3 (d). Hence we proceed with the parabolic dispersion approximation for nanowire modeling in this work. This assumption also allows great convenience in applying Helmoltz wave equation to model phonons since this equation satisfies the dispersion in Eqn. 2.19.

Phonon dispersion relation is also impacted the boundary condition on the nanowire surfaces. We evaluated the phonon dispersion for two limits of boundary conditions – stress free (Neumann)and frozen boundary (Dirichlet). We use the full-elasticity equation in a solid cylindrical wire [62][63] for the two boundary conditions. Figure 2.4 shows the acoustic dispersion in the nanowire of diameter $D = 50$ nm for both the boundary conditions .

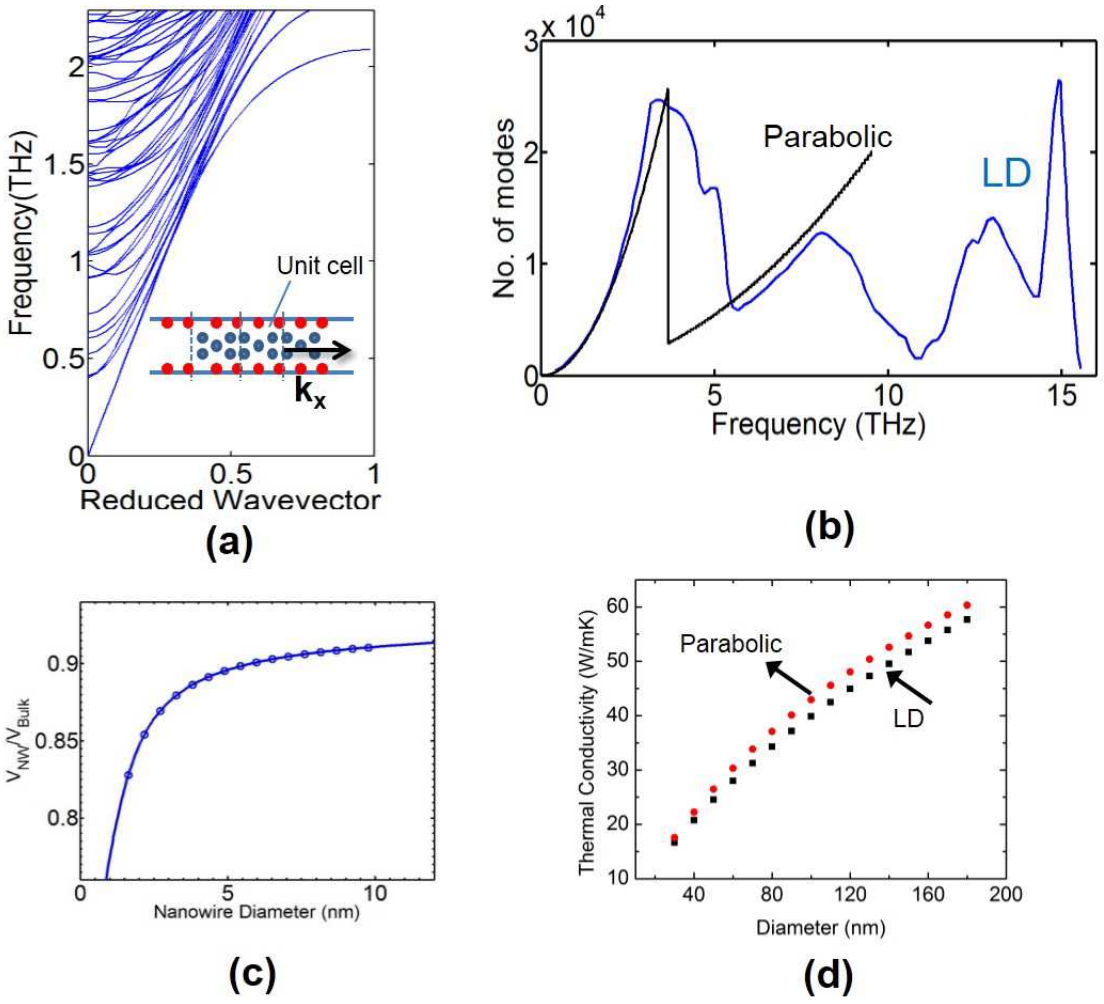

Figure 2.3: (a) Lowest lying transverse modes of a 3 nm nanowire calculated by lattice dynamics. (b) Density of modes calculate from complete LD simulations are compared with the parabolic dispersion equation in Eqn. 2.19. (c) The ratio of sound velocity in NWs to bulk shows the confinement effects are not significant for NW diameter >10 nm. (d) Casimir limit of thermal conductivity of SiNWs calculated using parabolic approximation closely match the calculation from LD from Ref. [2].

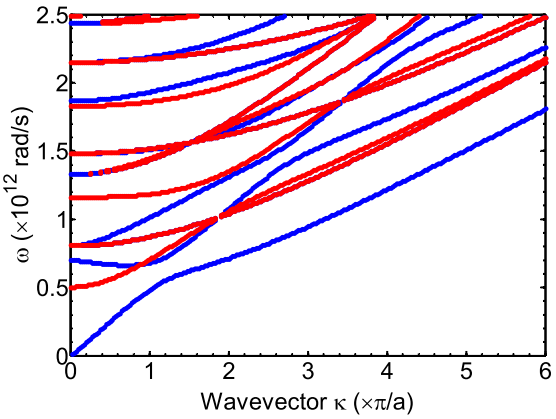

Figure 2.4: Acoustic phonon dispersion for the lowest-lying modes under rigid (in red) and stress-free (in blue) conditions at the nanowire surface.

We can observe that the Neumann condition accounts for the fundamental mode (modes with vanishing transverse wavenumber). The energy spacing between the corresponding branches for Dirichlet and Neumann boundary conditions $\Delta E = \hbar\Delta\omega$ is of order $\sim$ 0.3 meV and thus $\Delta E << k_b T$ for temperatures above 100 K. We conclude that consideration of the change in phonon dispersion due to boundary condition is relevant only at low temperatures. Hence, we anticipate the choice of boundary condition does not significantly impact the prediction of thermal conductivity.

2.3 Multiple scattering in rough nanowires

In order to consider coherent phonons, we start with a wave treatment of phonon transport. The interaction of phonons with the randomly rough walls of the nanowire leads to an attenuation of the mean intensity. To estimate the mode dependent attenuation, we derive the phase shift induced by the surface roughness. We consider a wire of length L along the x-direction. Rough walls are present along the y- and z-directions such that $0 \leq y \leq a$;

$0 \leq z \leq b$ define the wire dimensions. We note that experimental nanowires are typically not cylindrical. When comparing with diameter dependent experimental data, we define the characteristic diameter, $d = \sqrt{4ab/\pi}$. We use individual scalar wave equations to describe polarizations of phonons in the wire, implicitly ignoring coupling between polarizations enabled by the disorder. By comparison with experimental data later, we show that this simplifying assumption is still adequate in illustrating the basic physics.

To obtain the phase shift, we need the Green function, G, for phonons in the rough wire. This modified Green function can be obtained from the Green function of a smooth wire G_0 as described below. The Green function G_0 for a smooth square wire is a solution of Helmoltz equation with a stress free boundary condition over its smooth walls $\mathbf{S}$ given as

$$\begin{aligned} \left(\nabla^2 + K^2\right) G(R, R_0) &= -4\pi\delta(R - R_0) && (2.21) \\ (\partial G/\partial n)_{\Re} - \alpha G &= 0 \ , && (2.22) \end{aligned}$$

where $\overrightarrow{n}$ is the outward normal to $\Re$, K is the total wave number, R and R_0 are the point of observation and the source respectively. The boundary condition in Eq. 2.22 describes a generalized impedance condition with the limits $\alpha = 0$ and $\alpha^{-1} = 0$ being the Neumann (stress-free) and the Dirichlet boundary conditions respectively.

In defining the boundary condition, we hypothesize that the surface responsible for scattering phonons is the interface between the crystal and the surface oxide and not the outer surface. Our hypothesis follows from existing transmission electron micrographs of the rough nanowires [3]. While an impedance boundary condition is more appropriate here, the transmission coefficient of phonons between silicon and its native oxide remains unknown theoretically and experimentally. Thus, we choose to use a stress free condition (Neumann) and frozen boundary condition (Dirichlet) for mathematical convenience. We note that the oxide thickness is $\sim$ 2 nm and we do not expect the thin oxide itself to play a dominant role in surface scattering.

The solution for Eq (2.22) for a three dimensional smooth waveguide $\mathbf{R} =$

$\{x, y, z\}$ can be expressed as[41]

$$G_0(R, R_0) = \int_{-\infty}^{\infty} \frac{d\kappa}{2\pi} e^{i\kappa(x-x_0)} \sum_m \sum_n \frac{\phi_{mn}(y,z)\phi_{mn}(y_0,z_0)}{k^2 + (n\pi/a)^2 + (m\pi/b)^2 - K^2} \quad (2.23)$$

where a and b are cross sectional dimensions of the square wire and the transverse eigenfunctions $\phi_{mn}(R)$ are given by

$$\phi_{mn}(x, y, z) = \frac{2\epsilon_{mn}}{(ab)^{1/2}} \, cos\left(\frac{n\pi y}{a}\right) cos\left(\frac{m\pi z}{b}\right) exp(i\kappa_{mn} x) \quad (2.24)$$

where $\kappa_{mn}^2 = K^2 - (n\pi/a)^2 - (m\pi/b)^2$ is the longitudinal wavevector; $\epsilon = 1/2$ for $m = n = 0$ and is unity otherwise.

To obtain the modified Green function in the same volume with random perturbation in the surface profile **S**, we solve Eq. (2.21) with the boundary condition in Eq. (2.22) applied over the random rough surface $\Re$ instead of **S**. If the rough boundary at the bottom of the square nanowire is assumed $z = \zeta(x)$ where $\zeta(x)$ represents the random surface height along the wire length, we can enforce the stress free condition as $\partial G/\partial n|_{\Re} = 0$. We then project the boundary conditions on the rough surface, $\Re$ onto the smooth boundaries **S** by expressing the surface normal on $\Re$ as $\overrightarrow{n} = -\overrightarrow{z} + \zeta'(x)\overrightarrow{x}$ where $\zeta'(x) = d\zeta/dx$ is the random slope of $\Re$. Hence the boundary condition for the rough wire becomes

$$\frac{\partial G}{\partial n}\Big|_{\Re} = \left(-\frac{\partial G}{\partial z} + \zeta'(x)\frac{\partial G}{\partial x}\right)\Big|_{z=\zeta(x)} = 0. \quad (2.25)$$

Expanding Eq. (2.25) for Neumann condition about the smooth boundary $z = 0$ in terms of ζ and ζ', retaining only first order derivates, we obtain

$$\left(\frac{\partial G}{\partial z} + \zeta\frac{\partial^2 G}{\partial z^2} - \zeta'\frac{\partial G}{\partial x}\right)_{z=0} = 0 \quad (2.26)$$

For a generic three-dimensional surface, the above boundary condition can be expressed as

$$G + \zeta\frac{\partial G}{\partial n_s} = 0 \text{ (Dirichlet)} \quad (2.27)$$

$$-\nabla_\perp\zeta.\nabla_\perp G + \frac{\partial G}{\partial n_s} + \zeta\frac{\partial^2 G}{\partial n_s^2} = 0 \text{ (Neumann)} \quad (2.28)$$

where $\nabla_\perp = (\partial/\partial r)\hat{r} + (\frac{1}{r})\,(\partial/\partial\phi)\,\hat{\phi}$ denotes transverse part of surface gradient and n_s is the normal vector to the smooth surface $\mathbf{S}$.

By using Green theorem, we can express the Green function in rough wires as

$$G(R,R_0) = G_0(R,R_0) + \frac{1}{4\pi}\int_S \left(G(R,r)\frac{\partial G_0(r,R_0)}{\partial n} - G_0(R,r)\frac{\partial G(r,R_0)}{\partial n} \right) dr \tag{2.29}$$

where $r \in \mathbf{S}$. Substituting the boundary conditions in Eq. (2.26) and Eq (2.22) into Eq. (2.29), we obtain

$$G(R,R_0) = G_0(R,R_0) + \frac{1}{4\pi}\int_S G_0(R,r)\widehat{V}(r)G(r,R_0)\; dr \tag{2.30}$$

where the operator $\widehat{V}(r)$ with $r \equiv \{x,y,z\}$ is given by

$$\widehat{V}(r) = \zeta\frac{\partial^2}{\partial z^2} - \zeta'\frac{\partial}{\partial x} \tag{2.31}$$

For generic three dimensional surface, the perturbation operator $\widehat{V}(\zeta)$ for the two boundary conditions are

$$\widehat{V}(\zeta) = \leftarrow -\frac{\partial}{\partial n_s}\zeta\frac{\partial}{\partial n_s} \rightarrow \text{ (Dirichlet)} \tag{2.32}$$

$$\widehat{V}(\zeta) = \zeta\frac{\partial^2}{\partial n_s^2} - \nabla_\perp\zeta.\nabla_\perp \text{ (Neumann)}, \tag{2.33}$$

where the left and right arrows denote operation on the left and right functions respectively.
Applying an iteration method, we substitute the Green function $G(r,R_0)$ on left hand side of Eq. (2.30) with the Green function from i^{th} iteration $G^{(i)}(R,R_0)$ thus obtaining an infinite series expansion for $G(R,R_0)$ as shown in Eq. (2.34)

$$\begin{aligned} G(R,R_0) = G_0(R,R_0) &+ \frac{1}{4\pi}\int G_0(R,r)\widehat{V}(r)G_0(r,R_0) \\ &+ \frac{1}{(4\pi)^2}\int\int G_0(R,r_1)\widehat{V}(r_1)G_0(r_1,r_2)\widehat{V}(r_2)G(r_2,R_0)\; dr_1 dr_2 + \ldots \end{aligned} \tag{2.34}$$

Thus the n^{th} term in this series is a n-fold integral over the surface involving n functions $\widehat{V}(r_i)$ $(i = 1, 2, 3 \ldots n)$ and represents the n^{th} order scattering field at a point R from the roughness aspersions due to source at R_0. Eqn. 2.34 resembles the Dyson equation from the multiple scattering theory. Dropping the integrals, 4π factor and the arguments of the functions, we can rewrite Eqn. 2.34 as

$$G = G_0 + G_0 \left(VG_0 + VG_0V + VG_0VG_0V + \ldots \right) G \tag{2.35}$$

Retaining only the first non-zero term in series of Eqn. 2.35 leads to the widely used first-Born approximation. This approximation reduces the problem to single scattering where the wave interacts with a particular scatterer on the surface only once. This approximation fails [45] when the surface has a correlation length on the order of a phonon wavelength, which is the case for nanowires at room temperature. To proceed, we instead employ the Bourret approximation or the first-smoothing approximation which accounts for second-order scattering terms.

The first statistical moment $\langle G(R, R_0) \rangle$ represents the field intensity at point R coherent with the source at R_0. Hence the spatial decay of averaged Green function yields the length over which coherence is lost due to the boundary scattering. We proceed with ensemble averaging of the Green function from Eq. (2.30) over statistical realizations of ζ. To this purpose, we assume the random function ζ is statistically uniform and varies only along the wire length (x), we assign normal Gaussian statistics to ζ such that $\langle \zeta(x) \rangle$=0, $\langle \zeta^2(x) \rangle$=0 and the spatial correlation function is

$$\langle \zeta(x_1)\zeta(x_2) \rangle = \sigma^2 exp(-|x_1 - x_2|^2 / L_c^2) \tag{2.36}$$

Here σ is root mean square height of surface ζ and L_c is its correlation length. More complex two-dimensional roughness models are discussed in Section 2.6. Averaging Eq. (2.34) and noting that all the odd-moments of the random operator $\widehat{V}(r)$ vanish, we finally obtain

$$\langle G(R, R_0) \rangle = G_0(R, R_0) + \frac{1}{(4\pi)^2} \int \int_S G_0(R, r_1) \widehat{M}(r_1, r_2) \langle G(r_2, R_0) \rangle \, dr_1 dr_2 \tag{2.37}$$

where the mass operator $\widehat{M}(r_1, r_2)$ is the sum of infinite terms represent-

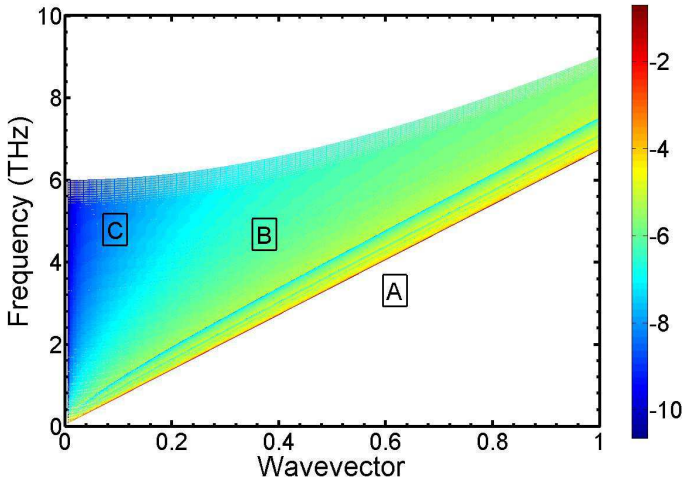

(a)

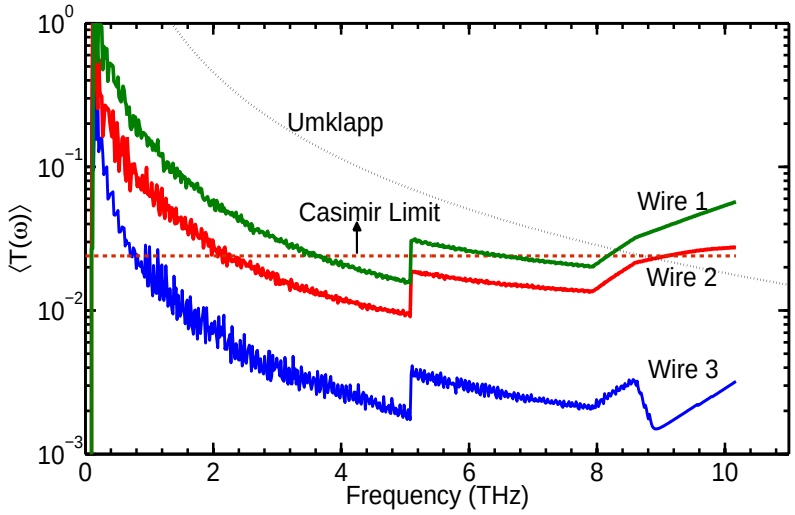

(b)

Figure 2.5: (a) The logarithm of attenuation length plotted on phonon dispersion plot shows (A) quasi-ballistic transport for modes near fundamental branches (B) diffuse modes and (C) non-conducting modes near the zone center with high transverse wavenumbers. (b) The boundary scattering transmission coefficient for longitudinal modes averaged over number of modes is shown for wire 1 (σ=0.8 nm, L_c=300 nm), wire 2 (σ=2.5 nm, L_c=90 nm) and wire 3 (σ=2.5 nm, L_c=30 nm) for a 50 nm wire representing transition from smooth to very rough surface. The Casimir transmission ($=d/L$) and the Umklapp transmission($=\Lambda_u/L$) are also shown.

ing increasing order of correlations in $\widehat{V}$. The first term of the mass operator is $\langle \widehat{V}(r_1) G_0(r_1, r_2) \widehat{V}(r_2) \rangle$ and we retain only this term which is the so-called Born approximation in volume scattering theory [64]. The solution of Eq. (2.37) which resembles Dyson equation can be solved using spatial Fourier transform outlined in Ref. [65].

Finally we expand the averaged Green function in plane waves $exp[i\overline{\kappa}_r r]$ where $\overline{\kappa}_r$ is the perturbed wavenumber due to roughness. The unperturbed wavenumber κ_{mn} (Eq. (2.24)) thus shifts by $\delta\kappa_{mn}$=$\overline{\kappa}_{mn} - \kappa_{mn}$. This shift is proportional to the mass operator and the derivative of the unperturbed eigenfunctions ϕ_{mn} in Eq. (2.24) with respect to the Fourier variable κ. The mean attenuation length of wave intensity is obtained from the imaginary part of this wavenumber shift $\mathrm{Im}(\delta\kappa_{mn})$ as $l = [2\mathrm{Im}(\delta\kappa_{mn})]^{-1}$ .For phonon mode with transverse wavenumbers $\{m, n\}$, we obtain the mean attennuation length as

$$l_{mn}(\omega)^{-1} = \left(\frac{\sigma}{d}\right)^2 \frac{2\epsilon_{mn}}{\kappa_{mn}} \sum_p \sum_q \sum_{\alpha=0,\pi} \frac{\epsilon_{pq}(K^2 - \kappa_{mn}\kappa_{pq}\cos\alpha)^2}{\kappa_{pq}} \widetilde{W}(|\kappa_{mn} - \kappa_{pq}|), \tag{2.38}$$

where m, n, p and q are indices representing phonon modes, κ is the longitudinal wave number, α is the angle between incident (mn) and scattered directions (pq). The Fourier transform of the wall roughness correlation function is given by $\widetilde{W} = \sqrt{\pi} L_c exp(-\kappa^2 L_c^2/4)$; $K = \omega/c$ is the wave number of the phonon propagating at speed c. The summation in Eq. 2.38 represents the sum of scattering probabilities of the incident field mn into all possible incoherent channels where the probability for scattering into a particular channel pq is proportional to the correlation function $\widetilde{W}(\kappa_{mn} - \kappa_{pq})$. The double summation runs over all modes p, q that satisfy $\sqrt{p^2 + q^2} < \omega d/c$ representing the total phonon modes $N(\omega)$ at the frequency ω.

2.4 Thermal conductance of rough nanowires

2.4.1 Phonon transmission coefficient

We proceed with calculating the attenuation length of every eigenmode ϕ_{mn} of a square wire using Eq. (2.38) with appropriate choice of roughness parameters σ and L_c. Figure 2.5(a) plots the logarithm of inverse of the mean field attenuation length ($log_{10}\ l_{mn}$) as a function of phonon frequency and wave number. Three distinct transport regimes become evident: Quasi-ballistic, weakly localized and diffusive. We now discuss each of the regimes individually. The quasi-ballistic regime is restricted to the fundamental modes ($\omega \sim k$) with long wavelengths. These modes see the surface corrugations as point-like imperfections and propagate quasi-ballistically until scattered by Umklapp processes. Since the attenuation length exceeds the length of wire, the transmission function is given by $t(\omega) = 1 - L/l$. In contrast, high frequency and long wavelength modes with large transverse wave vectors, $k_\perp$ are strongly attenuated. Using the results of the DMPK theory [51], the phonon localization length is Nl, where N is the number of phonon modes at frequency ω. When $Nl << L$, the transmission of these phonon modes $t(\omega) = \exp(-L/Nl)$. Even though the model predicts these to be localized, it is likely that these can still propagate particle-like between scatterers [66, 38]. In any case, their contribution to thermal conductivity is small due to their low group velocities. Overall, we do not expect a detectable localization behavior in thermal conductivity. We confirm this assertion later with calculations.

All other modes are diffusive and fall into the third and most dominant regime. The transmission function is $t(\omega) = l/L$, where the frequency dependence of l yields the overall frequency dependence of surface scattering. In the Casimir limit, this becomes frequency independent and l is replaced by the diameter of the wire. We note that the above arguments apply only when the attenuation length, l is smaller than the Umklapp scattering mean free path, Λ_u at the same frequency. In the absence of this condition, surface scattering remains uncorrelated. The effective transmission at the frequency ω, is an average over the transmission coefficient of individual modes $N(\omega)$

in each regime such that $\overline{T_b}(\omega) = \sum_{m,n} t_{mn}/N(\omega)$ where the subscript b represents boundary scattering.

Figure 2.5(b) compares the mode averaged transmission function $\overline{T_b}(\omega)$ for the Casimir limit with that for multiple scattering. We choose a 50 nm diameter wire and vary the surface roughness to make this comparison. The strong frequency dependence of the low frequency modes is consequential only at very low temperatures. At room temperature, the dominant frequency range is ∼1-7 THz. In smooth wires, the transmission function has contributions above and below the Casimir limit which effectively balances out the frequency dependence. However, as surface roughness increases, the function increasingly deviates below the Casimir limit for high frequency phonons. The sharp discontinuities in the transmission are consequences of mode averaging. The discontinuity in $N(\omega)$ at $\sim$ 5 THz and $\sim 9-10$ is due to the sharp decline of transverse and longitudinal modes respectively at these frequencies which shows up as apparent jump in $\overline{T_b}(\omega)$ in Figure 2.5(b). We also plot the transmission function for Umklapp scattering for comparison. The delay in the onset of Umklapp scattering is evident in rougher nanowires.

2.4.2 Landauer formula for thermal conductance

We use the transmission function to calculate the thermal conductivity of a rough surface nanowire. Following Mingo's approach [2, 67], we write the Landauer formula for the thermal conductance of the nanowire,

$$G_{TH} = \sum_{i=1}^{3} \frac{1}{2\pi} \int_0^{\omega_c^i} N_i(\omega)\overline{T_i(\omega)}\hbar\omega \frac{d\langle n\rangle}{dT}\, d\omega \tag{2.39}$$

where $\langle n\rangle$ is the Bose-Einstein distribution and i represents the polarization of a phonon mode. The cut-off frequency, ω_c for longitudinal modes ($i = 1$), ω_c^L and transverse modes ($i = 2, 3$), ω_c^T are 10 THz and 3.6 THz in accordance with the bulk Si dispersion [68]. The speed of longitudinal and transverse modes are $c_L = 8400$ m/s and $c_T = 5400$ m/s respectively. As temperature increases, the transmission function should include increasing contributions from Umklapp and isotope scattering. The mean free

path for isotope scattering, Λ_m=$\langle c \rangle / A\omega^4$ and that for Umklapp scattering, Λ_u=$\langle c \rangle / BT\omega^2 e^{-C/T}$ where $\langle c \rangle$=6400 m/s are added to the transmission function using the Matthiessen's rule. We use values fit to bulk silicon data [2, 68]: $A = 1.32 \times 10^{-45} s^{-3}$, $B = 1.7 \times 10^{-19}\ s^{-1}K^{-1}$ and $C = 140$ K. The overall transmission function is $\overline{T_i}(\omega) = \left(\overline{T_{b,i}}^{-1} + L/\Lambda_m + L/\Lambda_u\right)^{-1}$.

2.5 Results and Discussion

2.5.1 Effect of roughness scales

The two roughness parameters, the root mean square height, σ and the correlation length, L_c affect transport differently. Under the Born approximation, the ratio (σ/d) has an inverse quadratic relation with the attenuation length. Since the transmission function, $\overline{T_b(\omega)}$ is linear in the attenuation length in the dominant diffusive transport regime, the thermal conductance becomes proportional to the inverse of $(\sigma/d)^2$. Figure 2.6(a) plots the change in room temperature thermal conductivity of a 50 nm silicon nanowire of 2 μm length as the roughness height varies from atomically smooth ($\sim$A^o) to 5 nm. The thermal conductivity dips sharply till σ = 2 nm as the propagation of high frequency phonon modes near the zone center becomes affected. These modes with $\sigma k_\perp >> 1$ are strongly attenuated, consistent with the Rayleigh criterion for destructive interference of the scattered wavefronts. The calculations show that the effect of the roughness height reaches a plateau above σ=4 nm similar to the trend reported in Ref [40]. The present calculations likely overestimate the thermal conductivity at larger values ($\approx$5 nm) of σ where terms of order σ^4 would likely increase the attenuation coefficient. However, the trend in roughness height is strongly dependent on the correlation length L_c with an increased sensitivity of the thermal conductivity to roughness height at lower correlation lengths.

The other parameter, the correlation length L_c, affects transport in three ways. First, the inverse of the correlation length controls the Gaussian width of the roughness Fourier spectrum. Strong surface scattering requires the change in phonon wave number on scattering to lie within the Gaussian

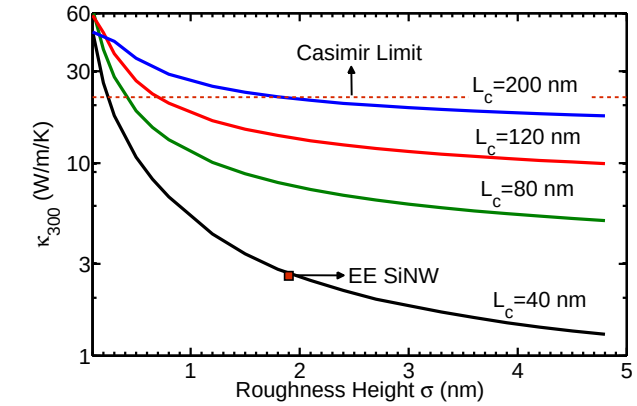

(a)

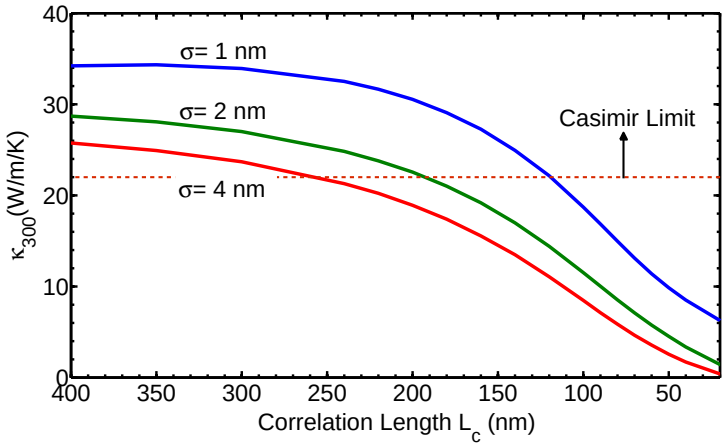

(b)

Figure 2.6: Dependence of thermal conductivity at 300 K on (a) roughness height at different correlation lengths (b) correlation length at different roughness heights for a 50 nm wire, 2μm in length

.

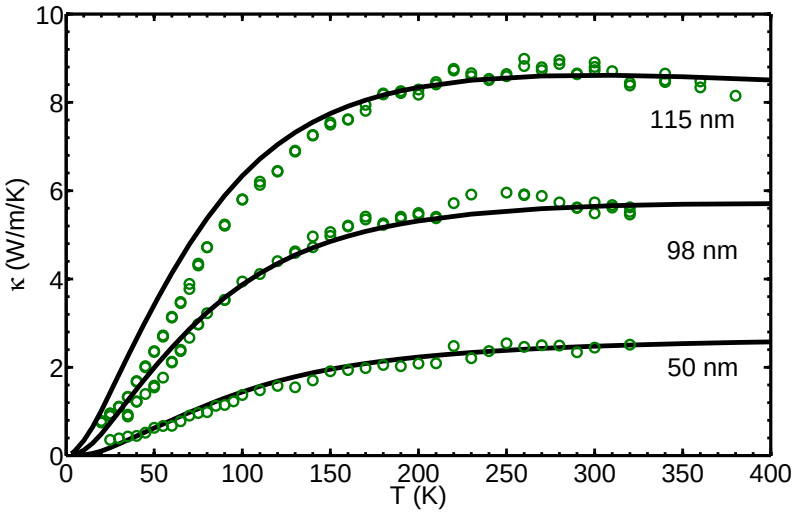

Figure 2.7: Temperature trend of thermal conductivity of EE SiNW for 50 nm ($\sigma = 2.2$ nm, $L_c = 21$ nm), 98 nm ($\sigma = 2.2$ nm, $L_c = 70$ nm) and 115 nm ($\sigma = 2$ nm, $L_c = 86$ nm) diameter wires. The experimental data is from Ref [3].

width. Thus, a short correlation length increases the phase space for effective multiple scattering, allowing more phonons to participate in the process. A large correlation length reduces the roughness spectrum to a delta-like function. Such roughness can only scatter very long wavelengths, which do not contribute significantly to thermal transport. Second, the correlation length determines the angular spread of intensity in the scattered field, given by $\Delta\Phi \propto (\omega L_c/c)^{-1}$. If a phonon is incident at an angle θ_n from the tangent to the scattering surface, the scattered field in a direction θ_m is proportional to $\exp(-|\cos\theta_n - \cos\theta_m|^2 L_c^2)$. Third, the correlation in relation to the wire diameter controls the cut-off angle for phonons participating in correlated scattering. Phonons incident at angles smaller than $\cot^{-1}(L_c/2d)$ from the surface can not undergo multiple scattering. Figure 2.6(b) shows the effect of the correlation length on the room temperature thermal conductivity. Quantitatively, the effect of surface roughness on thermal conductivity diminishes when $L_c > 100$ nm.

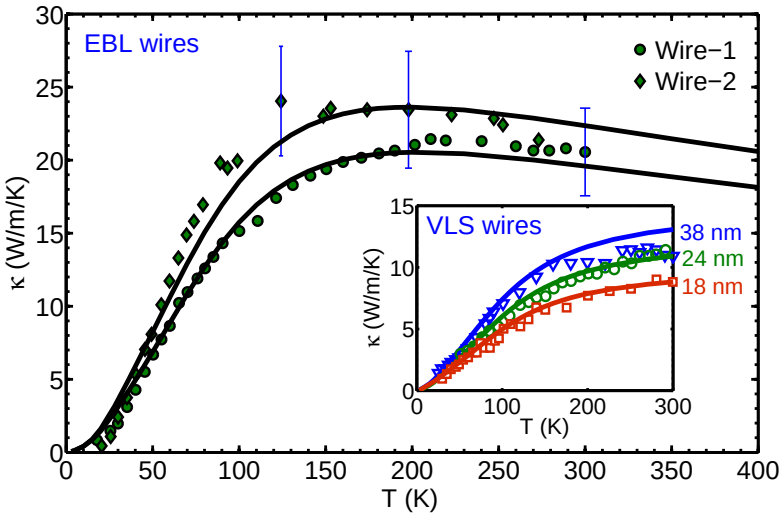

Figure 2.8: Temperature trend of thermal conductivity of EBL wires using $\sigma = 7.4$ nm and $L_c = 400$ nm for Wire-1 ($120\times$ 41 nm^2 and $L = 4\mu m$) and Wire-2 (86×62 nm^2 and $L = 7\mu m$). The data is from Ref [4]. (*Inset:* Temperature trend of thin VLS wires compared against data from Ref [5]) using $\sigma = 1$ nm, $L_c = 80$ nm).

2.5.2 Comparison with data

We now compare the thermal conductivity calculated from the above model with experimental data on electrolessly etched (EE) rough nanowires, electron beam lithography (EBL) defined rough nanowires and vapor-liquid-solid (VLS) grown smooth nanowires respectively. Figure 2.7 compares the predictions with data for EE wires and Figure 2.8 shows the thermal conductivity temperature trend for EBL wires across different diameters. We find an excellent agreement with the EE wire data from Ref. [3] using the roughness scales, $\sigma = 2.2$ nm and $L_c/d = 0.5 - -0.7$, close to the values reported for these wires from high resolution transmission electron images. We find similar agreement with the data for EBL wires. The thermal conductivity of EBL wires increases approximately four times when compared to EE wires despite an increased roughness height compared to EE wires. This increase results from the large increase in the roughness correlation length in EBL wires compared to EE wires. A nominal rms height, σ =7.4 nm and a correlation length, L_c =400 nm provide a good fit for EBL wires of different cross sections but similar characteristic diameter. Our model also captures the

delay in the onset of Umklapp scattering related dip in the thermal conductivity between Wire-1 ($120 \times 41\ \mu m^2$) and Wire-2 ($86 \times 62\ \mu m^2$). The reason is the higher boundary scattering rate in the former. As a check, we calculated the thermal conductivity of smooth VLS grown nanowires assuming small roughness scales. The calculations fit the data for VLS wires ($d > 37$ nm) from Ref. [33] using σ =0.4 nm and L_c fixed at 100 nm. The thermal conductivity data for thinned nanowires [5] which show a linear trend in thermal conductivity till 200 K are fit using $\sigma = 1.2$ nm.

2.6 Effects of two-dimensional roughness

In this section, we consider a cylindrical wire (of nominal diameter a and length L) with both longitudinal and azimuthal roughness. The radius at any point on the surface of the rough wire ($\Re$) is given by $r = a/2+\zeta(x,\phi)$, where ζ is a random roughness function as shown in Fig. 2.9. We use $r = \{\phi, x\}$ to represent the coordinate of a point on the surface and $R = \{r, \phi, x\}$ to denote the cylindrical coordinate system. The surface height ζ is assumed to be statistically homogeneous with small gradient $|\partial\zeta/\partial\rho| << 1$ and $|\partial\zeta/\partial x| << 1$. The small roughness height approximates conditions for the experimental wires where the roughness height is typically ≤ 2 nm for wires of $\sim$100 nm diameter. Further, we assume the statistical average, $\langle\zeta\rangle$, which is the mean height of the roughness, to be zero.

The derivation of attenuation coefficient for a cylindrical wire with two-dimensional roughness follows the methods presented in Sec. 2.3. The statistical roughness is now represented by a Gaussian process defined as

$$\langle\zeta(x,\phi)\zeta(x+X,\phi+\theta)\rangle = \sigma^2 W(X,\theta) \quad (2.40)$$

$$\text{where } W(X,\theta) = \exp(-X^2/L_c^2)\exp(-\theta^2/\Phi_c^2) \quad (2.41)$$

with the roughness characterized by three length scales – σ is RMS roughness height, L_c is the longitudinal correlation length and $a\Phi_c/2$ is the azimuthal correlation length. Now, using Eq. 2.27 and Eq. 2.41, we can express the statistical average $M(\rho_1,\rho_2) = \langle\widehat{V}(\rho_2)G_0\widehat{V}(\rho_1)\rangle$ in Eq. 2.37 for the Dirichlet boundary condition[69], for example, as

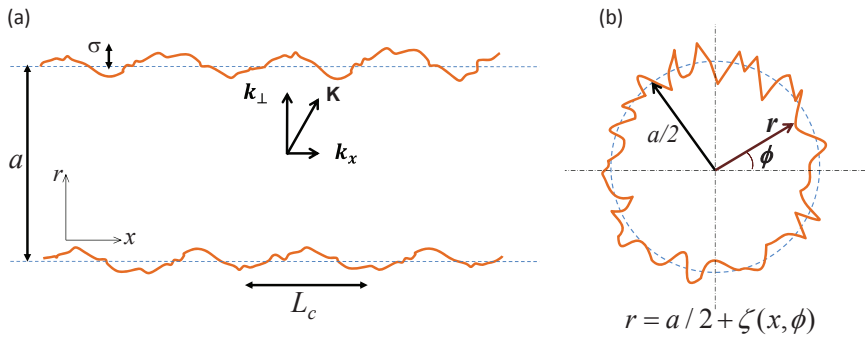

Figure 2.9: Schematic of the the longitudinal section (a) and the cross-section (b) of a rough nanowire showing the relevant roughness scales used in the model.

$$M(\rho_1, \rho_2) = -\sigma^2 W(\rho_1 - \rho_2) \frac{\partial^2}{\partial r_1 \partial r_2} \langle G_0(R_1, R_2) \rangle \frac{\partial}{\partial r_2}. \tag{2.42}$$

We obtain the boundary condition for solving the averaged Green function $\langle G \rangle$ by letting R in Eq. 2.37 approach the smooth surface as follows:

$$\langle G(r, R_0) \rangle + \int d\rho' M(\rho, \rho') \langle G(r', R_0) \rangle = 0 \text{ (Dirichlet)} \tag{2.43}$$

$$\partial \langle G(r, R_0) \rangle / \partial r = \int d\rho' M(\rho, \rho') \langle G(r', R_0) \rangle \text{ (Neumann)}, \tag{2.44}$$

We must now solve for the averaged Green function $\langle G \rangle$ from Eq. 2.21 using the boundary condition Eq. 2.43 or Eq. 2.44 . To proceed, we take a Fourier transform of the Green functions defined as

$$\widetilde{G}(\kappa, m; r, r_0) = \int_{x=-\infty}^{x=\infty} \int_{\phi=-\pi}^{\phi=\pi} dx \; d\phi \; \exp[jk_x(x - x_0)] \; \exp[jm(\phi - \phi_0)] G(r, R_0) \tag{2.45}$$

where κ is longitudinal wavenumber and m is the angular wavenumber.

The unperturbed Green function, G_0, for the smooth wire with Dirichlet boundary condition [65] are given by

$$\Psi_{mn}(r, \phi, x) = \frac{\sqrt{2} J_n\left(\frac{2r}{a} \mu_n^m\right)}{\pi a J_n'(\mu_n^m)} \exp[jm\phi + j\kappa_m^n x] \tag{2.46}$$

where {m,n} represent the eigenmode with transverse wavenumber μ_n^m which

corresponds to the m^{th} zero of the Bessel function J_n. The longitudinal wavenumber is $\kappa_m^n = \sqrt{K^2 - \mu_n^m}$. Hence G_0 can be obtained from normal modes in Eqn 2.46 by Hilbert-Schmidt expansion [65].
For the Dirichlet boundary condition, the attenuation length of the field intensity is obtained as

$$l_{mn}^{-1} = \left(\frac{\sigma}{2\sqrt{\pi}a}\right)^2 \sum_{p=1}^{N} \sum_{s=1}^{M(p)} \frac{(\mu_s^p/a)^2 (\mu_n^m/a)^2}{\kappa_n^m \kappa_s^p} \left[\widetilde{W}(\kappa_n^m - \kappa_s^p; m-p) + \widetilde{W}(\kappa_n^m + \kappa_s^p; m+p)\right], \tag{2.47}$$

where $\{m, n\}$ and $\{s, p\}$ represent incident and scattered phonon modes. Since the attenuation of a particular mode of frequency ω depends on the probability of scattering into all the possible incoherent directions available at that frequency, the double summation in Eq. 2.47 run over all directions $\{s, p\}$ such that $\mu_1^N < a\omega/c < \mu_1^{N+1}$ and $\mu_M^p < a\omega/c < \mu_{M+1}^p$. Here c is propagation speed of the mode. Using these limits of summation, we can also obtain $N(\omega)$, the total number of modes at the frequency ω. In Eq. 2.47, $\widetilde{W}$ is the Fourier transform of the wall roughness correlation function defined in Eq. 2.41.

2.6.1 Results

We now examine the influence of the longitudinal correlation length (L_c/a) and that of the angular correlation (Φ_c), in reducing thermal conductivity. Both correlation lengths independently determine the two dimensional Gaussian width of the roughness Fourier transform $\widetilde{W}(\kappa, m)$ defined in Eq 2.41. From the attenuation relationship in Eq. 2.38, we see that strong surface scattering requires the change in phonon wave number upon scattering to lie within the Gaussian width. The inverse of longitudinal correlation length $(L_c/a)^{-1}$ is proportional the spatial width of $\widetilde{W}$ along the κ-axis while Φ_c^{-1} is proportional to the spatial width along the transverse wave number axis. Thus, a short correlation length increases the phase space for effective multiple scattering, allowing more phonons to participate in the process. A large correlation length reduces the roughness spectrum to a delta-like function. Such roughness can only scatter very long wavelengths, which do not

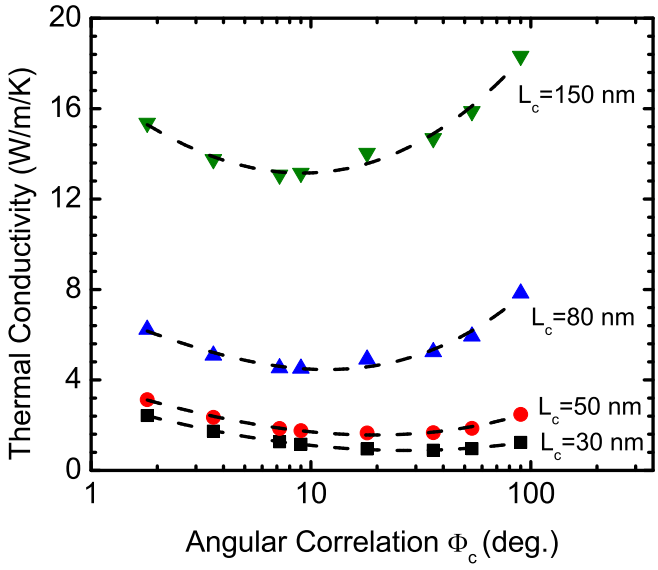

Figure 2.10: The effect of longitudinal roughness correlation length (L_c) and the circumferential roughness correlation angle (Φ_c) on thermal conductivity of a 40 nm diameter wire at 300 K. The RMS height of roughness is assumed to be 2 nm and wire length to be 2 μm with a Dirichlet boundary condition

contribute significantly to thermal transport. Figure 2.10 shows thermal conductivity calculated at 300 K for a wire of diameter 40 nm, length 2μm at different longitudinal and angular correlation (on x-axis) lengths. We observe a much more dramatic reduction in thermal conductivity with a decreasing longitudinal correlation length when compared with that for a varying angular correlation Φ_c.

The reason for the greater impact of L_c as compared to Φ_c is as follows. At a given frequency, the probability of a particular mode transforming into incoherent modes upon scattering is higher when the angular separation of the "permitted" incoherent channels ($\Delta\kappa$) is lower. It can be geometrically shown that for a mode incident on the boundary at angle θ_n to its normal, the angular separation with the closest available incoherent channel is given by $\theta_{n+1} - \theta_n \propto (\omega a\ tan\theta_n/c)^{-1}$. At short correlation lengths L_c, phonon modes with high frequencies that are incident at grazing angles (away from the zone center) are scattered strongly while modes with high normal inci-

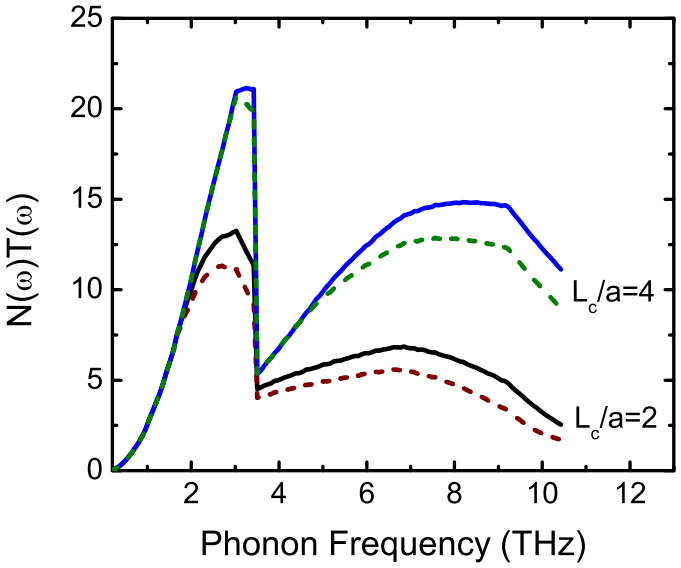

Figure 2.11: Effective transmission of the phonon spectrum $N(\omega)\overline{T}(\omega)$ for the cases L_c/a=2 and L_c/a=4. Solid lines represent angular correlation of $\Phi_c = 22.5^0$ while dashed lines represent $\Phi_c = 60^0$. The RMS height is fixed at 1.5 nm with the diameter at $a = 40$ nm.

dence (near the zone center) are least scattered. Since modes away from zone center predominantly contribute to transport, the effect of the longitudinal correlation length on thermal conductivity is more pronounced.

The role of angular correlation is quite different. At any given frequency, the sum of squares of the longitudinal and the transverse wave numbers is constant. Thus, the effects of the corresponding correlations are complementary. The angular roughness correlation attenuates modes near the zone center more effectively than ones away from the zone center. Since modes near the zone center contribute minimally to thermal conductivity, the angular correlation has a lesser overall impact on thermal conductivity. Further, Fig 2.10 shows that thermal conductivity has a minimum over the range of Φ_c. This is explained by considering the distance traveled by the wave, d in the $r - \phi$ plane between two subsequent reflections at the boundary. If the angular correlation length $a\Phi_c$ is very small compared to d or if $a\Phi_c$ is very large compared to d, mode attenuation is minimum and peaks in between.

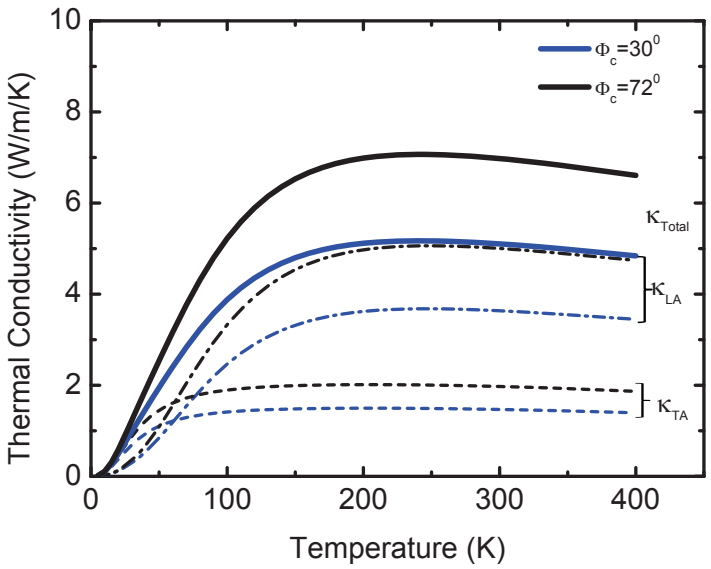

Figure 2.12: The effect of circumferential roughness correlation on thermal conductivity of a wire. The RMS height of roughness is 2 nm, longitudinal correlation length is 80 nm and wire length of 2 μm. The contribution of LA modes (in dash-dot lines) and TA modes (in dashed lines) are also shown for the two cases.

Figure 2.11 summarizes the effects of longitudinal and angular correlations on the phonon spectrum $N(\omega)\overline{T}(\omega)$. This spectrum is representative of the percentage contribution of phonons to the thermal conductivity across the frequency band. From the above discussion, we conclude that higher frequency phonons are more affected by L_c rather than Φ_c which can be clearly observed in the phonon spectrum. We further see that as the longitudinal correlation length decreases, the effect of Φ_c becomes more pronounced. The temperature trend of thermal conductivity in Fig. 2.12 shows the effect of circumferential roughness on contributions of longitudinal and transverse modes respectively.

2.7 Conclusion

The model described above matches data from all three sets of measurements: VLS smooth wires, EBL rough wires and EE rough wires. The parameters used in fitting, the roughness height and correlation length compare well with

experimentally determined values. Despite the reasonable match, we would like to point out a few deficiencies that we seek to address in future work as well as their implications. The use of the Bourret approximation is the most critical assumption. Dening a range of validity is not straightforward in this case and there is no guarantee that the Bourret solution will converge to the actual solution even if such validity is satised. However, the Bourret approximation does impose less restrictive conditions compared to the Born approximation, especially on the phonon wavelength in comparison with the roughness correlation. The latter requires that the wavelength be larger than the correlation length, which is easily violated for room temperature phonon transport. Thus, future work should carefully consider higher-order scattering terms while still focusing on wires of $\sim$50 nm in diameter. Another subtle issue is that the scattering cross section depends Another subtle issue is that the scattering cross-section depends on the second moment of the Green function and not the first statistical moment that we have used in this work. Finally, the roughness statistics in actual wires is likely to be non-Gaussian and may follow a power law. This requires further experimental data but should be relatively easy to consider once such data becomes available.

CHAPTER 3

ROUGHENED NANOWIRE ARRAYS USING METAL ASSISTED CHEMICAL ETCHING

Over the last twenty years, silicon nanowires have been continuously explored for wide range of applications in nano-electronics [70], photovoltaics [71, 72, 73], high capacity Li-ion battery anodes [74, 75] and thermoelectrics for energy conversion [3]. Controllable fabrication of the nanowires with desired morphology, doping and surface characteristics is primary requisite their application in the device technologies. Numerous methods, both bottom-up and top-down techniques have been developed for nanowire fabrication. In particular, electroless wet etching techniques have gained considerable attention in the recent years for cost-effective fabrication of large scale Si nanostructures. One of these techniques is metal-assisted chemical etching [76, 77, 78], an electrochemical process in which a mixture of an acid (HF) and an oxidant (H_2O_2) is used to etch Si in the presence of metal (Au). In contrast to VLS-based NW growth techniques, metal-assisted chemical etching (MacEtch) is a low-cost method since the processing can be done at room-temperature conditions. Further, the nanowires obtained by MacEtch acquire the crystallographic orientation of the starting Si substrate irrespective of their diameters. MacEtch can generate high-aspect ratio (> 100), vertically aligned NWs.

In a typical MacEtch process, a silicon substrate partially covered with a metallic pattern is introduced into an etchant solution comprising of HF and an oxidizing agent H_2O_2. A highly anistropic etching proceeds along the metal-Si interface producing three-dimensional Si structures, mimicking the initial metallic pattern [76]. For nanowire fabrication, the metallic pattern can be generated using several self-assembly techniques of thin metal films. Self-assembled patterns offer high-resolution sub-100 nm templates without any need for expensive lithographic processes [79, 80]. In this work, we generate metallic patterns for Si MacEtch using thin-film dewetting. Thin-

film dewetting is a scalable and robust process for creating self-assembled monolayers of metal nanoparticles in the 10 - 500 nm size range. A metallic thin-film deposited on the substrate, followed by a thermal annealing step activates thermal grooving in the thin film resulting in the formation of individual nanoparticles.

The structural properties of the nanowires fabricated by MacEtch such as diameter, length, orientation, morphology, porosity etc. depend on the etchant solution composition and quality of the thermal dewetting. We develop a controllable and repeatable process technology to generate NW arrays with consistent structural properties through exhaustive characterization of wire morphology and its dependence on the etching parameters. Control on the surface roughness of the nanowires and the doping are of primary importance in the study, as they directly affect the thermoelectric properties of these wires. This chapter provides a basic overview of the SiNW fabrication process flow in Section 3.1. The surface roughness control of the NW arrays with several electron microscopy studies is presented in Section 3.2. We then study the dependence of the morphology of MacEtch SiNWs with the doping concentration of the starting Si substrate in Section 3.3. Finally, we present the ex-situ doping technique of the SiNWs in Section 3.4.

3.1 Process overview

The process flow of SiNW fabrication and roughening is shown in Figure 3.1. The process involves four steps – (a) silver film dewetting (b) Gold deposition and Ag lift-off (c) Etching in HF+H_2O_2 solution (d) post-roughening step. Each step is briefly described in this section.

The process starts with deposition of thin silver (Ag) film ($\sim$10 nm using e-beam evaporation) on lightly-doped Si substrate (Fig. 3.1 (a)). The resistivity of the starting substrate is usually $\rho \sim 1-5$ Ω-cm. Subsequent thermal annealing of Ag film at 350^0C for 4 h under 3×10^{-7} Torr pressure thermally dewets the Ag, forming truncated spherical particles (contact angle $> 90^0$) on the surface. The particle size and the inter-particle spacing depends on the thickness [81] of the Ag film as well as the annealing temperature and

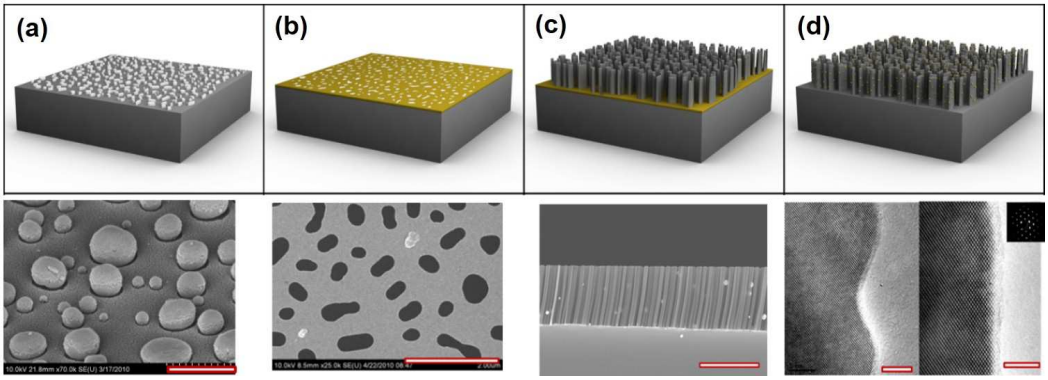

Figure 3.1: (a) Thermal dewetting pattern of silver droplets after annealing 10 nm Ag film for 350^0C for 4 hours. (b) The gold mesh fabricated by Ag lift off serves as pattern for subsequent etching. (c) Etching in the solution of HF and H_2O_2 produces vertically aligned nanowire array (d) The Au droplets are sputtered on the nanowire sidewalls and a subsequent etching for short time produces controllable surface roughness on the nanowires as shown in HR-TEM images. The scale bars represent a length of (a) 500 nm (b) 2 μm (c) 2 μm (d) 2 nm

time. The dewetting results in Ag nanoparticles with diameters in the range of 10 - 80 nm and areal coverage of 32 - 42% range. The particle size is dependent on the deposition rate as well as the initial film thickness as it affects the thin-film nucleation and growth kinetics. For the conditions described above, we obtained particles with average diameter 80 - 150 nm.

The Ag particles are used as a shadow mask to form a gold mesh (10 nm Au deposited by e-beam evaporation shown in Fig. 3.1 (b)). The lift-off of Ag particles is achieved by sonicating the samples in a selective etchant (NH_4OH(32%):H_2O_2(30%):methanol = 1:1:2; v:v:v). Silver lift-off is a limiting step for producing smaller diameter NWs (sub-100 nm), especially when the particles height is comparable to the Au film thickness. In order to address this issue, we increase the height of Ag particles by predepositing a thin-oxide layer (10 - 15 nm). During lift-off, we use a BOE (buffered oxide etch) step to etch the underneath oxide layer. The oxide undercut under the silver particles produces pedestal-like structures that greatly facilitate the lift-off process.

The Si substrate covered with gold mesh is now introduced into the etching solution consisting of HF and H_2O_2. An electrochemical reaction is catalyzed

at Au-Si interface etching Si underneath the metal. Briefly, metal-catalyzed reduction of H_2O_2 at the silicon-metal interface injects holes into Si valence band thus locally oxidizing silicon at this interface, which is subsequently dissolved by HF acid. The balance between hole injection (by H_2O_2) and hole consumption (by HF) maintains holes localized at the metal-substrate interface and consequently, directional etching is achieved with non-porous single crystalline features being generated. The highly anisotropic etching proceeds along metal-Si interface producing vertically etched silicon structures mimicking the metallic pattern on the Si surface as shown in Fig. 3.1(c). The etching rate is $\sim$ 1.2 μm/min for etching solution of [HF]: [H_2O_2] = 13:2. We controllably generate SiNWs of areal coverage ranging from 25-40 %, nanowire lengths (L) from 0.5 μm-2 μm and diameters (D) from 90-150 nm with a tight standard deviation of Δ D$\sim$ 13% in a given array. The resulting NWs are solid and single-crystalline as evidenced from the transmission electron micrographs (TEM).

3.2 Nanowire Roughening

The as-synthesized nanowires are then roughened by a second-etching step (post-roughening step). We deposit Au nanoparticles on sidewalls of the NWs by all-angle sputtering and a short MacEtch is performed to drive these particles into the NWs for few nanometers. The etching time in the post-roughening step will determine the magnitude of roughness generated on the NW sidewalls. A dilute MacEtch solution composed of HF(49%):H_2O_2(30%):H_2O = 1:1:24 (v:v:v) is used for the post-roughening step.

Roughness of the nanowires was determined by high-resolution transmission electron microscopy (HR-TEM). A double-tilt holder was used to tilt the nanowire to [110] zone-axis enabling high resolution imaging of the Si/native-oxide boundary. Several atomic resolution images recorded along the length of a nanowire as shown in Fig. 3.2. The images are stitched together to generate the roughness profile of the nanowire over a length of $\sim$500 nm, with the boundary being taken as the outmost edge of the lattice fringes. The boundary profile was fit to a linear function, considered to be the mean

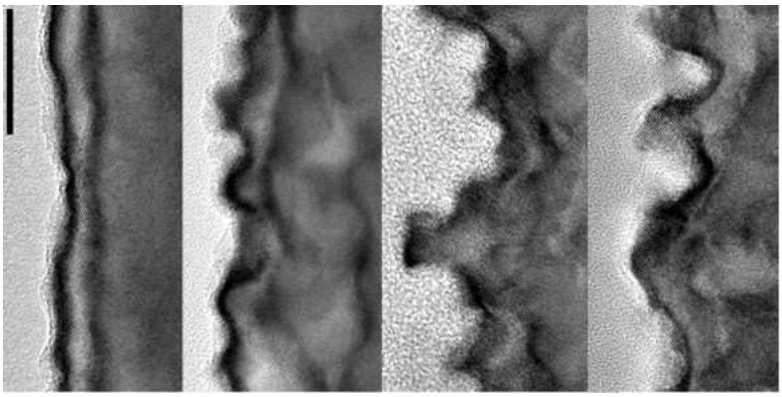

Figure 3.2: Bright field transmission electron micrographs of nanowires obtained by post-roughening process (etch times increasing from left to right: 2, 10, 16 and 20 seconds respectively); the scale bar is 10 nm).

surface. The RMS roughness and correlation length was calculated about the mean surface.

Figure 3.3 (a) shows the stitched roughness profiles $h(x)$ of wires taken from samples with different post-roughening times. The RMS roughness is calculated as $\sigma = \sqrt{\langle h^2 \rangle}$. This procedure was conducted for three nanowires from each array to obtain an average rms roughness for each sample. The average RMS roughness height for several samples is plotted as a function of roughening time (t_r) in Figure 3.3 (b). We fit a linear relation for σ and t_r and use this relation for roughness control. The post-roughening step yields controllable sidewall roughness with root-mean square (RMS) height ranging from 0.3 nm (for 3 sec etching) to $\sim$4 nm (for 20 sec etching).

We extract the correlation length of surface roughness by calculating the height-height correlation function of the roughness profile [82]. The correlation function defined as $G(\rho) = \langle [h(x+\rho) - h(x)]^2 \rangle$ is a real space statistical measurement that gives detailed information about the length scales of the system. The key features of $G(\rho)$ are that, typically, for $\rho > \zeta$ (we consider $\zeta = 30$ nm), $G(\rho)^{1/2} = \sqrt{2}\sigma$ and the correlation length can be estimated by first local minima of $G(\rho)$ as shown in Fig. 3.3 (c). The correlation lengths for all nanowires are in a range from 15 - 40 nm which is characteristic of the size of the Au islands used during the roughening process.

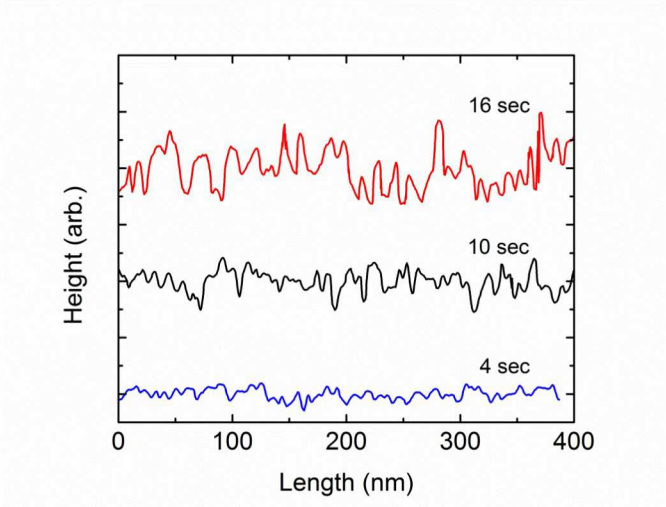

(a)

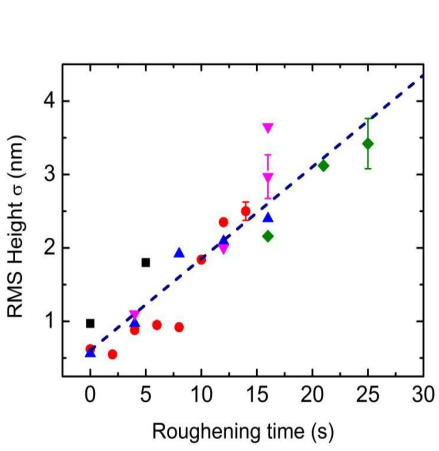

(b)

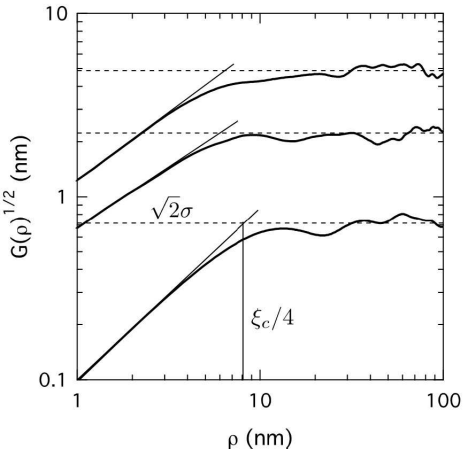

(c)

Figure 3.3: (a) The surface roughness profiles of wires for different etching times is obtained by stitching several HR-TEM images (b) Average RMS height of post-roughened nanowires as a function of etching time. Different symbols represent the wires from different batches. (c) Height-height correlation function $G(\rho)$ for three different roughness profiles.

3.3 MacEtch on degenerate silicon

Nanowires obtained from MacEtch on lightly doped Si substrates has been discussed in the previous section. In this section, we study the dependence of wire morphology on the doping concentration of the starting wafer. Specifically, we study MacEtch on degenerately doped Si ($N > 3 \times 10^{18}$ cm^{-3}), a doping concentration of specific interest to silicon thermoelectrics.

Several studies on MacEtch of degenerately doped Si wafers have found that the NWs tend to be porous for doping levels above 10^{18} cm^{-3}. Formation of porous nanostructures by MacEtch were reported for both p-type [83] and n-type [84] substrates comprising of single crystalline silicon surrounded by amorphous silicon and silicon suboxides. Hochbaum et.al.[85] also reported single crystalline mesoporous silicon nanowires from MacEtch of degenerately doped wafers using silver nitrate and HF. It is imperative to further explore the MacEtch parameter space in order to gain insights in controlling the porosity of degenerately doped silicon.

The formation of porous nanostructures using MacEtch has been attributed to the diffusion of holes outside of the metal-semiconductor interface and causing additional but reduced extent of etching in the areas outside the metal mesh pattern [83]. Another possible reason is the hole transport (thus pore formation) is more favorable in degenerately doped Si due to less band bending at the metal-semiconductor interface [85]. In our work, we study the porosity of NWs produced from highly doped substrates with varying the hole production and consumption rate by changing the [HF]:[H_2O_2] etchant ratio. Using very high ratio of [HF]/[H_2O_2] increases the hole generation process compared to the etch rate. When this condition is met, there will be little time for the injected holes to diffuse before the HF removal of Si^{4+}. Thus, increasing the rate of Si^{4+} removal process with higher [HF]/[H_2O_2] ratio can help to reduce hole transport and thus the formation of pores. Hence, we aim to study the variation in degree of porosity of NWs from high-doped substrates with the parameter [HF]:[H_2O_2]

Figure 3.4 shows the high magnification and low magnification TEM micrographs of SiNWs generated from p-type substrate (ρ= 0.001 -0.005 Ω-cm)

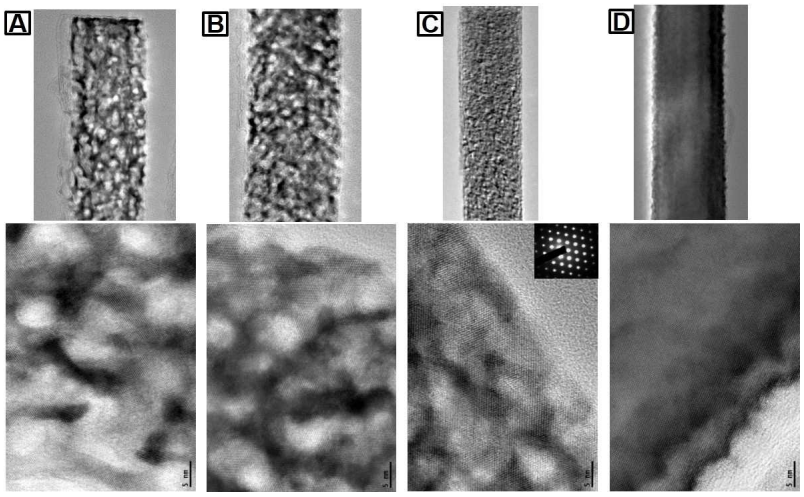

Figure 3.4: The degree of porosity of degenerately p-doped NWs decreases with dilution of HF solution as indicated in low mag and corresponding HRTEM images for [HF]:[H_2O_2] of (A) 10:1 (B) 20:1 (C) 30:1. A non-porous crystalline nanowire (D) is shown as comparison.

with [HF]:[H_2O_2] volume ratios from 10:1 to 30:1. The HR-TEM images of the nanowire etched using 10:1 [HF]:[H_2O_2] MacEtch solution (Fig. 3.4 (c)) clearly shows the presence of pores as indicated by sharp contrast in the image. Since TEM image is a projection of several atomic planes along beam direction, a lighter region is a representation of relatively lesser number of atomic planes, indicating porous regions. From Fig. 3.4, we find the porosity decreases with increasing [HF]: [H_2O_2] ratio. The nanowires are single crystalline and the porosity at 30:1 etchant concentration (Fig. 3.4 (c))is dramatically reduced to pore sizes of within $\sim$ 5 nm. A solid nanowire fabricated using MacEtch from lightly doped p-type (ρ= 1 Ω-cm) Si wafer is shown for comparison in Fig. 3.4 (d) which shows no intensity contrast as observed in the porous wires.

In addition to relative concentration of [HF]:[H_2O_2], we have found that etch time also changes the porosity. We observe that MacEtch SiNWs from highly doped n-type substrate ($\rho \sim 0.08\ \Omega$-cm) etched using 15:1 [HF]:[H_2O_2] exhibits higher degree of porosity when etching time is increases from 30 s to 60 s. Further, we have also observed a gradual change in porosity along the axis of the nanowire produced by MacEtch from these highly doped silicon wafers. Figure 3.5 shows the TEM images of three segments of a nanowire

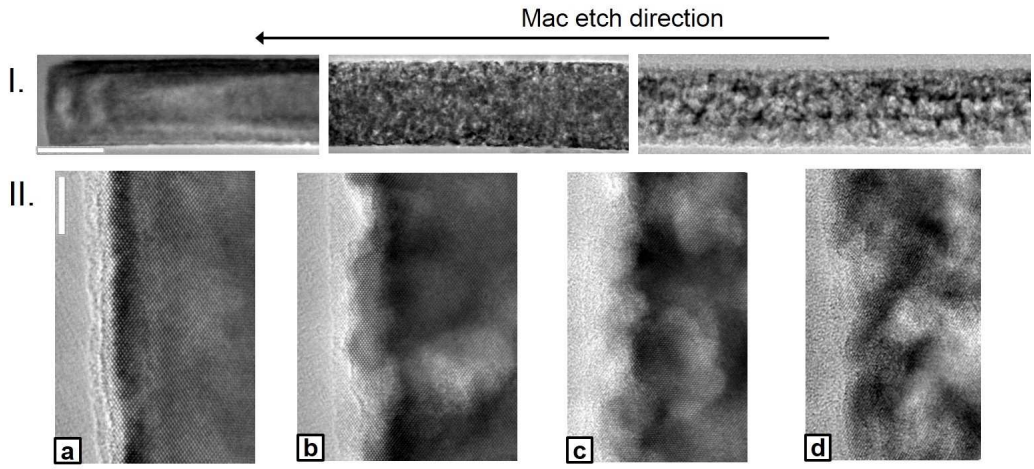

Figure 3.5: The porosity of the wire progressively decreases along the etching direction. (I) shows the low-magnification images of the wire from wire tip (d) to bottom (a). (II) shows the corresponding HRTEM images with (d) to (a) representing the etch direction. We also observe the boundary becomes smoother towards the bottom of the wire. The scale bars in (I) and (II) are 50 nm and 5 nm respectively.

produced from an n+ silicon wafer using [HF]: [H_2O_2] volumetric ratio of 10:1 after etching for 3 minutes. We observe a gradual increase in porosity along the axial length (3 μm) of the nanowire. The increase in porosity along the axis from the top to bottom of the wires may be due to the prolonged exposure of the tip and the middle parts of the wires in the etching solution [86].

3.4 Doping control of NWAs

Since, highly doped silicon nanowires of solid morphology are of primary interest for this study, we develop an ex-situ furnace doping technique to controllably dope the solid nanowires obtained from MacEtch on low-doped substrate. We employ spin-on dopants (SODs) to dope the entire NW array either p-type (boron) or n-type (phosphorus). Before going through the doping procedure, we first calculate the dopant diffusion characteristics in nanowire to design time and temperature conditions for doping.

For a Si nanowire covered by spin-on dopant of boron (say), the initial

concentration of the dopant of nanowire surface equals the solid-solubility of boron in Si (N_{sl}). We can calculate the dopant diffusion in the cross-section of the NW using Fick's law in a cylindrical wire of radius a

$$\frac{1}{r}\frac{\partial}{\partial r}\left(r\frac{\partial C}{\partial r}\right) = \frac{1}{D}\frac{\partial C}{\partial t}$$
$$C(a,t) = N_{sl}C(r,0) = 0 \tag{3.1}$$

where C(r,t) is concentration of dopant inside the wire at time t and D is dopant diffusivity in silicon at temperature T. The solution for Eqn. 3.1 is given by

$$\frac{C(r,t)}{N_{sl}} = 1 - 2\sum_{k=1}^{\infty}\frac{J_0\left[\lambda_k(r/a)\right]}{\lambda_k J_1(\lambda_k)}exp\left(-\frac{D\lambda_k^2}{a^2}t\right) \tag{3.2}$$

where λ_k is the k^{th} zero of the Bessel function J_0. By tuning the temperature (thus changing D) and doping time, we can control the dopant concentration in the NW. We find the predeposition of dopant at 950^0 C over 10 min yields nanowire doping concentrations above 10^{19} cm^{-3} for boron doping. Hence we choose 950^0 C as the doping temperature for both boron and phosphorus diffusion.

3.4.1 Doping via SODs

The as-etched Si nanowires produced by MacEtch of lighty doped wafer ($N_0 \sim 7 \times 10^{16}$)are doped in an ex-situ manner using spin-on dopants. SODs are spun onto the wire array and annealed at doping temperature in a Lindberg furnace for required time to introduce dopants into the wires. Before the SODs are spun on the arrays, we deposit thin layer of PECVD oxide on the sidewalls of NWs which serves two purposes – (a) the surface oxide layer protects the surface roughness on NW sidewalls generated by post-roughening step and (b) the PECVD layer acts as a barrier to dopant diffusion and thus by varying its thickness, we can control the dopant concentration into the NWs. Thus PECVD oxide thickness serves as the control parameter for doping in this work while temperature and doping time are kept constant.

Spin-on dopants of boron (borofilm) or phosphorus (phosphorofilm from

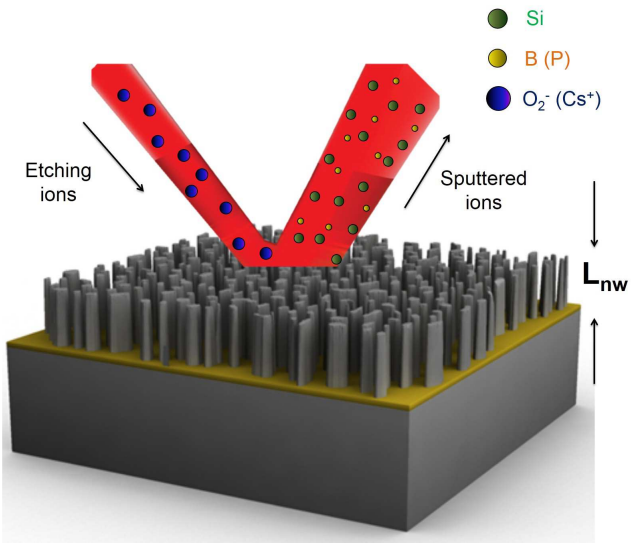

Figure 3.6: Schematic showing the dopant depth profiling of nanowire arrays. The etching ions are is Cesium or oxygen ions for profiling n-type or p-type NWs respectively.

Filmtronics©) are used for p-type or n-type respectively. SODs are spun on the NW arrays with PECVD oxide layer at 3000 rpm for 30 s. SOD is then baked at 270^0C for 10 min. The dopant diffusion is activated by annealing the samples at 950^0C for 15 min, called the predeposition step. The borosilicate / phosphorosilicate glass formed as a part of annealing are removed by BOE etch for 3 min. We observe that the nanowire roughness is preserved after this doping step. Finally, we drive-in the dopant at 975^0C for another 10 min.

The doping in the nanowires is characterized by dopant depth profiling by secondary ion mass spectroscopy (SIMS). The primary ion beam for depth profiling is either Cs^+ and O^{2-} for phosphorus (n-type) and boron (p-type) doped wires respectively as shown in Fig. 3.6. A standard ion-implanted sample of known dose is also measured at the same alignment conditions to extract relative scaling factor (RSF) for the dopant species. The crater depth is then measured using profilometry to convert the etching time to depth. We assume an uniform etch rate of the NWs due to the primary beam (10 keV) for this conversion. Figure 3.7 shows the depth profile of boron-doped NW arrays, doped with several thickness of barrier oxide layer. First, we observe that the doping is uniform across the length of the nanowires with the depth profile sharply declining to substrate dopant concentration after a depth that

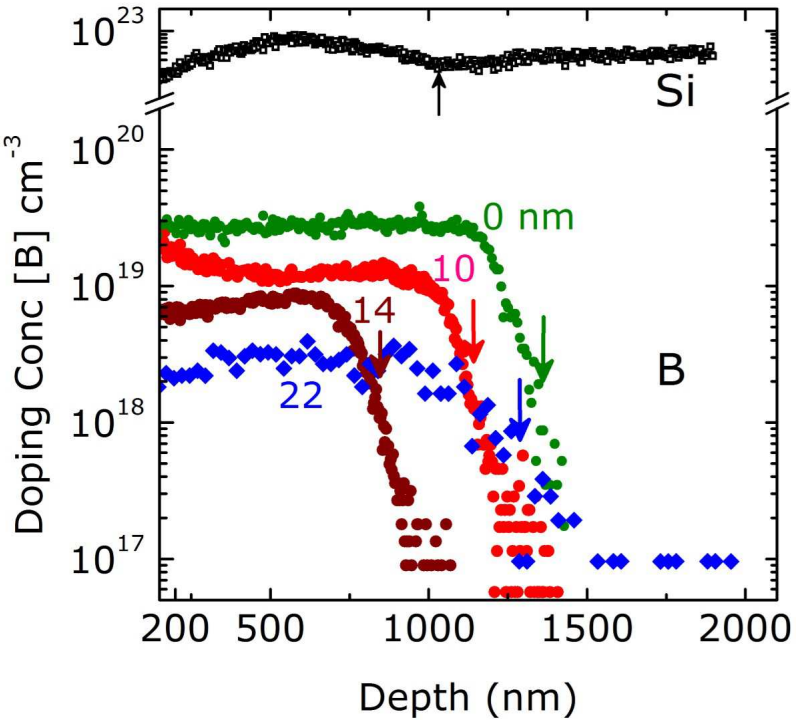

Figure 3.7: The SIMS depth profile of the boron-doped nanowire arrays, doped with PECVD barrier layer of thickness labeled against each profile. The arrows represent the length of NW array measured from SEM before the profiling.

matches with the SEM length of the nanowire arrays. Second, we observe the magnitude of the doping concentration comes down with the thickness of the barrier layer. Thus, by varying the thickness of PECVD oxide barrier layer in the range 10 nm 25 nm, we achieve a controllable range of doping concentration in NW array from 2×10^{19} cm^{-3} to 4×10^{18} cm^{-3}.

3.4.2 Tip doping of NW arrays

One of the key limitations to device technologies based on vertically aligned nanowires is the inability to form low resistance ohmic electrical contacts at the top of the wires. The typical wrap-around contact length in the devices is $\sim$ 100 nm and assuming a specific contact resistivity of $\rho_c'' = 5 \times 10^{-4}$ $\Omega - cm^2$, the contact resistance itself dominates the array resistance (typical array lengths of 2μm). This limitation causes high losses in device efficiencies

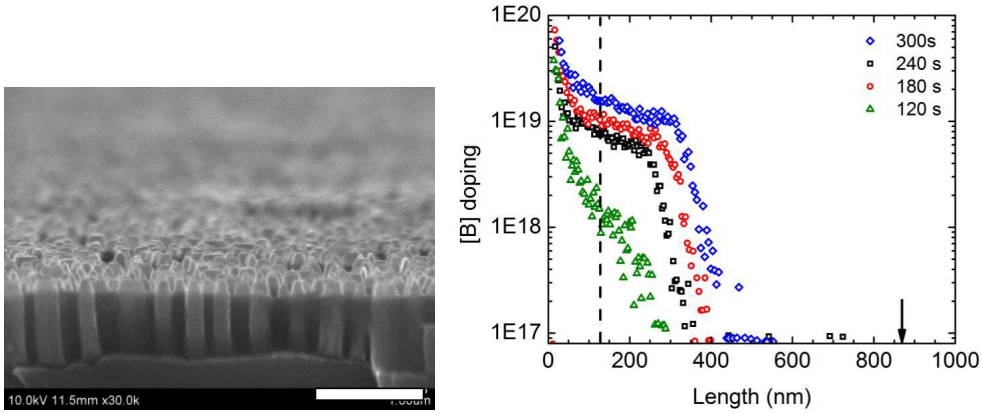

(a) (b)

Figure 3.8: (a) SEM image showing the nanowire tips exposed after RIE etching of spin-on glass spun over the NW array. The scale bar is 1μm. (b) SIMS depth profile of NW array of length 850 nm.

due to joule heating at the contacts. For a thermoelectric module used in waste energy harvesting, the device efficiency halves for an order increase in ρ_c'' [87]. It is known that the specific contact resistivity can be reduced by an order in magnitude by increasing the doping near contacts by an order. Hence, its imperative to dope the NW tips above 10^{20} cm^{-3} without affecting the doping in the rest of the array. We achieve the tip doping using a two-step process using spin-on glass (SOG) and spin-on dopants (SOD) described in this section.

Initially, the nanowire arrays are filled with spin-on glass by spinning SOG at 2000 rpm for 30 s. The SOG is baked on hot plate at 110^0 C and 270^0 C for 90 s at each step. The SOG is then cured in nitrogen environment for 1 h at 350^0 C. The initial thickness of SOG layer is usually $\sim$ 1.5 μm for the conditions described above. We then etch the SOG using Freon gas (CF_4) by reactive ion etching (RIE) till the SOG thickness typically $\sim$100 nm below the tip of the nanowires. Figure 3.8 (a) shows a scanning electron microscope image of nanowire tips exposed in SOG filled NW array of length 850 nm.

After exposing NW tips using RIE, we then spin a layer of boron SOD on the top of SOG covering the nanowire tips. We follow the same steps as nanowire doping, but the doping time is now reduced to less than 5 min at

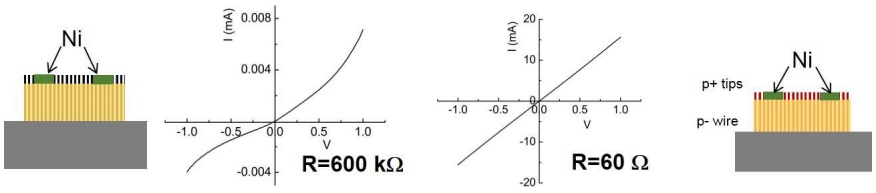

(a) (b)

Figure 3.9: (a) Electrical resistance measurements before (a) and after (b) tip-doping shows improvement in contact resistivity by four orders.

950^0 C since the purpose of tip-doping is dope only the tips without affecting the doping in the rest of the wires. The section of wires covered by SOG are not doped in this process. We confirm this by conducting dopant depth profile analysis using SIMS. Figure 3.8 (b) shows the SIMS depth profiles of NWs (of length 850 nm) doped at the tips by boron. For this analysis, we expose $\sim$ 150 nm of NW tips for doping. We observe that the tip doping is successful with the dopant diffusion getting shallow with the doping time.

We further test the success of tip doping by conducting a two-probe electrical measurement on the NW array. We deposit nickel pads (thickness of 200 nm) as the electrical contacts on SOG filled NW arrays. The Ni contacts are then annealed at 320^0 C by rapid thermal processing (RTP) to facilitate ohmic contacts. Figure 3.9 shows the results of electrical measurements of the NW arrays before and after tip-doping. We find a four order decrease in the specific contact resistivity as a result of tip-doping.

CHAPTER 4

FREQUENCY DOMAIN MEASUREMENTS OF THERMOELECTRIC PROPERTIES

4.1 Introduction

The measurement of cross-plane Seebeck coefficient of micron-scale thin films is challenging as it requires precise measurement of temperature and voltage simultaneously at the interfaces of the film. Cross-plane measurements are further plagued by non-desirable contributions from the supporting substrate, parasitic heat flow paths and non-ideal thermal/electrical contacts. One of the widely employed technique for cross-plane ZT measurement of thin films is the transient Harman technique [88]. In this technique, a DC current pulse applied across the film sets up the thermal gradient (ΔT) via Joule heating. A current (I) also leads to ohmic (V_R) and Peltier (V_0) voltages across the film. When current is turned off, V_R decays within the dielectric relaxation time but V_0 decays according to the thermal time constant. The resulting Seebeck voltage V_0 follows the transient thermal decay of all the elements along heat flow path. However, the fast thermal response of thin films requires high-speed detection of the small transient Seebeck voltage V_0 rendering the Harman method quite difcult to apply to thin films [89]. Even the measurements of ΔT across the film is offset by non-uniform Joule heating in the film and parasitic heat losses through the contacts [90, 91], often requiring complex thermal simulations to characterize these effects. Further, the definition of the Seebeck effect requires measurement of the open-circuit voltage across an applied ΔT in absence of any current, which calls in question the accuracy of these closed circuit measurements.

In this work, we employ frequency domain technique similar to 3ω-measurements where the temperature field across the structure is set up by AC Joule heating in an external heating element. The open circuit Seebeck voltage de-

veloped across the film, the substrate and the contacts have distinguishable frequency response due to variable heat penetration in each layer. The architecture for 3ω measurements even allows mm^2-scale thermal contacts onto the investigating films which made contact contribution in our measurements negligible. This technique has been previously applied for room temperature thermoelectric measurements of SiGe superlattices [92]. We show that this technique yields accurate measurements of Seebeck coefficient in the temperature range 25 K 500 K using appropriate control of heating frequency range based on the thermal diffusivity of Si across in this temperature range. We also extend the application of this technique to generic nanostructures by developing new techniques for the data extraction to analyze cross-plane S and k simultaneously.

We discuss the principle of frequency domain measurements in Section 4.2 followed by discussion of differential measurements to extract Seebeck coefficient and thermal conductivity of the nanowire arrays. We then proceed to validity limits of the technique in temperature dependent measurements in Section 4.3

4.2 Principle of Measurement

We employed a frequency-domain technique to measure the Seebeck coefficient (S) and the thermal conductivity (k) of the nanowire arrays, similar to the 3ω technique [93] used for measuring the thermal conductivity of thin-films. Fig. 4.1 (a) shows the schematic of the measurement platform. In principle, a sinusoidal heating current of frequency ω through the top metal heater sets up a temperature gradient across the NW-array (ΔT_{NW}), the insulating oxide layer (ΔT_{ox}) and the substrate (ΔT_{sub}), each oscillating at a frequency 2ω. Since the Seebeck voltage follows the temperature field, the voltage drop across the NW-array ($\Delta V_{NW} = S_{NW}\Delta T_{NW}$) and the substrate ($\Delta V_{sub} = S_{sub}\Delta T_{sub}$) also oscillate at 2ω. By measuring the 2ω component of the voltage between the metallic pads as shown in Fig 4.1 (a) using a lock-in amplifier, we obtain the open-circuit Seebeck voltage $V_{2\omega}(=\Delta V_{sub}+\Delta V_{NW})$. The temperature at the heater ($\Delta T_{h,NW} = \Delta T_{NW}+\Delta T_{ins}+\Delta T_{sub}$) is ob-

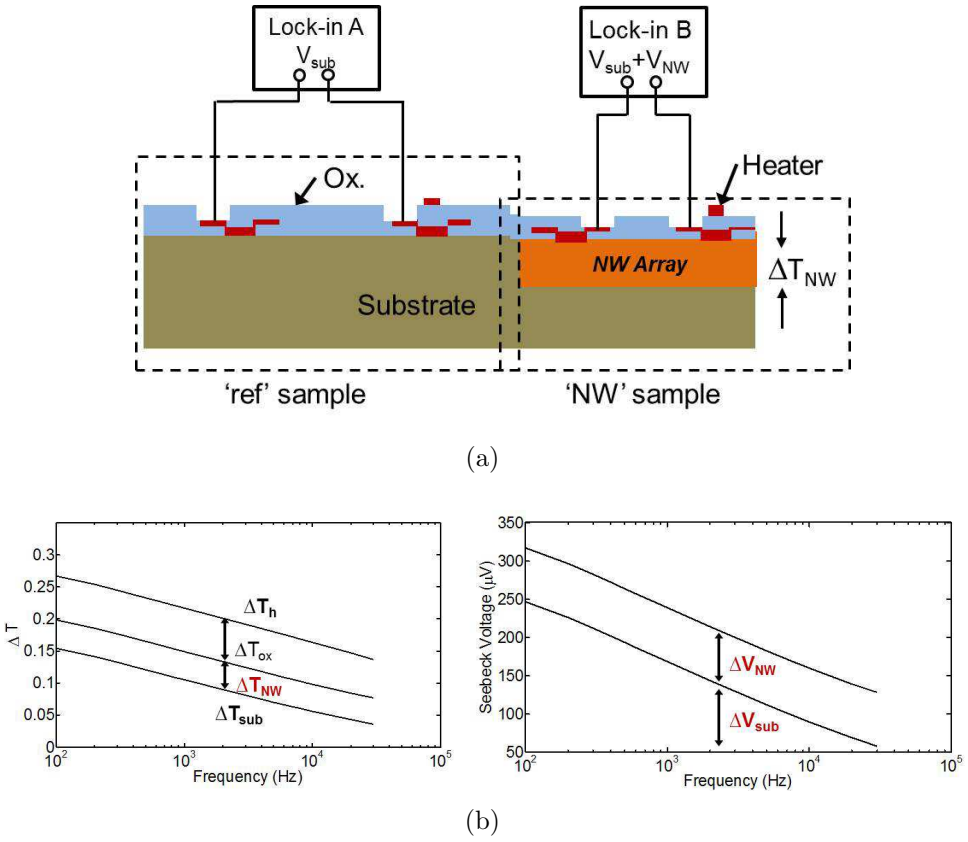

Figure 4.1: Principle of differential measurements shown in (a) schematic and (b) simulation of temperature and voltage signals for 'ref' and 'NW' samples.

tained by measuring the 3ω voltage signal across the heater arising from its temperature dependent resistance.

4.2.1 Differential measurements

The measurement provides the total temperature drop across the insulator, the NWA and the substrate and total voltage drop across the NWA and the substrate. In order to extract the Seebeck coefficient of NW arrays, we need to subtract the contributions from the substrate and the insulator by conducting a differential measurement on the 'reference' sample comprising of the substrate with the same insulation layer shown in Fig. 4.1 (a). Thus we differentially obtain the temperature drop ΔT_{NW} $=\Delta T_{h,NW}$ $-\Delta T_{h,ref}$ and

the Seebeck voltage across the NW array ΔV_{NW} =$\Delta V_{2\omega,NW}$-$\Delta V_{2\omega,ref}$. Figure 4.1 (b) shows the simulated results of temperature and voltage signals obtained for NW array of length 2μm on low doped silicon substrate. Using the differential temperature and voltage drop across the NW array, we obtain the Seebeck coefficient of NWA as S_{NW}=$\Delta V_{NW}/\Delta T_{NW}$. We can also extract the thermal conductivity of the NW array simultaneously as $k_{array} = P/(2bl\ \Delta T_{NW})$ where l and $2b$ are the length and the width of the heater line with heating power P. The nanowire thermal conductivity can be obtained using the effective medium theory[94] by subtracting the conductance contribution from the spin-on glass (SOG) as $k_{NW} = (k_{array} - k_{SOG}(1-x))/x$ where x is the areal fraction of nanowires in the array. We measured the thermal conductivity of pure SOG (200 nm thick film) using the 3ω technique to be 0.34 W/mK. It should be noted that the differential technique can be applied only for heating frequencies where one-dimensional heat conduction through the array is the valid. The conditions to met for the validity of the technique across different temperatures is widely discussed in the next section.

4.3 Limitations in high diffusivity media

The key assumption in the differential measurement is that the contribution of substrate to the measured Seebeck voltage is similar in both 'NW' and 'ref' samples for same heating power P. This condition holds in the heating frequency range at which one-dimensional heat conduction occurs across the insulator layer and the NW array. The differential voltage drop from the signals from 'ref' and 'NW' samples can only be obtained from the frequency range where the signals decreased linearly with logarithm of the heating frequency. This is the frequency regime where (a) the thermal penetration ($\delta = \sqrt{2D_{th}/\omega}$ where D_{th} is the thermal diffusivity of Si) into substrate is within the substrate thickness (t_{Si}=550 μm) in both the ref and NW samples and (b) one-dimensional heat conduction occurs across the NW array. These two conditions (a) and (b) place the lower limit and the upper limit of frequency range in which differential measurements can be applied. We now discuss each condition separately.

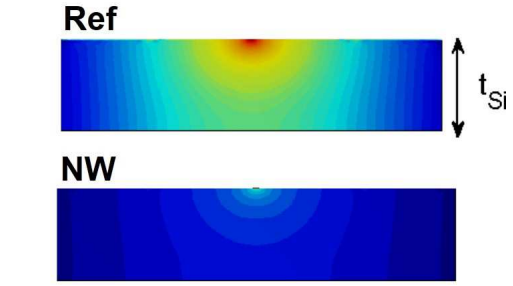

(a)

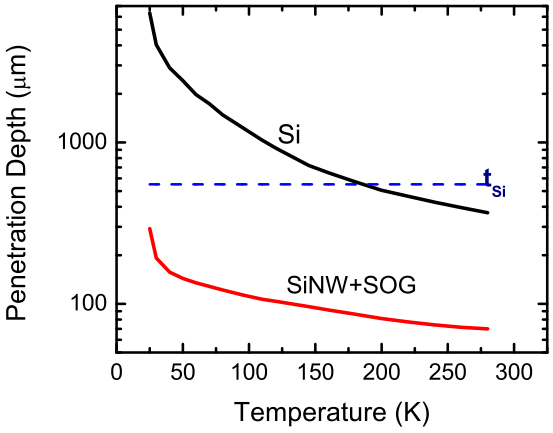

(b)

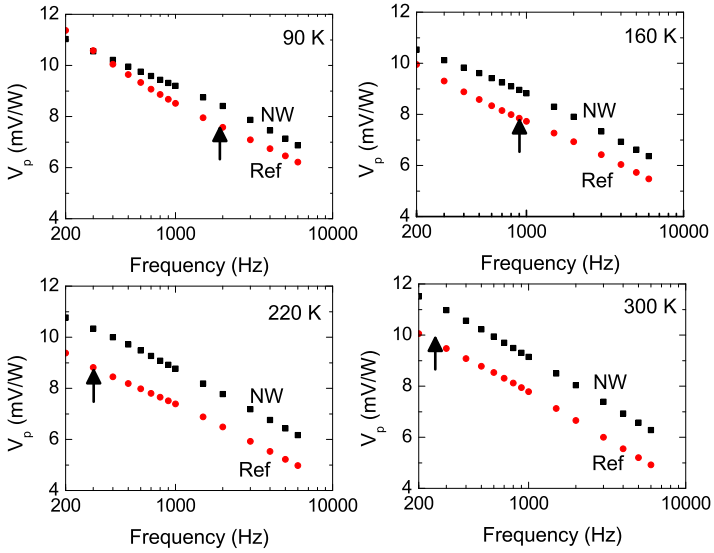

(c)

Figure 4.2: (a) Steady periodic temperature simulation in 'ref' and 'NW' sample in highly diffuse substrate. (b) The penetration depth in silicon as a function of temperature at heating frequency of 200 Hz. (c) The measured data of power normalized Seebeck voltage at several temperatures.

When heat penetration depth is comparable to or exceeds the substrate thickness, the temperature (and thus voltage) response at the substrate surface is sensitive to the boundary conditions in either samples (heat flux q"=0 at bottom). Figure 4.2(a) depicts the heat penetration into the substrate for 'ref' and 'NW' sample when $\delta > t_{Si}$ for highly diffuse substrates. Due to different heat penetration depths in 'ref' and 'NW' samples, we cannot apply differential measurements when the heat penetration depth in ref' is comparable to or greater than substrate thickness. Figure 4.2 (b) shows the thermal penetration in Si and SiNW array (thermal conductivity of SOG-NW composite ∼6 W/mK at 300 K) with temperature at frequency 200 Hz. Thus, we cannot use frequencies below 200 Hz for differential measurements below 200 K since$\delta > t_{Si}$. The same argument applies when the penetration depth into the substrate is comparable or greater than the heater length ($L_h = 600\mu$m for our samples).

The measured data in Fig. 4.2 (c) shows that the valid frequency range (indicated by arrows) for application of differential measurement at 90 K, 160 K and 220 K are f >2000 Hz, f >800 Hz and f >300 Hz respectively. For T <25 K, the thermal penetration depth in Si is beyond t_{Si} for entire range of lock-in amplifier frequencies, thus limiting the application of this technique below 25 K.

The upper limit of valid frequency range for differential measurements (f_{crit}) occurs when the penetration depth is confined within the length of the NW arrays. This condition generally arises at high frequencies ($f_{crit} = 6000$ Hz for NW composite thermal conductivity ∼6 W/mK). In this case, the heat diffusion in NW array can longer be considered one-dimensional thermal diffusion.

4.3.1 Finiteness of heating element

The original derivation of 3ω technique [93] considers line-heater on semi-infinite substrate. In highly diffuse samples (Si at low temperatures), it is important to consider the finiteness of the substrate and finite heater. In ad-

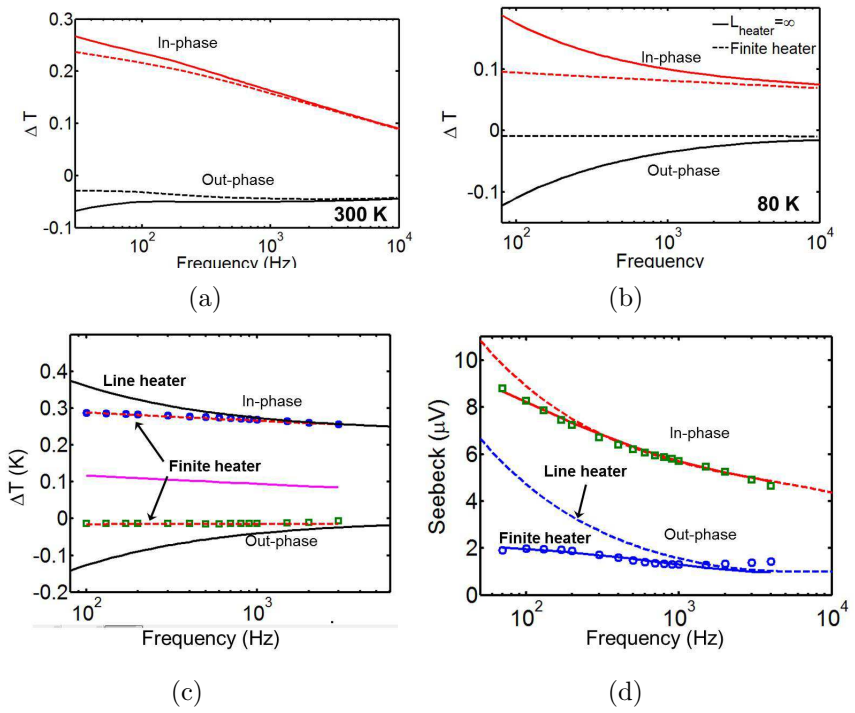

Figure 4.3: Simulations showing the deviation in temperature rise of heater using line heater assumption relative to finite heater of length 600μm at (a) 300 K and (b) 80 K. The deviation in the fits produced by line heater assumption to the measured data of (c) heater temperature rise and (d) Seebeck voltage.

dition, it is not possible to fabricate long heaters on the small size of nanowire samples used in this work. Appendix A gives a detailed derivation of three-dimensional heat diffusion for the case of finite heater on finite substrate.

Figure 4.3(a) and 4.3 (b) show the deviation of line heater assumption from the finite heater assumption (L_h600 μm) in heater temperature rise (ΔT) at 300 K and 80 K respectively. The thermal diffusivity in Si at 80 K is 40 times higher than that at 300 K. Thus higher penetration depths in Si at 80 K in comparison to heater length throughout the entire frequency range shown in Fig. 4.3 (b) renders line heater assumption invalid. Figure 4.3 (c) and 4.3 (d) compares the fit of raw data with line heater assumption and finite heater calculation. This demonstrates the importance of considering the 3D heat diffusion model in Appendix A to analyze the signals in this work.

CHAPTER 5

THERMOELECTRIC MEASUREMENTS OF NANOWIRE ARRAYS

5.1 Thermal conductivity with roughness

In this chapter, we report the measurements of thermoelectric properties of the MacEtch nanowire arrays, discussed in the previous chapter. Our study specifically focuses on the role of the surface roughness and the wire morphology on the thermoelectric properties. Since, the role of surface roughness in reduction of thermal conductivity of SiNW is of specific focus in thermoelectrics of rough silicon nanowires, we start with a systematic study of thermal conductivity reduction with nanowire roughness. We measured the thermal conductivity of the roughenend nanowire arrays using time-domain thermoreflectance [82] and single nanowire measurement using a microfabricated platform [95]. Figure 5.1 (a) shows the TDTR measurement [96] of thermal conductivity of NW arrays with the RMS roughness (σ) characterized by HR-TEM. We observe a definite reduction in k_{NW} with roughness down to $\sim$10 W/mK at σ $\sim$4 nm. The data shows that the thermal conductivity of MacEtch wires is reduced below the Casimir limit by a five times. While the data is encouraging, more thorough characterization of wire morphology is desired before attributing the phenomenon to surface roughness effects. The details of the measurement and the smaple characterization can be found in Ref. [82].

In order to understand the physics of phonon scattering in roughened nanowires, low temperature measurements of thermal conductivity are required for NWs of known roughness statistics. To this purpose, we conducted thermal conductivity measurements on single nanowire of known roughness from 15 K - 300 K using a microfabricated platform described in Refs. [95, 97]. The surface roughness statistics of the NW was measured

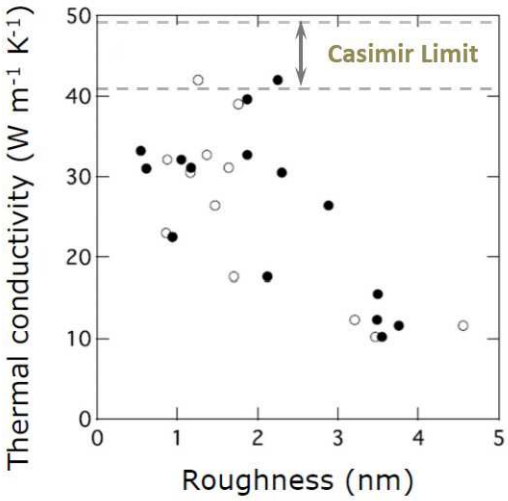

(a)

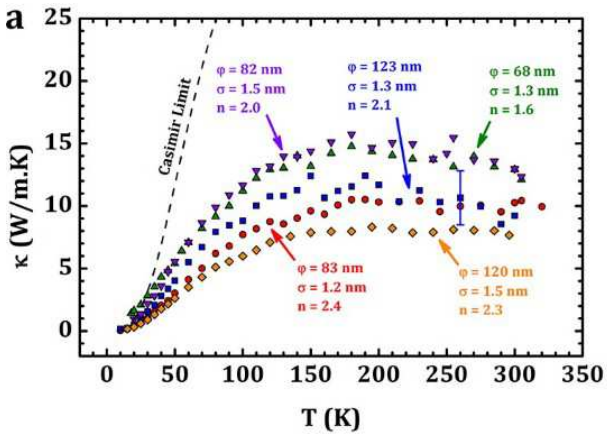

(b)

Figure 5.1: (a) Thermal conductivity of SiNWs measured using time-domain thermoreflectance as the function of RMS roughness height of the nanowires. The Casimir limit of thermal conductivity for the NWs of average diameter 100 nm - 150 nm is also shown. (b) Thermal conductivity of single nanowire with various roughness statistics measured using microfabricated platform.

by HR-TEM as described in Chap. 3 before transferring the wire to the measurement platform. Figure 5.1 (b) shows the thermal conductivity measured for a set of single nanowire with roughness height ~ 1 nm but varying correlation lengths of roughness. In the figure, ϕ, σ and n are roughness correlation length, RMS amplitude of roughness and the exponent of temperature law. The low temperature trend of thermal conductivity data follows $\sim T^{1.6-2.4}$ (in 15 K - 80 K range) as opposed to near T^3 law for frequency-independent boundary scattering. This suggests a strong frequency dependence of the phonon scattering from the roughened walls. We employ the partially coherent transport theory presented in Chap. 2 to study the effect of multiple scattering of phonons from the rough surfaces to study the thermal conductivity trend. We find that the multiple scattering provides an excellent match to the temperature trend law as a function of correlation length of roughness. The details of the data fitting procedure and the analysis of the roughness statistics for this experiment can be found in the Ref. [95].

The studies of enhancement in thermoelectric figure of merit (ZT) in Si have mainly focused on reducing its thermal conductivity by engineering various nanostructures to affect the phonon boundary scattering. The effects of nanostructuring of the electrical properties – electrical resistivity (ρ) and Seebeck coefficient (S) remain largely unexplored. As discussed in Chap. 1, the Seebeck effect arises from the non-equilibrium effects of both the electron and the phonon systems and thus the narrative that nanostructuring will not affect the Seebeck coefficient should be examined carefully. In order to understand the effects of boundary scattering on the phononic component of Seebeck coefficient (S_{ph}) and thermal conductivity (k), we simultaneously measure the thermal conductivity and Seebeck coefficient of the MacEtch nanowires. Using theory as well as the experimental data of S, we aim to understand S_d and S_{ph} individually in SiNWs. The extensive TEM characterization of the nanowire arrays as described in Chap. 3 provides direct correlation of measured transport properties with the NW morphology and roughness. Using the frequency domain techniques described in Chap. 4, we measure S and k of NWAs simultaneously.

The measurement platform and its fabrication is described in Section 5.2. The data reduction and analytical fitting of the data to extract the thermo-

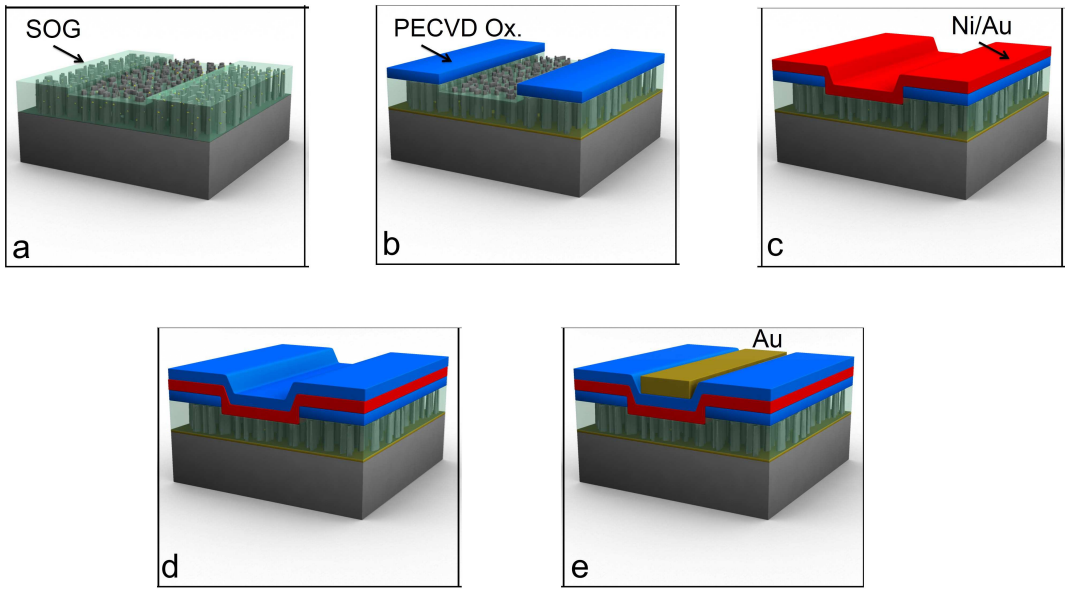

Figure 5.2: Schematic showing the fabrication flow of measurement platform on SOG-filled NW arrays; each step detailed in Sec. 5.2.1

electric properties is discussed in Section 5.3. We then validate the measurement technique by measuring bulk Si properties in Sec. 5.4. We then proceed to the measurements on MacEtch NWAs using this technique in Section 5.5 and analyze the mechanism of Seebeck effect in NWs using the accompanying electrical measurements in Section 5.6.

5.2 Differential measurements of NWAs

5.2.1 Platform fabrication

In this section, we will briefly describe the fabrication of the measurement platform. Figure 5.2 shows the schematic of fabrication flow on preparing the measurement platform on SOG filled nanowires. In order to facilitate electrical contacts to the arrays, a smooth surface is created on the top of array by filling the wire array with spin-on glass (SOG). The SOG is later etched by reactive ion etching using CF_4 gas to make it level with the tips of the nanowires shown in Fig. 5.2 (a). A 300 nm thick PECVD oxide deposited on the SOG-filled arrays is patterned by photolithography to form

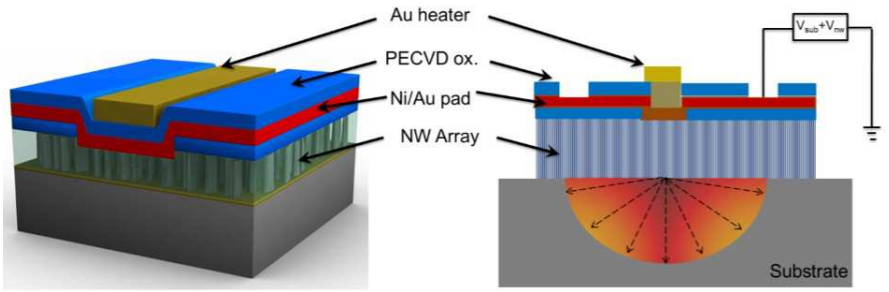

Figure 5.3: Schematic showing the platform for the simultaneous measurement of Seebeck coefficient and thermal conductivity on the spin-on glass filled nanowires

30 μm wide windows shown in Fig. 5.2 (b). The nanowire tips are exposed in these windows by RIE etching of oxide and SOG underneath till ∼100 nm. The electrical contacts which serve as Seebeck voltage pads on the NW arrays are formed by deposition of Ni (150 nm)/ Au (80 nm) for p-type NWs and Ti/Au for n-type nanowires (Fig. 5.2 (c)). The silicide contacts are formed by rapid-thermal annealing the Ni contacts at 320^0C and Ti contacts at 450^0C to achieve ohmic contacts. A thin gold line of width $2b$ ∼30 μm is fabricated right above the voltage pad contacts which serve as the heater element in our design. The Au heater and Seebeck voltage pads are electrically insulated by another 200 nm PECVD oxide /50 nm SiN film shown in Fig. 5.2 (d,e). We found that such a thick oxide was required to avoid electrical cross-talk between the heater and the voltage pads. The devices are finally bonded onto a chip and transferred to a temperature controlled cryostat stage for measurements.

Figure 5.4 shows the frequency responses of the Seebeck voltage and the heater temperature rise respectively in the differential measurement at 300 K and 80 K. As discussed in Chap. 4, the differential method for calculating NW Seebeck coefficient is obtained by extracting signal differentials only across the frequency range where the signals decrease linearly with logarithm of the heating frequency. This is the frequency regime where the thermal penetration ($\Xi = \sqrt{2D_{th}/\omega}$) where D_{th} is the thermal diffusivity) in both the 'ref' and 'NW' samples is within the substrate thickness (t_{Si}=550 μm). At 300 K, this condition applies for the frequency range 200 Hz-4000 Hz for both the 'ref' (30 μm $< \Xi_{ref} <$ 500 μm) and 'NW sample'. However

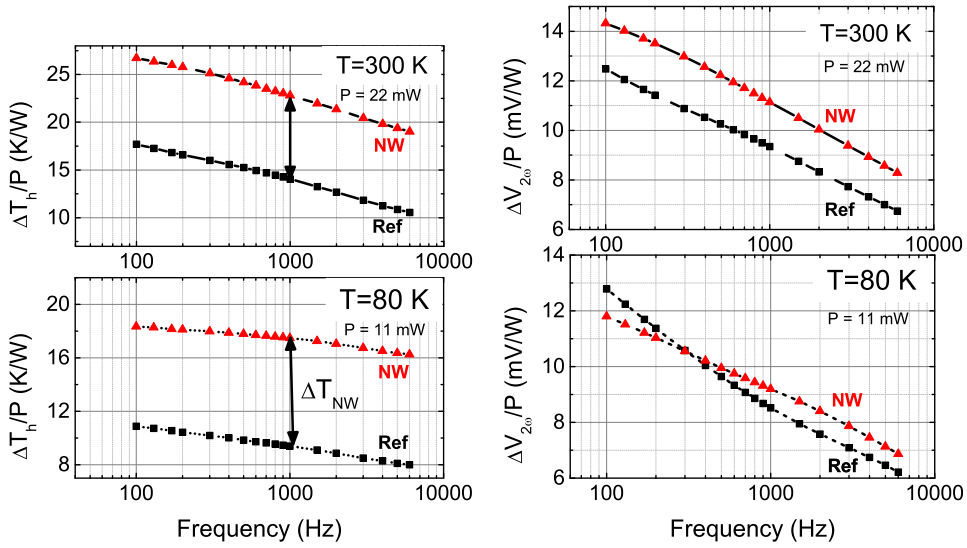

(a) (b)

Figure 5.4: (a) The response of the temperature rise of the heater with heating current frequency at 300 K and 80 K. The sample with nanowire array is labeled 'NW' and the sample on substrate is labeled Ref. The heating power P used at these temperatures is also shown. (b) The response of the measured Seebeck voltage with heating current frequency at 300 K and 80 K.

at low temperatures as shown for 80 K in Fig 5.4, the high thermal diffusivity of Si (40 times larger at 80 K than at 300 K) results in thermal penetration depth in the Ref sample (Ξ_{ref} >550 μm up to f <1000 Hz) exceeding the substrate thickness as well as the length of the heater (L=600 μm in our samples). Thus at 80 K, the differential measurement can only be applied for frequencies beyond 1000 Hz.

5.3 Data reduction and fitting

Figure 5.5 shows the data fitting used to extract Seebeck coefficient and thermal conductivity of bulk Si. For bulk Si, a quick estimate of S can be obtained using slope of Seebeck voltage with frequency (V_{sl}=dV_s/d(ln f)) and slope of heater temperature with frequency (T_{sl}=dT_h/d(ln f)) as $S = -V_{sl}/T_{sl}$. It should be noted that the Seebeck voltage is the out-of-phase signal of '2ω'

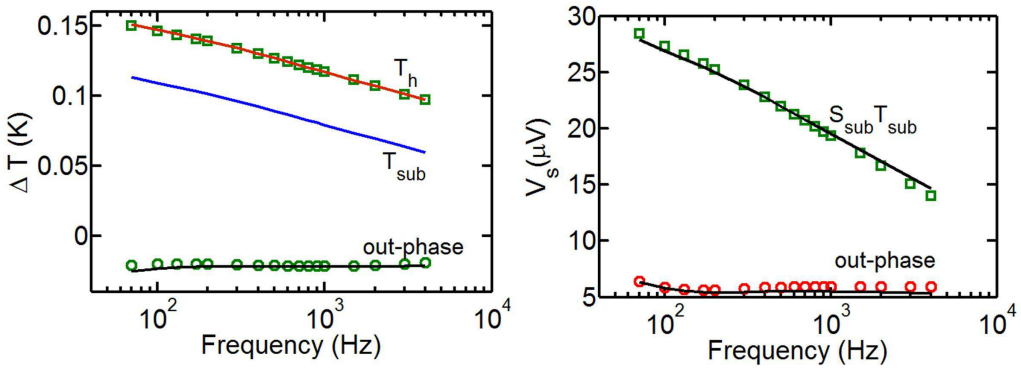

Figure 5.5: The frequency response of heater temperature (T_h) and measured Seebeck voltage (V_s) for bulk Si. The simulated temperature rise at substrate (T_{sub})is used to fit the Seebeck voltage trend.

component in the lock-in amplifier. Similarly, the thermal conductivity is given by $k = -P/(2\pi L T_{sl}$ where P is the heating power. This simple estimates are only valid when the thermal penetration depth is well within substrate thickness over the entire frequency range of fitting. For more accurate estimates, the data fitting should use a model which accounts for finite substrate thickness and finite heater lengths. This model is described in detail in Appendix A. Using this model, we first fit the heater temperature with frequency using k_{sub} and k_{ins} as fitting parameters. The estimation of temperature rise at substrate surface is shown as T_{sub} in Fig. 5.5. If the entire Seebeck voltage measured is contributed by substrate and not by any contacts / interfaces, we require $V_s = S_{sub}T_{sub}$. Using the simulated T_{sub}, we fit the Seebeck voltage data using S_{sub} as the fitting parameter. The exact fit of the magnitude and the phase of V_s across the entire frequency range at 100 K and 300 K proves (a) we are measuring only the open circuit Seebeck voltage (b) no parasitic voltages are measured. Figure 5.6 shows the fitting of measured Seebeck voltage across several temperature validating the model and the fitting procedure.

The sign of Seebeck coefficient depends on the carrier type with S being negative for n-type and positive for p-type. Figure 5.7 shows the raw data of heater temperature rise and measured Seebeck voltage for a n-type and a p-type substrate. We observe that change in polarity of the voltage depending on the carrier type providing an additional confirmation that the measurement only gives the open-circuit Seebeck voltage.

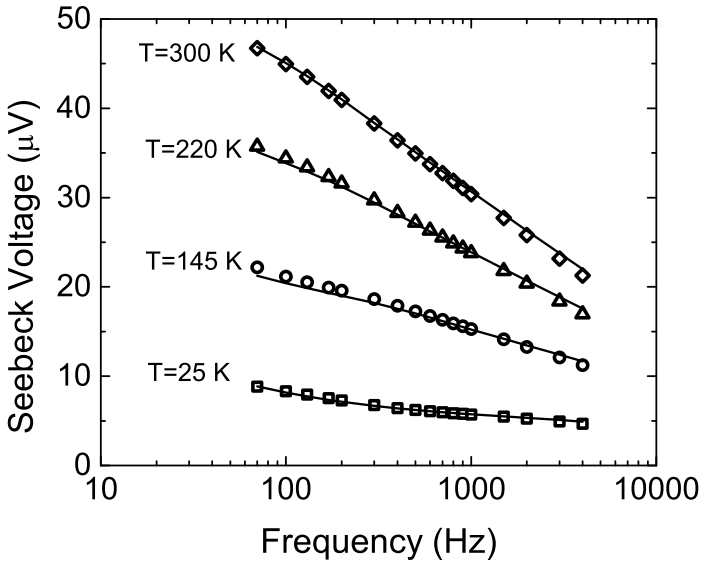

Figure 5.6: The measured Seebeck voltage across several temperatures with heating current frequency. The solid lines represent the fits produced by $V_s = S_{sub}T_{sub}$.

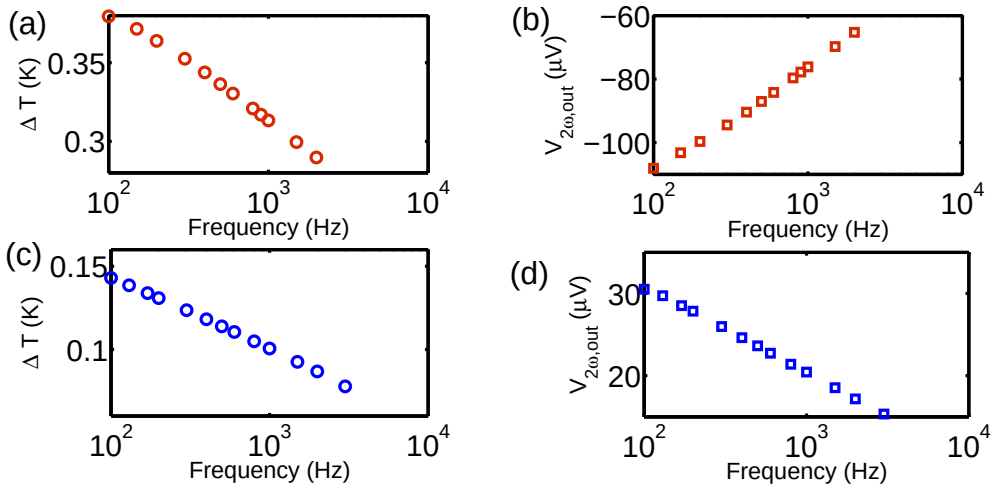

Figure 5.7: The heater temperature rise and the Seebeck voltage for bulk silicon of different carrier types (a) n-type and (b) p-type.

5.3.1 Error analysis of differential measurements

The primary source of error in the measurements arises from the uncertainty in the calibration of temperature coefficient of resistivity (dR/dT). Since the temperature estimation in the measurements are based on resistive thermometry, the calibration error directly affects the temperature drop across nanowire array (ΔT_{NW}), $\Delta\tilde{T}_{NW} = \Delta\tilde{T}_{h,NW} - \Delta\tilde{T}_{h,ref}$ where tilde represents normalized values of temperature $\tilde{T} = T/(P/2bL_h)$, $\Delta\tilde{T}_{h,NW}$ and $\Delta\tilde{T}_{h,ref}$ are heater temperature rise calculated for 'NW' sample and 'ref' sample respectively. The heater temperature rise is inversely proportional to dR/dT. Including the uncertainty in insulating oxide thickness between 'ref' and 'NW' sample, we can estimate the error in calculating the temperature drop across NWs as

$$\begin{aligned}
\delta(\Delta\tilde{T}_{NW}) &= \sqrt{\left(\delta\Delta\tilde{T}_{h,NW}\right)^2 + \left(\delta\Delta\tilde{T}_{h,ref}\right)^2 + \left(\frac{\delta t_{ox}}{k_{ox}}\right)^2} \qquad (5.1)\\
&= \sqrt{\left(\frac{\delta\Delta\tilde{T}_{h,NW}}{\tilde{T}_{h,NW}}.\tilde{T}_{h,NW}\right)^2 + \left(\frac{\delta\Delta\tilde{T}_{h,ref}}{\tilde{T}_{h,ref}}.\tilde{T}_{h,NW}\right)^2 + \left(\frac{\delta t_{ox}}{k_{ox}}\right)^2}\\
&= \sqrt{\left(\frac{\delta\Delta\alpha_{h,NW}}{\alpha_{h,NW}}.\alpha_{h,NW}\right)^2 + \left(\frac{\delta\Delta\alpha_{h,ref}}{\alpha_{h,ref}}.\alpha_{h,NW}\right)^2 + \left(\frac{\delta t_{ox}}{k_{ox}}\right)^2}
\end{aligned}$$

The error in the calibration of the temperature coefficient of resistance is 5% ($d\alpha/\alpha$) [98]. The uncertainty in the oxide thickness between 'NW' and 'ref' samples based on the PECVD system is ∼10 nm. Thus, we obtain ∼12% error in the estimation of $\Delta\tilde{T}_{NW}$ at 300 K and 14% at 80 K. Since the estimation of $\Delta\tilde{T}_{NW}$ is the only source of error in obtaining the Seebeck coefficient of the NW array, the total error estimate for S_{NW} ($=\Delta V_{NW}/\Delta T_{NW}$) is ∼12%. For array thermal conductivity measurements, the main source of error other than uncertainty in $\Delta\tilde{T}_{NW}$ is the uncertainty in estimating the areal coverage of the array x. We conducted extensive SEM areal analysis at several locations in the array and observed ∼20% deviation in areal density of NWs across the array. In addition, we find deviation of nanowire lengths across the array to be within ∼10%. Since the thermal conductivity of the

array is calculated using

$$\begin{aligned} xk_{NW} &= k_{comp} - (1-x)k_{SOG} \\ k_{comp} &= L_{NW}/\Delta\tilde{T}_{NW} \end{aligned} \tag{5.2}$$

we estimate that the overall error in calculating the array thermal conductivity k_{NW} is ∼32% at 300 K.

5.4 S and k measurements on bulk Si

We first measured S in bulk Si samples that act as reference for SiNWs. Fig. 5.8(a) and Fig. 5.8(b) shows the temperature trend of Seebeck coefficient measured for p-type non-degenerate Si (N_a= 2×10^{17} cm^{-3}) and degenerate Si (N_a=3×10^{19} cm^{-3}) respectively. Our data compares well with classical Seebeck data of non-degenerate Si [6, 7] as shown in Fig. 5.8(a). The behavior of the Seebeck coefficient shows distinct physics at these doping levels due to the different dominance of the drag versus the diffusion component. In non-degenerate Si, the phonon drag dominates S at low temperatures. Phonon drag, mainly due to phonons of long wavelengths is the dominant mechanism at low temperatures and low doping levels. With the onset of Umklapp scattering (as indicated by the peak in thermal conductivity in the inset of Fig. 5.8 (a)), the phonons are rapidly thermalized by phonon-phonon scattering. This leads to decrease in the drag in the increasing temperature due to decrease in the transfer of crystal momentum to the electrons. In degenerate Si, phonon drag is further quenched by impurity scattering of phonons. In order to quantitatively estimate the diffusion component versus phonon drag, we theoretically calculate the diffusion component S_d. The calculation of S_d is well documented in the literature and is defined as the average energy transported by the carriers relative to the Fermi level (E_F), and can be calculated directly using a solution to the Boltzmann transport equation as

$$S_d = \frac{1}{eT}\left(\frac{\langle \tau E \rangle}{\langle \tau \rangle} - E_F\right) = \frac{k_b}{e}\left(\frac{(r+2)F_{1+r}(\eta*)}{(r+1)F_r(\eta*)} - \eta*\right) \tag{5.3}$$

where η^* is the reduced Fermi-level ($E_b - E_F/k_bT$) with E_b being the band edge (conduction band in n-type and valence band in p-type), F_n is the Fermi-integral of n^{th} order. The first term is determined by the dominant carrier scattering process while the second term depends the carrier concentration. In order to evaluate Eqn. 5.3, we require the energy dependence of carrier scattering rates which can either calculated in detail using Matheissen's rule (an approach we refer to as Boltzmann solution) or simply assume the power dependence of electron mean-free path with its energy using the exponent r ($\Lambda_{e-e} \propto E^r$ or $\tau \propto E^{r-1/2}$). These methods described in detail in Chap. 6, where we discuss the theory of Seebeck effect. Using the latter approach, we see that the magnitude of S_d increases with the scattering exponent r with r varying between 0 representing the lowest limit for longitudinal acoustic phonon scattering to 2 representing the Conwell-Weisskopf formula for impurity scattering. Subtracting the calculated S_d from the measured S yields the phonon drag S_{ph} shown in Fig. 5.8. We observe the phonon drag has a very significant contribution to S even in highly doped Si at room temperature.

5.5 S and k measurements of rough SiNWs

We now discuss the data for SiNWs. Figure 5.9 shows the temperature trend of S for p-type NW arrays with three different surface morphologies and compares with that of similarly doped bulk Si. The Seebeck coefficient reduces in solid nanowires by $\sim$ 58% at 100 K and by $\sim$27% reduction at 300 K compared to bulk Si. Surface roughness in the range 0.5 nm- 1.3 nm does not appear to have any significant effect on S. We attribute the observed reduction in S to the annihilation of the phonon drag from the boundary scattering of long wavelength phonons. In order to verify this assertion, we calculated S_d at the same doping concentration as measured from SIMS using complete Boltzmann solution and we find a very good fit of the measured data with the calculated trend for S_d. Using Eqn. 5.3, the fit corresponds to r=0.8 indicating that ionic impurity scattering is the dominant electron scattering mechanism in these NWs, as expected. We can ignore any surface charge depletion effects in $\sim$ 100 nm dia. wires doped above $1 \times 10^{19} cm^{-3}$,

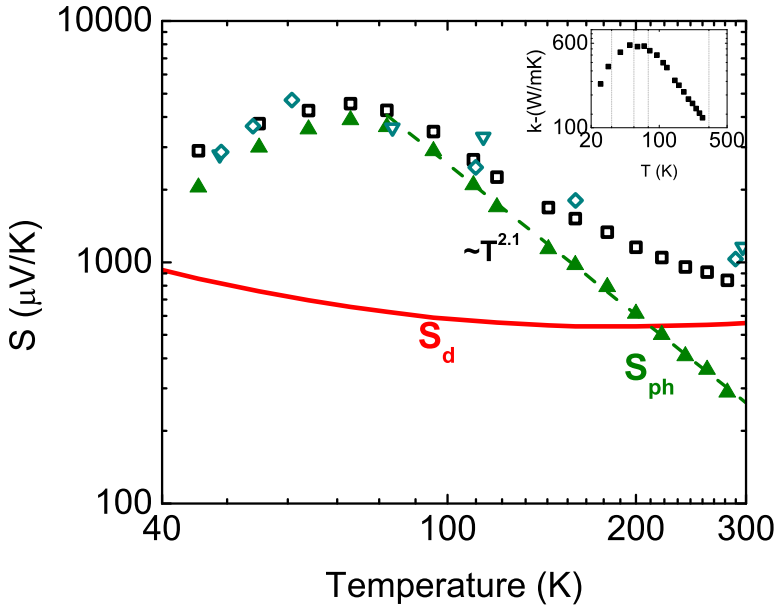

(a)

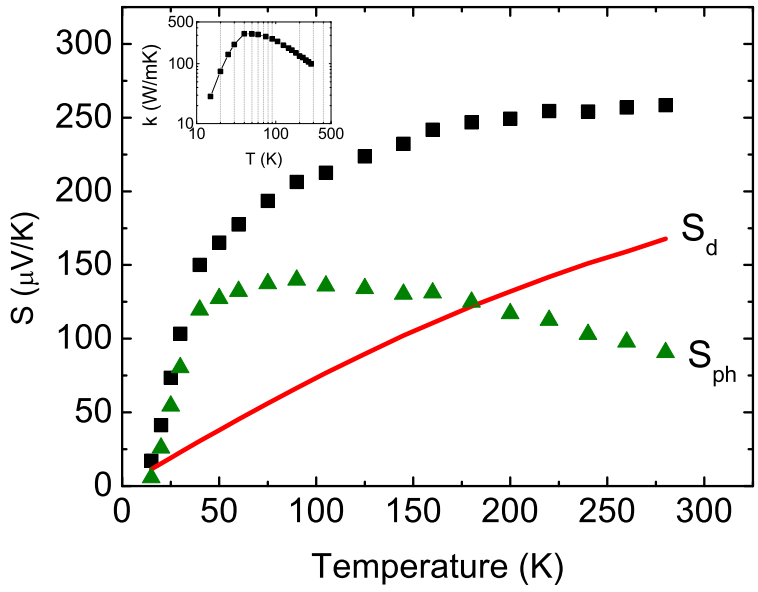

(b)

Figure 5.8: Seebeck coefficient of (a) non-degenerate Si (N_a= 2×10^{17} cm^{-3}) and (b) degenerate Si (N_a= 2×10^{17} cm^{-3}) is shown in solid squares. The diffusion component calculated from Eqn. 5.3 is represented in solid line and the phonon drag extracted is shown in solid triangles. The open symbols in (a) show comparison with classic literature [6, 7]

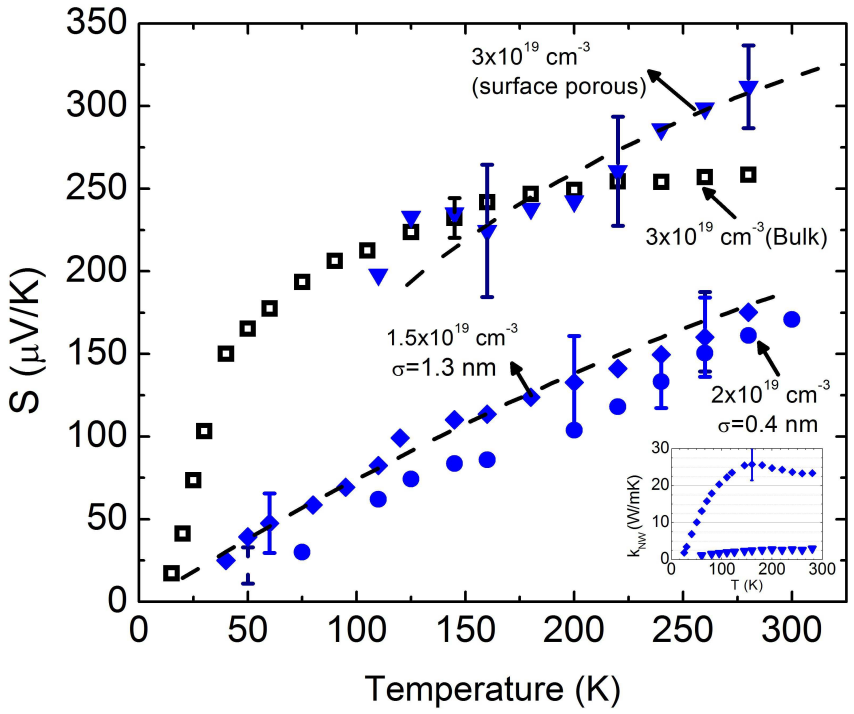

Figure 5.9: The Seebeck coefficient of NW arrays with different surface morphology at similar doping concentrations. The theoretical fits were obtained using Eqn. 5.3 using the doping concentration obtained from SIMS. (Inset shows the thermal conductivity of the NW arrays).

discussed in Sec. 5.6.

Figure 5.9 also shows the trend for S measured on surface-porous nanowires obtained through metal-assisted etching of a degenerate Si wafer (N_a=3×10^{19} cm^{-3}). Interestingly, surface-porous nanowires have similar S as bulk Si at 300 K with the thermal conductivity of the arrays reduced $\sim$20$\times$ below the Casimir limit for these wires. The rising temperature trend of S indicates that phonon drag is absent in these wires, similar to that of the solid nanowires. The enhancement in S_d possibly arises from carrier depletion due to surface porosity or from an increase in the scattering parameter r due to strong scattering from the porous surface. While the depletion of the carriers enhances S_d due to lowering of Fermi level (E_F) (see Eqn. 5.3), the increase in parameter r elevates the average energy of carriers $\langle E \rangle$ and thereby S_d. From fitting S_d to the data using Eqn. 5.3, we find that carrier depletion by half an order of magnitude compared to the original doping would enhance S to the measured value. But this effect cannot explain the steep tempera-

ture trend in the measured S. The slope of S_d versus T is only sensitive to the exponent of the energy dependence in carrier scattering, r. We could fit both the slope and magnitude of S using the original doping concentration of N_a=3×10^{19} cm^{-3} with r=2.2 shown in Fig. 5.9.

5.6 Electrical measurements of SiNWs

One important assumption considered in this work is that the carrier concentration is similar to the dopant concentration measured from secondary ion mass spectroscopy. The validity of this assumption holds when (a) all the acceptor atoms are fully ionized and (b) the surface states do not impact the charge-carrier concentration. In NWs of diameter $\sim$ 20 nm, the ionization energy of the dopants [99] is similar to bulk Si and thus we expect full ionization of the dopants in the NWs investigated in this work. We now discuss the validity of the second assumption, surface depletion effects due to trapped charges at Si/SiO_2 interface. Depending on the charge densities stored at this interface, it has been experimentally observed [99] that NWs can undergo partial to full charge depletion resulting in high resistivity compared to bulk Si. Using the interface trap charge densities $D_{it} = 2 \times 10^{12}$ $eV^{-1}cm^{-2}$ (typical in NWs with native oxide), we calculate the surface depletion layer thickness [99, 8]. Figure 5.10 compares the radius of NWs contributing to charge transport (r_{elec}) to the physical radius of NW (r_{phys}) for various doping levels (with surface depletion thickness being $r_{phys} - r_{elec}$). For NWs of r=50 nm, we see the surface depletion can be ignored in the doping range $3 \times 10^{18} - 7 \times 10^{19}$ cm^{-3}, investigated in this work. Further, since the NWs are surrounded by SOG, there should be better surface passivation of the NW array than assumed.

Electrical measurements on the post-doped MacEtch NWs are an alternate way to SIMS measurements to verify the carrier concentration in the NWs post doping. Since only top-side contacts can be achieved in array scale measurements, only two-point probe measurements are possible. However, due to the current crowding effects at the top-side contacts, the resistance measured in the 2pp measurements is entirely from the contact contribution.

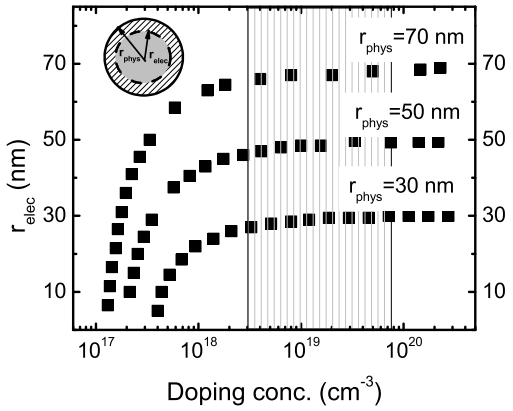

Figure 5.10: Surface depletion model for SiNWs showing the radius of undepleted region (r_{elec}) in comparison to their physical radius (r_{phys}) against dopant concentration. The shaded region indicates the NW doping range studied in this paper. We extracted the data in this figure from Ref. [8].

In order to extract the wire resistivity unambiguously, we conduct four-point probe electrical measurements on a single nanowire separated from the array.

We start with dispersing the nanowires from the array onto an oxidized Si substrate (200 nm thermal oxide). The wires are then located by SEM in order to draw e-beam pattern for the four electrical pads over the NW. Before e-beam lithography to define these pads, the wires are protected by ∼30 nm PECVD oxide film in order to protect the NWs from the organic contaminants. We deposit Ni (130 nm)/Au (30 nm) for electrical pads and the subsequent RTP at 320^0C for 3 min provide ohmic contacts. The measurement platform is shown in Fig. 5.11 (a) and Fig. 5.11 (b) shows the I-V measurements of the NW.

We conduct measurements on long NW arrays (∼15 μm) and short NW arrays (∼2 μm) in order to investigate whether longer MacEtch times used for generating longer NW arrays deteriorate the electrical properties. The results of the resistivity measured for these wires are summarized in Table 5.1. We observe that the electrical resistivity of the MacEtch wires is not length dependent. The NW resistivity is within a factor of 3 from the bulk resistivity values based on SIMS doping concentration. The significant error in these measurements arises from the estimation of the exact cross sectional

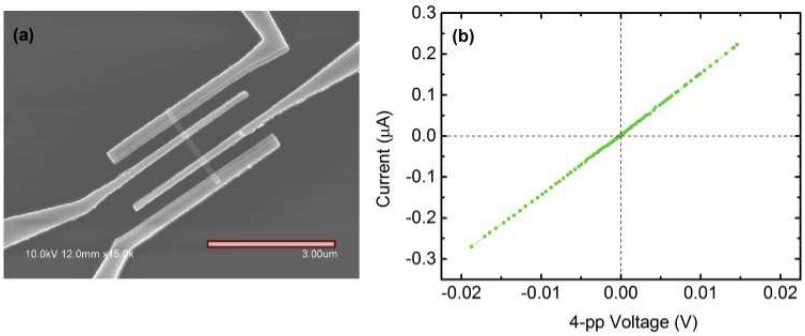

Figure 5.11: (a) SEM micrograph of single NW measurement platform. The scale bar is 3 μm. (b) 4-point probe electrical measurements on single nanowire.

Wire No.	**Est. Doping (cm^{-3})**	**Length**	ρ_{NW} $m\Omega$**-cm**	ρ_{bulk} $m\Omega$**-cm**
W1	7×10^{18}-1×10^{19}	572 nm	11±6	5.5-8.5
W2	1×10^{18}-3×10^{18}	10560 nm	38±7	20–40

Table 5.1: Summary of the single-wire electrical measurements on post-doped nanowires.

area of the NWs. We expect the apparent increase in the resistivity of NWs can be explained by obtaining electrical radius of the wire (the conduction core with active carriers after excluding the surface depleted region) rather than the physical radius obtained from SEM.

We observe a seven-order increase in the resistivity of the surface porous NWs in comparison of bulk Si of similar doping which is expected for mesoporous Si. Since wire resistivity is several orders greater than the contact resistance and the substrate resistance, two-point electrical measurements are sufficient to extract the NW resistivity. We verified this assumption by conducting several 4pp measurements on single NWs and observed that the 2pp and the 4pp resistivity (ρ) were equivalent. Hence we conduct two-point electrical measurements on the same NW array for which the Seebeck coefficient and the thermal conductivity are measured. We note that the temperature dependence of ρ and S, both depend on the energy exponent of scattering r as

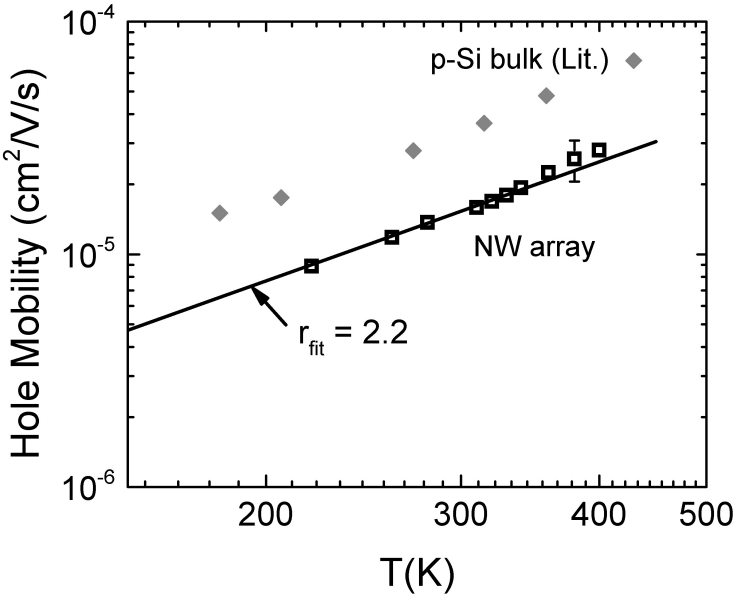

Figure 5.12: Extracted mobility from the two-point resistivity measurements of porous SiNW arrays. The literature values for porous Si mobility are taken from Ref.[9]

$$
\begin{aligned}
S &= \frac{k_b}{e}\left(\frac{(r+2)F_{1+r}(\eta*)}{(r+1)F_r(\eta*)} - \eta*\right) \\
\mu &= A\frac{e}{m_\sigma}(k_bT)^{r-1/2}\frac{F_r(\eta^*)}{F_{1/2}(\eta^*)}(r+1)
\end{aligned}
\tag{5.4}
$$

where the carrier mobility (μ) is related to the resistivity as $\rho = 1/Ne\mu$, N is the free carrier concentration, e is the elctron charge, the electron scattering rate is defined as $\tau_{e-e} = AE^{r-1/2}$ and m_σ is the conductivity effective mass of the carriers. Figure 5.12 shows the extracted mobility of porous NW arrays with temperature. Using the mobility equation in Eqn. 5.4, we use the fitting parameter $r = 2.2$ (from the Seebeck measurement fit in Sec. 5.5 for porous wires) and we see an excellent match to the measured mobility. This suggests that either of these measurements (S or ρ) reveals the dominant carrier scattering mechanism.

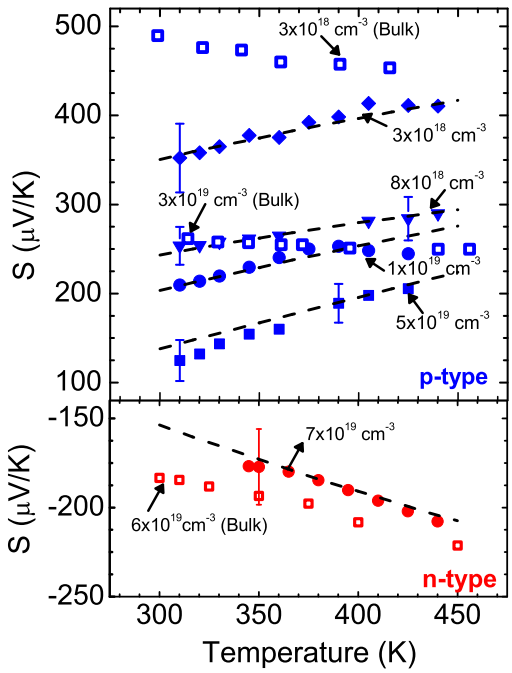

Figure 5.13: The Seebeck coefficient of NW arrays measured across several doping concentrations. The dashed lines represent the diffusion component, S_d calculated theoretically using Eqn. 5.3. The open symbols represent data for bulk Si.

5.7 Discussion

We varied doping in SiNWs to further confirm these observations in the temperature range 300-450 K of interest to thermoelectric waste heat harvesting. Figure 5.13 shows the Seebeck measurements on smooth nanowire arrays doped between 3×10^{18} cm^{-3} -7×10^{19} cm^{-3}. Figure 5.13 also shows the fits to the data using S_d calculated from Eqn. 5.3. We find that best-fit value of r varies between 0.6 at low doping ($N_a = 3 \times 10^{18}$ cm^{-3}) to 0.95 at high doping ($N_a = 3 \times 10^{19}$ cm^{-3}). This increase in r with doping is expected since ionic impurity scattering increasingly dominates longitudinal acoustic phonon scattering at higher doping levels. Consistent with the previous data set, we observe temperature trends that indicate the absence of S_{ph} and the complete dominance of S_d. Again, no surface depletion effects are expected to occur at these degenerate doping levels. The disappearance of S_{ph} in nanowires irrespective of doping concentrations further proves that the quenching is entirely due to boundary scattering of long-wavelength phonons.

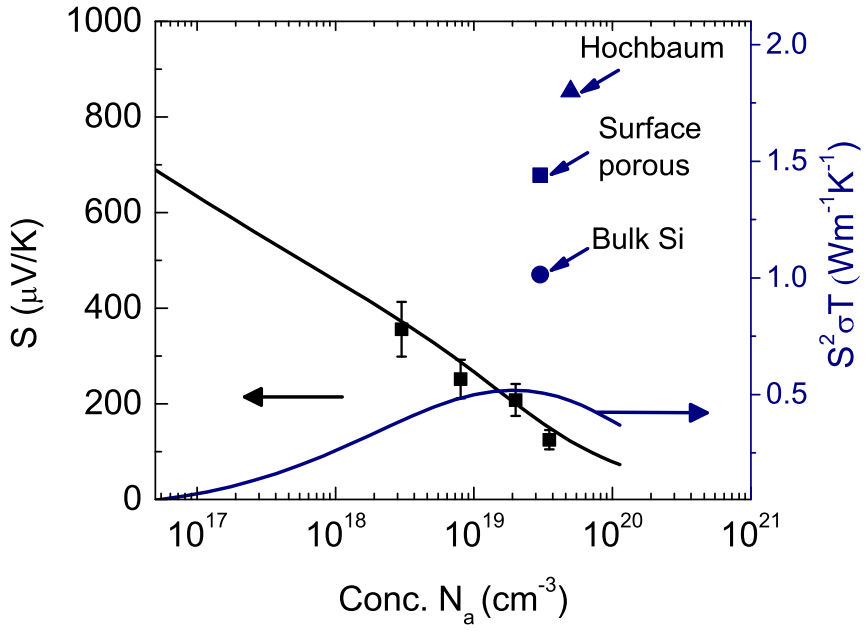

Figure 5.14: The Seebeck coefficient (only the diffusion component S_d and the power factor ($S^2\sigma$T)across various doping levels.

We note that with the absence of S_{ph}, the measurement of S provides an excellent way to obtain carrier concentration using relatively simple fabrication and without requiring any information on the wire diameter or cross-section. In summary, we have experimentally shown the complete annihilation of the phonon drag contribution to the Seebeck coefficient in silicon nanowires across a range of doping concentration, leading to a reduction of as much as 27% at 300 K compared to the bulk. The disappearance of the drag shifts the optimal doping for maximizing the power factor in thermoelectric energy conversion significantly to $\sim 5 \times 10^{19}$ cm^{-3} in p-type nanowires. Figure 5.14 shows that when Seebeck coefficient equals S_d with no contribution from the drag, the power factor peak shifts rightwards. Finally, in porous-surface nanowires, the Seebeck coefficient recovers to the bulk value through enhancement of the diffusion component. Through modeling, we show that this is likely due to strong energy-dependence in carrier scattering. These results motivate a rethinking of the widely pursued approach of enhancing the figure of merit in thermoelectric conversion through introduction of scatterers for phonons of all wavelengths. Scattering phonons lower than the critical frequency contributing to drag reduces the power factor without significantly reducing heat conduction.

CHAPTER 6

THEORY OF THERMOPOWER AND PHONON DRAG

This chapter develops the formal theory of the Seebeck effect using Boltzmann transport equation (BTE). In Section 6.1, we develop theoretical framework to define Seebeck coefficient as a cumulative effect of phonons and electrons in non-equilibrium. We discuss the conditions under which we can decompose the Seebeck coefficient into the diffusion and drag components. We then separately derive the expressions for S_d and S_{ph}. Finally, we investigate the spectral dependence of phonons that contribute to the drag and analyze how boundary scattering affects this dependence.

6.1 Formal theory using Boltzmann transport equation

In this section, we derive the Seebeck coefficient from the solution of Boltzmann transport equation. This derivation gives the expression for generalized S without any distinction between the diffusion component from phonon drag. We consider the simultaneous non-equilibrium amongst the charge carriers and the phonon systems in this model. Consider a one-dimensional conductor (along x-axis) with electric field $\mathbf{F}$ and temperature gradient $\nabla_r T$ across the sample. Due to the presence of electric field, the electron distribution is perturbed to f from its equilibrium distribution f_0. Assuming the electrons relax their momentum through scattering processes including acoustic phonon scattering ($e-ph$) and ionized impurity scattering ($e-ion$), we solve for f using the Boltzmann equation for electron system as

$$-e\vec{F}.\vec{v}\frac{\partial f}{\partial E} \quad + \quad \vec{v}.\nabla_r T\left(\frac{E_F - E}{T}\frac{\partial f}{\partial E}\right) = \left(\frac{\partial f}{\partial t}\right)_{scat}^{e-e} \tag{6.1}$$

$$\left(\frac{\partial f}{\partial t}\right)_{scat}^{e-e} \quad = \quad \left(\frac{\partial f}{\partial t}\right)_{e-ph} + \left(\frac{\partial f}{\partial t}\right)_{e-ion} \tag{6.2}$$

where we use the Fermi-dirac statistics for equilibrium distribution f_0, E_F is the fermi level and E is electron energy relative to band edge. Similarly, the perturbation of phonon distribution N due to temperature gradient can be solved by Boltzmann equation as

$$-\frac{dN}{dT}\frac{dT}{dx}\frac{q_x}{q}u_0 = \left(\frac{\partial N}{\partial t}\right)^{p-p}_{scat} \tag{6.3}$$

$$\left(\frac{\partial N}{\partial t}\right)^{p-p}_{scat} = \left(\frac{\partial N}{\partial t}\right)_{ph-e} + \left(\frac{\partial N}{\partial t}\right)_{ph-b} + \left(\frac{\partial f}{\partial t}\right)_{umk} \tag{6.4}$$

where we consider phonon relaxation processes include phonon-electron, umklapp and boundary scattering. The system of equations in Eqns. 6.1, 6.3 are coupled by the electron-phonon scattering terms expressed as

$$\left(\frac{\partial f}{\partial t}\right)_{e-ph} = A\int_0^{2\pi} d\phi \int_0^{2k} dq\ q^2[(N+1)f(k+q) - Nf(k) \tag{6.5}$$

$$. \quad + \quad Nf(k-q) - (N+1)f(k)]$$

$$\left(\frac{\partial f}{\partial t}\right)_{ph-e} = B\int_0^{2\pi} d\phi \int_{q/2}^{\infty} dk\ k\,[(N+1)f(k+q) - Nf(k)] \tag{6.6}$$

Hence, we need to solve the coupled integro-differential equations Eqns. 6.1, 6.3, 6.5 to obtain the electron and phonon distribution functions. Setting the current density in the specimen to zero for open-circuit Seebeck effect

$$J_x = -e\int v_x(f - f_0)D(E)\ dE = 0 \tag{6.7}$$

where $D(E)$ is electron density of states [100] and using the definition of Seebeck coefficient

$$S = \frac{F_x + d\left(E_F/e\right)/dx}{dT/dx} \tag{6.8}$$

we can derive the Seebeck coefficient. For solving f and N from Eqns. 6.1, 6.3, we need to choose trial function for the distribution functions as

$$f = f_0 + k_F g_e(E) \tag{6.9}$$

$$N = N_0 + q_F g_p(\hbar\omega) \tag{6.10}$$

$$\tag{6.11}$$

where g_e and g_p are unknown functions to be obtained by solving Eqns. 6.1, 6.3, k_F and q_F are the components of electron and phonon wavevectors respectively along the direction of electric field. Solving the distribution functions using coupled Boltzmann equations for electrons and phonons is mathematically cumbersome. Hence, we consider an approximation that the electric field and temperature gradient are small enough to perturb phonon system out of equilibrium. This assumption is valid at low carrier concentrations and appropriate corrections should be applied for highly doped Si.

6.2 Diffusion component of S

The diffusion component of Seebeck coefficient is defined as the average energy transported by electrons relative to Fermi level assuming lattice equilibrium. Hence, we can solve the perturbed electron distribution f from Eqn. 6.1 alone. Using the relaxation time approximation, the scattering term can be written as $(\partial f/\partial t) = (f - f_0)/\tau$. Here, τ is the effective relaxation time of electron scattering obtained by applying Mattheissen's rule for individual scattering processes. From Eqns. 6.1, 6.7, the diffusion component of the Seebeck coefficient assumes the form

$$\begin{aligned} S_d &= \frac{1}{eT}\left[\frac{\int_{E_b}^{\infty} E g(E) v(E) \Lambda(E) \frac{df_0}{dE} dE}{\int_{E_b}^{\infty} g(E) v(E) \Lambda(E) \frac{df_0}{dE} dE} - E_F\right] \\ &= \frac{1}{eT}\left(\langle E \rangle - E_F\right) \end{aligned} \tag{6.12}$$

where $g(E)$ is 3D density of states, $v(E)$ is the carrier velocity, $\Lambda(E)$ is MFP of carriers ($= \tau(E)v(E)$), f_0 is the equilibrium Fermi distribution function and E_F is the Fermi energy [101]. Assuming the energy level E=0 at conduction (or valence) band edge for n-type (or p-type) Si, the Fermi level E_F can be calculated from the carrier concentration (N_a) using the charge neutrality principle[57]. In order to calculate the energy dependence of MFP of carriers $\Lambda(E)$, we adopt two approaches.

- We use the detailed carrier scattering rates with acoustic phonons (Λ_{ADP}), ionic impurities (Λ_{II}), intervalley scattering (Λ_{IV}), boundary

scattering (Λ_{BS}), optical phonon (Λ_{opt}) and plasma scattering (Λ_{PS}). The effective MFP is then calculated using Matthiessens rule. The expressions for the carrier scattering rates of the processes mentioned above can be found in Ref. [29]. In this work, this approach is referred to as Boltzmann solution for S_d calculation.

- Assuming the effective MFP of carriers follows an energy dependence given by $\Lambda \propto E^r$ where r is referred to as the scattering exponent. This simplifying assumption is sufficient to model many electron-scattering mechanism with r=0 for ADP, r=1 for optical phonon scattering and r=2 in the extreme limit of ionic impurity scattering [102]. Increasing the value of r elevates the average energy $\langle E \rangle$ transported by the carriers relative to the Fermi level as seen in Fig 6.1(a). This approach is referred to as scattering exponent method for calculating S_d. This approach is extremely useful to correlate the effect of the dominant mechanism of electron scattering on the magnitude of S_d.

Figure 6.1(b) compares the two approaches for calculating the scattering rate $\tau^{-1}(E)$ (which is $v(E)/\Lambda(E)$) . The figure shows the energy dependence of the individual scattering rates (ionic S_{ii} and acoustic phonon S_{ac}) and the effective scattering rate calculated from the Matthiessens rule in bulk Si doped at 5×10^{19} cm^{-3}. The dotted lines fit the power law dependence r for the scattering processes. Since electron energies only within $\sim 10k_bT$ from Fermi energy contribute to the transport as seen from the density of states plot (shown in Fig. 6.1(a)), the power law dependence r is obtained by fitting the scattering rates in this energy range. We find a good match in the calculated Seebeck coefficient S_d between the two approaches.

6.3 Phonon Drag using Π-approach

In order to calculate the phonon drag, we adopt the Π-approach suggested by Herring (1954)[52]. In this approach, the phonon drag coefficient is defined as the energy flux carried by the phonons ($\mathbf{j}$) for unit carrier flux ($\mathbf{J}$) due to the presence of an electric field $\mathbf{F}$ applied across the specimen. This approach is thermodynamically equivalent to the Seebeck effect wherein an electrostatic

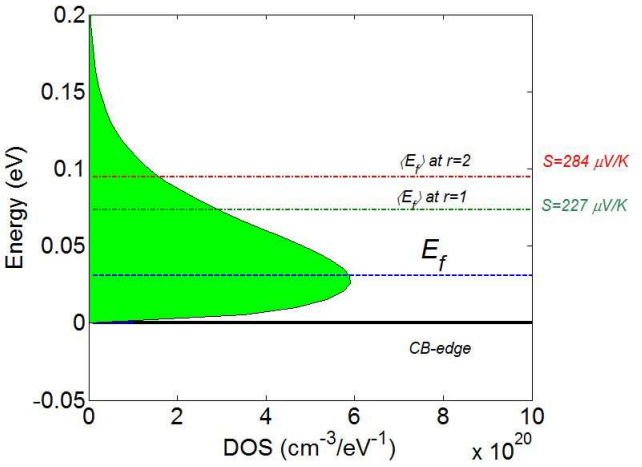

(a)

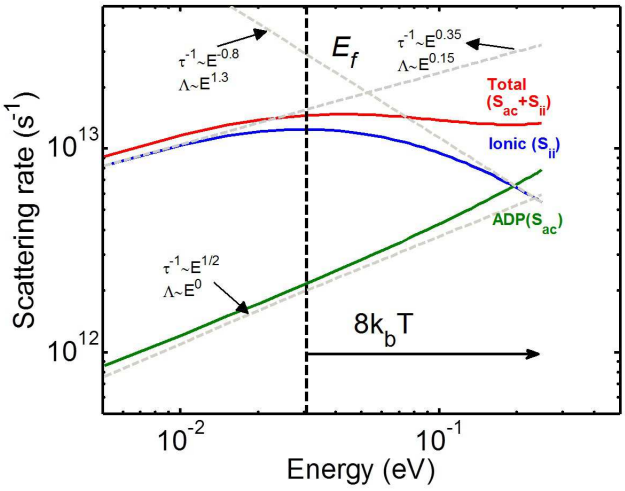

(b)

Figure 6.1: (a) Energy level diagram of n-type Si with carrier concentration $N_d = 5 \times 10^{19}$ cm^{-3}. The effective density of states (represented by filled region) is calculated using $g(E)f(E)$ (b) The exact scattering rates at this doping level (only ADP and II processes are shown here) are fitted for the power law dependence r.

field is set up in the specimen due to temperature gradient across it. In the Π-approach, the scattering of charge carriers by the lattice vibrations tends to increase the amplitudes of lattice waves (phonons) traveling in the direction of electric current ($\mathbf{J}$) resulting in net transport of heat flux ($\mathbf{j}$) in that direction.

In this work, we quantify the energy transport by phonons using crystal momentum which is related to the energy flux as

$$\mathbf{j} = \sum_{\alpha} \mathbf{P}_{\alpha} c_{\alpha}^{2} \tag{6.13}$$

where the crystal momentum ($P_{q,\alpha}$)in the phonon modes of wavevector $\mathbf{q}$ and polarization α with group velocity c_α is given by

$$\mathbf{P}_{\alpha} = \frac{1}{(2\pi)^3} \int N(\mathbf{q}, \alpha) \hbar \mathbf{q} \; d\mathbf{q} \tag{6.14}$$

In the presence of an electric field, crystal momentum is fed into a particular phonon mode ($\mathbf{q}$,α) through electron-phonon processes at rate R($\mathbf{q}$) while the momentum is subsequently relaxed through phonon-phonon processes at rate $\tau_{pp}(\mathbf{q})$. We aim to calculate net crystal momentum change of every phonon mode $\mathbf{P(q)}$ at equilibrium and integrate it over all phonon modes to obtain the heat flux $\mathbf{j}$.

We start by calculating the rate of change of phonon population N($\mathbf{q}$) due to electron-phonon interactions which relates to rate of change of crystal momentum R($\mathbf{q}$) by $R(\mathbf{q}) = \hbar \mathbf{q} \left(\partial N / \partial t\right)$. The expression for phonon population change by emission (first term) and absorption (second term) of phonons due to charge carrier interactions is given by

$$\begin{aligned} \left(\frac{\partial N_q}{\partial t}\right)_{e-ph} = \frac{2\pi}{\hbar} \sum_{\mathbf{q}} \quad & \langle \mathbf{k}, N_q + 1 \left| \mathbf{H} \right| \mathbf{k} + \mathbf{q}, N_q \rangle \delta \left(E_{k,N_q+1} - E_{k+q,N_q} \right) \\ & f_{k+q} \left(1 - f_k\right) - \langle \mathbf{k} + \mathbf{q}, N_q - 1 \left| \mathbf{H} \right| \mathbf{k}, N_q \rangle \\ & \delta \left(E_{k+q,N_q-1} - E_{k,N_q} \right) f_k \left(1 - f_{k+q}\right) \end{aligned} \tag{6.15}$$

In this expression, $\mathbf{k}$ is electron wave-vector and f_k is the perturbed electron distribution function in the presence of electric field F is given by $f = f_0 +$

f_1, where f_0 is the equilibrium Fermi-Dirac distribution and the perturbed distribution f_1 is

$$f_1 = \vec{k}.\vec{F}\frac{\hbar e\tau(E)}{m_\sigma}\frac{f_0(1-f_0)}{k_bT} \tag{6.16}$$

Here, $\tau_{ee}(E)$ is the relaxation time of electron-electron interactions and m_σ is the conductivity effective mass. We simply assume $\tau_{ee}(E)$ is proportional to $E^{r-1/2}$. Using the acoustic deformation potential Hamiltonian [100] **H**, we can calculate the rate of momentum exchange as

$$\begin{aligned} R(q) &= \hbar q\left(\frac{\partial N_q}{\partial t}\right)_{e-ph} \\ &= \frac{\Xi^2 q^2}{(2\pi)^2\rho\omega_q k_b T}\frac{\pi e m_d^2}{m_c\hbar^3}\widehat{q}.\vec{F} \\ &\quad \left[\int_{E=\frac{\hbar^2q^2}{8m}}^{\infty} dE\ (N_q+1)\tau(E)\, f_{E+\hbar\omega_q}(1-f_E) - dE\ N_q\tau(E)\, f_E(1-f_{E+\hbar\omega_q})\right] \end{aligned} \tag{6.17}$$

where Ξ is the deformation potential (9 eV for Si), ρ is the crystal density, ω_q is the mode frequency (we only consider the longitudinal acoustic modes with dispersion $\omega_q = cq$, c=8400 m/s), m_d is the density-of-states effective mass.

In order to calculate R($\mathbf{q}$) using Eqn. 6.17, we consider a approximation that the phonon system is under thermal equilibrium in the presence of the electric field. This allows us to set N_q to the equilibrium Bose Einstein distribution at temperature T. In this study, we are interested in the spectral dependence of phonon drag rather than its magnitude. Hence, the assumption of phonon system in equilibrium is sufficient for our analysis. However, it should be noted that this assumption overestimates drag at high carrier concentrations.

Now, we discuss the spectral dependence of the rate of which phonons receive momentum R($\mathbf{q}$). Figure 6.2 shows the momentum transfer to phonons by carrier scattering in degenerate and non-degenerate Si. For non-degenerate Si, we assume the electron scattering is dominated by longitudinal acoustic

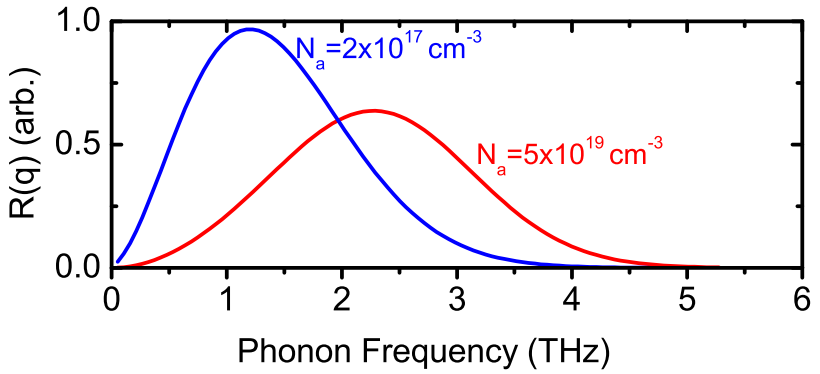

Figure 6.2: Spectral dependence of the rate of momentum exchange R($\mathbf{q}$) by electron-phonon interactions calculated using Eqn. 6.17.

scattering. Hence, we use a carrier concentration $N = 2 \times 10^{17}$ cm^{-3} with scattering exponent r=0 to model non-degenerate Si. Similarly, we assume impurity scattering dominates in degenerate Si and is modeled using carrier concentration $N = 2 \times 10^{17}$ cm^{-3} and r=2. From Fig. 6.2, we observe that the only the phonon modes within a critical frequency (ω_c) receive momentum from electron-phonon interaction. This critical frequency extends with increase in carrier concentration from $\sim$ 3 THz in non-degenerate Si to $\sim$ 4 THz in degenerate Si.

We now consider the relaxation of the phonons by phonon-phonon processes with relaxation time $\tau_{pp}(q)$. In bulk Si, we only consider Umklapp scattering and mass difference scattering with the effective $\tau_{pp}(q)$ calculated using Mattheissens rule. Hence, the rate at which the crystal momentum relaxes by phonon-phonon processes is given by $(N - N_0)/\tau_{pp}(q)$. At equilibrium, the net change in crystal momentum of a mode is

$$\mathbf{p(q)} - \mathbf{p_{eq}(q)} = \tau(\mathbf{q})\mathbf{R(q)} \tag{6.18}$$

where $p_{eq} = \hbar \mathbf{q} N_{eq}$ is the phonon momentum at equilibrium with N_{eq}, the Bose-Einstein distribution at T. Integrating Eqn. 6.18 over the Brillouin zone, we obtain the total crystal momentum as

$$\Delta \mathbf{P}_0 = \frac{1}{(2\pi)^3} \int \tau(\mathbf{q}) R(\mathbf{q}) \; d\mathbf{q} \tag{6.19}$$

since the equilibrium term p_{eq} vanishes in the integration.

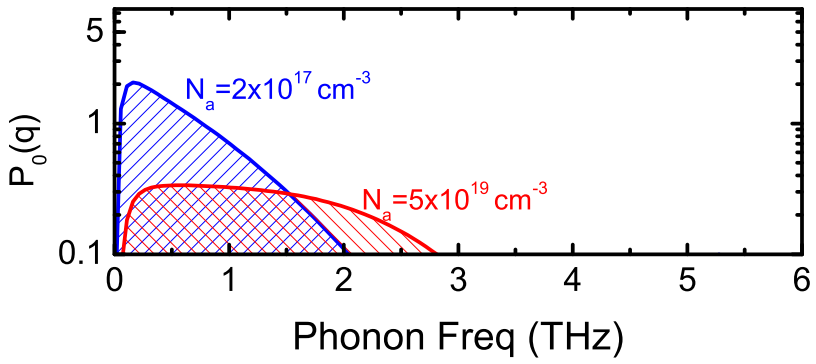

Figure 6.3: Spectral dependence of the net crystal momentum change in bulk Si for degenerate and non-degenerately doped Si calculated using Eqn. 6.18.

Figure 6.3 shows the spectral dependence of crystal momentum change due to balance of electron-phonon and phonon-phonon processes. We use Eqn. 6.18 to calculate the change in crystal momentum. We observe that $\sim$ 90% of crystal momentum and thus phonon drag is contributed by phonon frequencies $\leq$ 1.2 THz in non-degenerate Si. In degenerate Si, the magnitude of crystal momentum change is comparatively lower than non degenerate Si with the frequencies $\leq$ 2.3 THz contribute to phonon drag.

6.4 Effect of boundary scattering on drag

This section consider the phonon drag in low-dimensional materials where boundary scattering and phonon-phonon scattering are of comparable importance. We specifically aim to understand how the crystal momentum in a volume element $\hbar\mathbf{q}$ of $\mathbf{q}$ space is distributed spatially over the cross section of the specimen. In the presence of a electric field $\mathbf{F}$, the rate at which crystal momentum is fed into the volume element $\hbar\mathbf{q}$ through electron-phonon interactions is independent of position and proportional to R($\mathbf{q}$) in Eqn. 6.17. Phonon-phonon scattering removes crystal momentum from the volume element $\hbar\mathbf{q}$ at a rate proportional to the local density $\Delta P(\mathbf{q};\mathbf{r})$ of crystal momentum. Boundary scattering also removes crystal momentum but only from regions adjoining the boundaries proportional to the local crystal mo-

mentum at the boundary and to the component of phonon velocity toward the boundary.

Thus, we can investigate the spatial dependence of the crystal momentum in presence of crystal boundary scattering by solving the Boltzmann transport equation in a cylindrical wire (along the z-axis)

$$v_x \frac{\partial \Delta \mathbf{P}}{\partial x} + v_y \frac{\partial \Delta \mathbf{P}}{\partial y} + \frac{\Delta \mathbf{P}}{\tau(\mathbf{q})} = \frac{1}{(2\pi)^3} R(\mathbf{q}) \tag{6.20}$$

where ΔP is phonon momentum change in presence of boundary scattering. We assume the boundaries are diffuse so that $\Delta \mathbf{P}$ at the boundaries vanishes. We note that the wires measured do not have a circular cross section, but our approximation should yield reasonable insight. The solution for the above equation in a wire of radius a with diffuse boundaries was obtained by Dingle (1948)[103] as

$$\Delta P\left(r;q\right) = \frac{\tau\left(q\right) R\left(q\right) d^3q}{\left(2\pi\right)^3} \left[1 - exp\left(-\frac{rsin\phi + (a^2 - r^2cos^2\phi)}{\tau\left(q\right) vsin\theta}\right)\right] \tag{6.21}$$

where (r,θ, ϕ) define the spherical coordinate system for wavevector $\mathbf{q}$. The phonon-phonon relaxation $\tau(q)$ considers Umklapp and mass-difference scattering. Figure 6.4 plots the radial distribution of crystal momentum in wires of radii 10μm, 1μm and 100 nm calculated from Eqn. 6.21. The magnitude in colorbar in Fig. 6.4 compares the crystal momentum in presence of boundary scattering $\Delta P(r)$ relative to the crystal momentum in bulk Si $\Delta P_0(r)$ (this quantity is set to 1 for all the three cases). We observe that the crystal momentum is quenched by boundary scattering for wires of radii $< 1\mu$m and vanishes by an order in 100 nm wires.

Finally, we can obtain phonon drag by calculating the total crystal momentum $\langle P \rangle$ by integrating Eqn. 6.21 over space and over all phonon modes. We define γ as the ratio of total crystal momentum in presence of boundary scattering $\langle P \rangle$ to that in the absence of boundary scattering $\langle P_0 \rangle$ as

$$\gamma = \frac{\int_{q=0}^{\infty} \int_{r=0}^{a} \int_{\theta=0}^{\pi} \int_{\phi=0}^{2\pi} \Delta P\left(r;q\right) 2\pi r dr q^2 \; dq \; sin\theta d\theta d\phi}{\int_{q=0}^{\infty} \int_{r=0}^{a} \int_{\theta=0}^{\pi} \int_{\phi=0}^{2\pi} \Delta P_0\left(q\right) 2\pi r dr q^2 \; dq \; sin\theta d\theta d\phi} \tag{6.22}$$

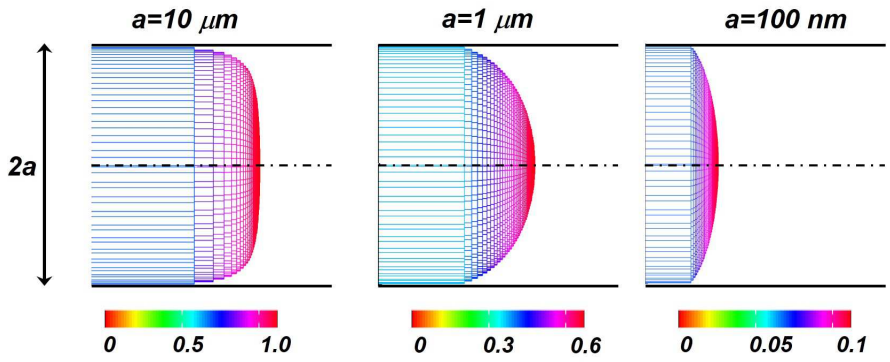

Figure 6.4: The radial distribution of crystal momentum in wires of radii 10μm, 1μm and 100 nm calculated using Eqn. 6.21. The color bar shows the magnitude of crystal momentum relative to crystal momentum P_0 in absence of boundaries.

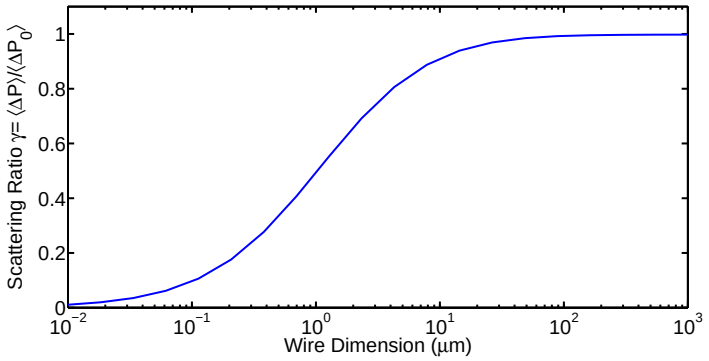

Figure 6.5: The effect of boundary scattering on the transfer of total crystal momentum $\langle P \rangle$ in comparison to that in the absence of boundaries $\langle P_0 \rangle$ with varying wire radius.

Figure 6.5 shows the effect of boundary scattering on total crystal momentum quantified by γ with wire radius. We observe that the boundary scattering effectively quenches phonon drag at a wire radius of 100 nm, consistent with the experimental observation.

CHAPTER 7

CONCLUSIONS AND FUTURE WORK

This dissertation explores the thermoelectric properties of the electrolessly etched silicon nanowires with a specific focus on the effects of phonon scattering on nanowire thermal conductivity and the Seebeck coefficient. Using novel frequency domain techniques, we conducted simultaneous measurements of the Seebeck coefficient and the thermal conductivity of the nanowire arrays. In conjunction with the charge and thermal transport theories, we interpret the measured data to gain insights into the transport physics in the nanowires. In this chapter, we summarize the key conclusions of our research and present future directions of research for designing highly efficient silicon based thermoelectrics.

Thermal conductivity data for rough surface silicon nanowires suggest the breakdown of the Casimir limit which assumes completely diffuse phonon boundary scattering. We show that the coherent effects in phonon transport at room temperature indeed can lead to such breakdown. Correlated multiple scattering of phonons off the rough surface lead to a reduced thermal conductivity that is dependent not just on the roughness amplitude but more importantly on the roughness correlation length. A correlation length less than diameter of wire is typically necessary for lowering the thermal conductivity below the Casimir limit. We find non-propagating diffusive phonon modes to be the prime conductors of heat in surface disordered nanowires, consistent with molecular dynamics calculations [39] on atomistic scale nanowires. There is no indication of localization in our calculations at the roughness scales reported thus far. We do not observe any length dependence in thermal conductivity, consistent with experimental reports [4, 34]. We note that the model is not without assumptions and the Bourret approximation used in the model might overestimate the phonon scattering rate. However, removing the assumptions remains challenging at present and will be a focus

of future work. The quantitative comparisons with the existing experimental data lend credence to the existence of coherent effects in phonon surface scattering close to room temperature.

To experimentally investigate the effects of phonon scattering in rough nanowires on the thermoelectric properties, we fabricated silicon nanowire arrays by metal-assisted chemical etching. Using extensive characterization of the nanowires by transmission electron microscopy and secondary ion mass spectroscopy, we developed a process to produce nanowire arrays of controllable surface roughness, doping, crystallinity and wire morphologies. The process can generate surface roughness in the range 0.3 - 4 nm RMS height and doping concentration in the range 4×10^{18} cm^{-3} to 7×10^{19} cm^{-3}. The study of porosity of the nanowires produced by etching the degenerately doped silicon wafers using various etching chemistries further advanced the understanding of the kinetics of the electrochemical etching process.

We simultaneously measured the thermal conductivity and the Seebeck coefficient of the nanowire arrays using novel frequency domain methods. In contrast to standard DC techniques, the parasitic contributions in the measurements can be isolated unambiguously due to their distinct frequency response in comparison with the nanowire arrays. Thus, the measurement technique provides an improvement over existing closed circuit techniques for cross-plane thermoelectric measurements. We also discuss the limits on the validity of the frequency domain techniques using detailed simulations of heat diffusion in the measurement platform.

The measurements on the nanowire arrays show that the thermal conductivity reduces with the amplitude of surface roughness to five times below the Casimir limit at 4 nm RMS roughness height. The highest reduction in thermal conductivity of 2 W/mK at room temperature was observed in the mesoporous nanowires etched from a highly doped substrates. We also observed a significant reduction in the Seebeck coefficient of the nanowires compared to the bulk by $\sim$27% at doping concentration 2×10^{19} cm^{-3}. Using the temperature dependent measurements and theoretical calculations, we concluded that the annihilation of phonon drag in these wires leads to the reduction in the Seebeck coefficient. Our measurements on bulk silicon show

that phonon drag has significant contribution to the Seebeck coefficient even in highly doped silicon (close to $k_b/e \sim 87$ μV/K at degenerate doping), an effect which is largely ignored in silicon thermoelectrics.

We have experimentally shown that phonon drag vanishes in silicon nanowires across a range of doping concentration. In the absence of drag, the data agree remarkably well with the theoretical S_d. The magnitude of the reduction is independent of any nanometer scale surface roughness, confirming that primarily long wavelength phonons contribute to drag. In mesoporous nanowires, S recovers to the bulk value through enhancement of the diffusion component due to strong energy-dependence in the carrier scattering mechanism. While this work investigated silicon nanowires, we expect the results to apply in general to other nanostructures and nanostructured bulk materials wherever drag is consequential in the bulk.

In order to understand the spectral contributions of phonons to drag in silicon, we developed a crystal momentum balance theory based on Herring's approach. In this approach, phonon drag is obtained by equating the rate of crystal momentum transfer from the electron-phonon processes to the rate at which it is removed by the phonon-lattice scattering processes. In bulk silicon, we observe that over 90% of phonon drag is contributed by phonon frequencies$<$ 1.2 THz. The crystal momentum is further quenched by boundary scattering of phonons in nanowires of diameter $<$ 10 μm. We observe that the boundary scattering effectively quenches phonon drag at a wire radius of 100 nm, consistent with the experimental observation.

We also comment on a subtle point on whether the decomposition of Seebeck coefficient into diffusion and drag is always valid. In the derivation of the Seebeck coefficient using the coupled Boltzmann transport equation of the electron and the phonon systems, we observe that effect of lattice non-equilibrium is inseparable from the diffusion of charge carriers. The decomposition possible only when the mean free path of phonons that participate in electron-phonon interactions is several times higher than the mean free path due to phonon-phonon processes. This decomposition into drag and diffusion components is thus more appropriate in nanowires than in bulk silicon. For accurate quantitative prediction of phonon drag, a fully symmetric

treatment of non-equilibrium amongst electrons and phonons is necessary but in such rigorous theory, a unique distinction between the diffusion (S_d) and drag (S_{ph}) components does not exist.

In light of the data presented here, the general approach of introducing scattering mechanisms to reduce phonon transport indiscriminately across all frequencies is unlikely to be beneficial for thermoelectrics. In materials such as Si, Ge and SiGe in particular, only phonons above the critical frequency can be scattered to conserve S even while reducing thermal transport. Point scatterers may be more beneficial in this regard [104]. Beyond thermoelectrics, reduced phonon drag in nanostructures should also alter thermomagnetic phenomena [105, 106] such as the Nernst and Ettingshausen effects.

APPENDIX A

HEAT DIFFUSION SOLUTION AT INTERFACES

In this section, we present the complete solution of the periodic steady-state heat diffusion equation in a multi-layered system. We wish to solve for the temperature field at each interface. In addition, we include the finiteness of heater. This generic solution can also be applied to 3ω experiments where the length of the heater is comparable to the heat penetration depth.

Figure A.1 shows the schematic of the n-layered system with the supporting substrate considered as $\mathbf{n}^{th}$ layer. The thermophysical properties of $\mathbf{i}^{th}$ layer of thickness (W_i) are represented by thermal conductivity (k_i) and thermal diffusivity (α_i). The temperature field in the $\mathbf{i}^{th}$ can be solved using heat diffusion equation given by

$$\frac{\partial^2 T}{\partial x^2} + \frac{\partial^2 T}{\partial y^2} + \frac{\partial^2 T}{\partial z^2} + \frac{1}{\alpha_i}\frac{\partial T}{\partial t} = -\frac{1}{\kappa_i} Q_i(x,y,z) \quad in\ \mathbf{i^{th}}\ \mathbf{layer} \tag{A.1}$$

$$\kappa_i \frac{\partial T}{\partial n_i} = \tilde{q}_i \quad \text{at the } i^{th} \text{ interface} \tag{A.2}$$

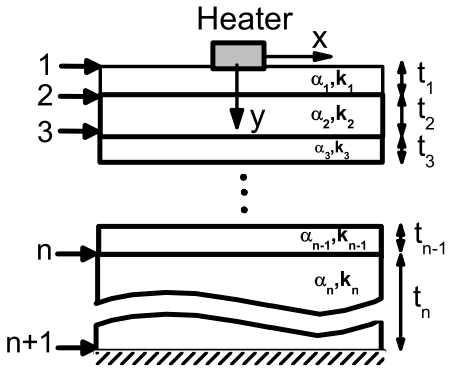

Figure A.1: Schematic of n-layered medium for frequency domain measurements. The origin of the coordinate system is located at the heater.

where Q_i is volumetric heat generation in the heater , n_i represents outward normal at i^{th} interface (interface between $(\mathbf{i}-\mathbf{1})^{th}$ layer and $\mathbf{i}^{th}$ layer) and $\tilde{q_i}$ represents the heat flux at this interface. In this model, the bottom of the substrate $(n+1)^th$ interface is considered adiabatic such that $q_{n+1}=0$.

We adopt Green's function approach to solve the system of equations in Eqn A.1. Let $G_i(y,\mathbf{r};y',\mathbf{r'})$ represent the periodic-steady state Green's function for the $\mathbf{i^{th}}$ layer with the point source at (y',**r'**). Then, we can express the temperature field of an $\mathbf{i}^{th}$ layer in terms of the Green function as

$$T(x,y,z,\omega)=-\frac{\alpha_i}{k_i}\int\int_{s_i}G(y,r;y_i,0)q_i ds_i+\frac{\alpha_i}{k_i}\int\int_{s_{i+1}}G(y,r;y_{i+1},0)q_{i+1}ds_{i+1} \tag{A.3}$$

with the temperature distribution in the first layer given by

$$T(x,y,z,\omega)=\frac{\alpha_1}{k_1}\int\int\int_{V_1}G_1(r,r')Q(r')\ dV+\frac{\alpha_1}{k_1}\int\int_{s_2}G(y,r;W_1,0)q_2 ds_2 \tag{A.4}$$

wheres_i represents i^{th} interface.It is convenient to express the above quantities in spatial Fourier transform defined by

$$\tilde{T}(\beta)=\int_{-\infty}^{\infty}\mathbf{T}(\mathbf{r},\mathbf{y})\mathbf{e}^{-\mathbf{j}\beta.\mathbf{r}}\ \mathbf{dr} \tag{A.5}$$

where the wavevector $\beta=k_x\hat{e}_x+k_z\hat{e}_z$ and $\mathbf{r}=x\hat{e}_x+z\hat{e}_z$.

The three-dimensional Greens function G for periodic steady-state heat diffusion in a thin film of finite width (W_i) with the uniform heat flux condition at its interfaces is given by [107]

$$\begin{aligned}&\tilde{G}(y,r;y',r'=0)=P(y;y',\omega)e^{-j\beta.\mathbf{r}}\\&P(y;y',\omega)=\frac{e^{-\sigma_i(2W_i-|y-y'|)}+e^{-\sigma_i(2W_i-y-y')}+e^{-\sigma_i|y-y'|}+e^{-\sigma_i(y+y')}}{2\alpha_i\sigma_i(1-e^{-2\sigma_i W_i})}\end{aligned} \tag{A.6}$$

where σ_i=$\sqrt{\beta^2+2j\omega/\alpha}$. In this equation, we use a local coordinate system for each layer y_i with the top surface of the layer at $y_i=0$

In this work, we assume the perfect thermal interfaces without any thermal boundary resistances. This assumptions allows us to apply heat flux and temperature continuity at the interfaces $T_i(y_i=W_i)=T_{i+1}(y_{i+1}=0)$. Now using the relations in Eqn A.3A.6 and expressing the quantities in Fourier

domain, we arrive at an iterative solution for interface thermal fluxes given by

$$\tilde{q}_i = \frac{\tilde{q}_{i+1}\psi_i + \tilde{q}_{i-1}\psi_{i-1}}{\chi_i + \chi_{i+1}} \tag{A.7}$$

and

$$\tilde{q}_2 = \frac{\tilde{q}_3\psi_3 - \tilde{Q}\psi_1}{\chi_1 + \chi_2} \tag{A.8}$$

where $\chi_i = 1/k_i\sigma_i \, tanh(\sigma_i W_i)$ and $\psi_i = (1/k_i\sigma_i) \, csch(\sigma_i W_i)$. We can solve for interface thermal fluxes using the system of linear equations in Eqns A.7A.8 and for an unit heat source $\tilde{Q} = 1$. Finally, the temperature field at the i^{th} interface $\tilde{T}_i$ can now be expressed in terms of thermal fluxes as

$$\tilde{T}_i = \tilde{q}_{i+1}\psi_i - \tilde{q}_i\chi_i \tag{A.9}$$

and

$$\tilde{T}_2 = \tilde{Q}\psi_1 + \tilde{q}_2\chi_1 \tag{A.10}$$

A.1 Line Heater assumption

For a rectangular line heater on the multi-layered system, the volumetric heat generation term is given by $\tilde{Q} = P/L \; sin(k_x b)/k_x b$ where L is length of the heater, $2b$ is the width of the heater and P is the heat generation. Thus, we have to substitute the above source term in Eqns. A.7A.8A.9A.10 to obtain the heat flux and temperature fields for this system. In this case, it is sufficient to use the 2D Green function in Eqn A.6 and the inverse fourier transform quantities are expressed as

$$T(x,y) = \frac{1}{2\pi}\int_{k_x=-\infty}^{\infty} \frac{P}{L}\frac{sin(k_x b)}{k_x b}\tilde{T}(k_x, y) \; dk_x \tag{A.11}$$

and the heater temperature response (T_h relevant the 3ω measurements) at the top interface (T_1) is averaged across the width of heater $|x| < b$

$$\langle T_h \rangle = \frac{P}{\pi L}\int_{k_x=0}^{\infty} \frac{sin^2(k_x b)}{(k_x b)^2}\tilde{T}_1(k_x) \; dk_x \tag{A.12}$$

When the heat penetration depth or the substrate thickness is comparable to the length of the heater, we cannot use the rectangular line heater assump-

tion. In this case, the finiteness of the heater should be taken into account by solving the complete 3D heat diffusion equations and the Eqns A.11A.12 transform into

$$\begin{aligned} T(x,y,z) &= \frac{P}{4\pi^2}\int_{k_x=-\infty}^{\infty}\int_{k_z=-\infty}^{\infty}\frac{sin(k_x b)}{k_x b}\frac{sin(k_x L/2)}{k_z L/2}\tilde{T}(\beta,y)\ dk_x\ dk_z \\ \langle T_h\rangle &= \frac{P}{\pi^2}\int_{k_x=0}^{\infty}\int_{k_z=0}^{\infty}\frac{sin^2(k_x b)}{(k_x b)^2}\frac{sin^2(k_z L/2)}{(k_z L/2)^2}\tilde{T}_1(\beta)\ dk_x\ dk_z \quad \text{(A.13)} \end{aligned}$$

REFERENCES

[1] J. P. Heremans, M. S. Dresselhaus, L. E. Bell, and D. T. Morelli, "When thermoelectrics reached the nanoscale," *Nature nanotechnology*, 2013.

[2] N. Mingo, "Calculation of si nanowire thermal conductivity using complete phonon dispersion relations," *Phys. Rev. B*, vol. 68, p. 113308, Sep 2003. [Online]. Available: http://link.aps.org/doi/10.1103/PhysRevB.68.113308

[3] A. I. Hochbaum, R. Chen, R. D. Delgado, W. Liang, E. C. Garnett, M. Najarian, A. Majumdar, and P. Yang, "Enhanced thermoelectric performance of rough silicon nanowires," *Nature*, vol. 451, no. 7175, pp. 163–167, 2008.

[4] K. Hippalgaonkar, B. Huang, R. Chen, K. Sawyer, P. Ercius, and A. Majumdar, "Fabrication of microdevices with integrated nanowires for investigating low-dimensional phonon transport," *Nano letters*, vol. 10, no. 11, pp. 4341–4348, 2010.

[5] R. Chen, A. I. Hochbaum, P. Murphy, J. Moore, P. Yang, and A. Majumdar, "Thermal conductance of thin silicon nanowires," *Physical review letters*, vol. 101, no. 10, p. 105501, 2008.

[6] T. Geballe and G. Hull, "Seebeck effect in silicon," *Physical Review*, vol. 98, no. 4, p. 940, 1955.

[7] M. Brinson and W. Dunstant, "Thermal conductivity and thermoelectric power of heavily doped n-type silicon," *Journal of Physics C: Solid State Physics*, vol. 3, no. 3, p. 483, 1970.

[8] H. Schmid, M. T. Bjork, J. Knoch, S. Karg, H. Riel, and W. Riess, "Doping limits of grown in situ doped silicon nanowires using phosphine," *Nano Letters*, vol. 9, no. 1, pp. 173–177, 2008.

[9] P. Rao, E. A. Schiff, L. Tsybeskov, and P. Fauchet, "Photocarrier drift-mobility measurements and electron localization in nanoporous silicon," *Chemical physics*, vol. 284, no. 1, pp. 129–138, 2002.

[10] A. F. Ioffe, *Semiconductor Thermoelements and Thermoelectric Cooling.* Infosearch, London, 1957.

[11] L. Hicks and M. Dresselhaus, "Effect of quantum-well structures on the thermoelectric figure of merit," *Physical Review B*, vol. 47, no. 19, p. 12727, 1993.

[12] L. D. Hicks and M. S. Dresselhaus, "Thermoelectric figure of merit of a one-dimensional conductor," *Phys. Rev. B*, vol. 47, pp. 16 631–16 634, Jun 1993. [Online]. Available: http://link.aps.org/doi/10.1103/PhysRevB.47.16631

[13] R. Venkatasubramanian, E. Siivola, T. Colpitts, and B. O'quinn, "Thin-film thermoelectric devices with high room-temperature figures of merit," *Nature*, vol. 413, no. 6856, pp. 597–602, 2001.

[14] T. Harman, P. Taylor, M. Walsh, and B. LaForge, "Quantum dot superlattice thermoelectric materials and devices," *Science*, vol. 297, no. 5590, pp. 2229–2232, 2002.

[15] K. F. Hsu, S. Loo, F. Guo, W. Chen, J. S. Dyck, C. Uher, T. Hogan, E. Polychroniadis, and M. G. Kanatzidis, "Cubic agpbmsbte2+ m: Bulk thermoelectric materials with high figure of merit," *Science*, vol. 303, no. 5659, pp. 818–821, 2004.

[16] C. J. Vineis, A. Shakouri, A. Majumdar, and M. G. Kanatzidis, "Nanostructured thermoelectrics: big efficiency gains from small features," *Advanced Materials*, vol. 22, no. 36, pp. 3970–3980, 2010.

[17] M. G. Kanatzidis, "Nanostructured thermoelectrics: The new paradigm?," *Chemistry of Materials*, vol. 22, no. 3, pp. 648–659, 2009.

[18] M. S. Dresselhaus, G. Chen, M. Y. Tang, R. Yang, H. Lee, D. Wang, Z. Ren, J.-P. Fleurial, and P. Gogna, "New directions for low-dimensional thermoelectric materials," *Advanced Materials*, vol. 19, no. 8, pp. 1043–1053, 2007.

[19] A. Minnich, M. Dresselhaus, Z. Ren, and G. Chen, "Bulk nanostructured thermoelectric materials: current research and future prospects," *Energy & Environmental Science*, vol. 2, no. 5, pp. 466–479, 2009.

[20] A. Shakouri, "Recent developments in semiconductor thermoelectric physics and materials," *Materials Research*, vol. 41, no. 1, p. 399, 2011.

[21] D. G. Cahill, W. K. Ford, K. E. Goodson, G. D. Mahan, A. Majumdar, H. J. Maris, R. Merlin, and S. R. Phillpot, "Nanoscale thermal transport," *Journal of Applied Physics*, vol. 93, no. 2, pp. 793–818, 2003.

[22] G. Chen, *Nanoscale energy transport and conversion: a parallel treatment of electrons, molecules, phonons, and photons.* Oxford University Press, USA, 2005.

[23] Y. Ju and K. Goodson, "Phonon scattering in silicon films with thickness of order 100 nm," *Applied Physics Letters*, vol. 74, no. 20, pp. 3005–3007, 1999.

[24] K. Esfarjani, G. Chen, and H. T. Stokes, "Heat transport in silicon from first-principles calculations," *Phys. Rev. B*, vol. 84, p. 085204, Aug 2011. [Online]. Available: http://link.aps.org/doi/10.1103/PhysRevB.84.085204

[25] Y. K. Koh and D. G. Cahill, "Frequency dependence of the thermal conductivity of semiconductor alloys," *Phys. Rev. B*, vol. 76, p. 075207, Aug 2007. [Online]. Available: http://link.aps.org/doi/10.1103/PhysRevB.76.075207

[26] A. J. Minnich, J. A. Johnson, A. J. Schmidt, K. Esfarjani, M. S. Dresselhaus, K. A. Nelson, and G. Chen, "Thermal conductivity spectroscopy technique to measure phonon mean free paths," *Phys. Rev. Lett.*, vol. 107, p. 095901, Aug 2011. [Online]. Available: http://link.aps.org/doi/10.1103/PhysRevLett.107.095901

[27] K. T. Regner, D. P. Sellan, Z. Su, C. H. Amon, A. J. McGaughey, and J. A. Malen, "Broadband phonon mean free path contributions to thermal conductivity measured using frequency domain thermoreflectance," *Nature communications*, vol. 4, p. 1640, 2013.

[28] M. Fischetti, "Effect of the electron-plasmon interaction on the electron mobility in silicon," *Physical Review B*, vol. 44, no. 11, p. 5527, 1991.

[29] J. Ma and S. Sinha, "Thermoelectric properties of highly doped n-type polysilicon inverse opals," *Journal of Applied Physics*, vol. 112, no. 7, pp. 073 719–073 719, 2012.

[30] H. Casimir, "Note on the conduction of heat in crystals," *Physica*, vol. 5, no. 6, pp. 495 – 500, 1938. [Online]. Available: http://www.sciencedirect.com/science/article/pii/S0031891438801622

[31] A. McConnell and K. E. Goodson, "Thermal conduction in silicon micro-and nanostructures," *Annual review of heat transfer*, vol. 14, no. 14, 2005.

[32] A. I. Boukai, Y. Bunimovich, J. Tahir-Kheli, J.-K. Yu, W. A. Goddard Iii, and J. R. Heath, "Silicon nanowires as efficient thermoelectric materials," *Nature*, vol. 451, no. 7175, pp. 168–171, 2008.

[33] D. Li, Y. Wu, P. Kim, L. Shi, P. Yang, and A. Majumdar, "Thermal conductivity of individual silicon nanowires," *Applied Physics Letters*, vol. 83, no. 14, pp. 2934–2936, 2003.

[34] J. Lim, K. Hippalgaonkar, S. C. Andrews, A. Majumdar, and P. Yang, "Quantifying surface roughness effects on phonon transport in silicon nanowires," *Nano letters*, vol. 12, no. 5, pp. 2475–2482, 2012.

[35] J. Tang, H.-T. Wang, D. H. Lee, M. Fardy, Z. Huo, T. P. Russell, and P. Yang, "Holey silicon as an efficient thermoelectric material," *Nano letters*, vol. 10, no. 10, pp. 4279–4283, 2010.

[36] J.-K. Yu, S. Mitrovic, D. Tham, J. Varghese, and J. R. Heath, "Reduction of thermal conductivity in phononic nanomesh structures," *Nature Nanotechnology*, vol. 5, no. 10, pp. 718–721, 2010.

[37] P. E. Hopkins, C. M. Reinke, M. F. Su, R. H. Olsson III, E. A. Shaner, Z. C. Leseman, J. R. Serrano, L. M. Phinney, and I. El-Kady, "Reduction in the thermal conductivity of single crystalline silicon by phononic crystal patterning," *Nano letters*, vol. 11, no. 1, pp. 107–112, 2010.

[38] P. G. Murphy and J. E. Moore, "Coherent phonon scattering effects on thermal transport in thin semiconductor nanowires," *Phys. Rev. B*, vol. 76, p. 155313, Oct 2007. [Online]. Available: http://link.aps.org/doi/10.1103/PhysRevB.76.155313

[39] D. Donadio and G. Galli, "Atomistic simulations of heat transport in silicon nanowires," *Physical review letters*, vol. 102, no. 19, p. 195901, 2009.

[40] P. Martin, Z. Aksamija, E. Pop, and U. Ravaioli, "Impact of phonon-surface roughness scattering on thermal conductivity of thin si nanowires," *Physical review letters*, vol. 102, no. 12, p. 125503, 2009.

[41] D. H. Santamore and M. C. Cross, "Effect of phonon scattering by surface roughness on the universal thermal conductance," *Phys. Rev. Lett.*, vol. 87, p. 115502, Aug 2001. [Online]. Available: http://link.aps.org/doi/10.1103/PhysRevLett.87.115502

[42] D. H. Santamore and M. C. Cross, "Effect of surface roughness on the universal thermal conductance," *Phys. Rev. B*, vol. 63, p. 184306, Apr 2001. [Online]. Available: http://link.aps.org/doi/10.1103/PhysRevB.63.184306

[43] Z. Aksamija and I. Knezevic, "Anisotropy and boundary scattering in the lattice thermal conductivity of silicon nanomembranes," *Phys. Rev. B*, vol. 82, p. 045319, Jul 2010. [Online]. Available: http://link.aps.org/doi/10.1103/PhysRevB.82.045319

[44] Y. He and G. Galli, "Microscopic origin of the reduced thermal conductivity of silicon nanowires," *Physical Review Letters*, vol. 108, no. 21, p. 215901, 2012.

[45] J. Carrete, L. J. Gallego, L. M. Varela, and N. Mingo, "Surface roughness and thermal conductivity of semiconductor nanowires: Going below the Casimir limit," *Phys. Rev. B*, vol. 84, p. 075403, Aug 2011.

[46] M. Luisier, "Investigation of thermal transport degradation in rough si nanowires," *Journal of Applied Physics*, vol. 110, no. 7, p. 074510, 2011.

[47] T. Markussen, A.-P. Jauho, and M. Brandbyge, "Electron and phonon transport in silicon nanowires: Atomistic approach to thermoelectric properties," *Phys. Rev. B*, vol. 79, p. 035415, Jan 2009. [Online]. Available: http://link.aps.org/doi/10.1103/PhysRevB.79.035415

[48] M. Kazan, G. Guisbiers, S. Pereira, M. R. Correia, P. Masri, A. Bruyant, S. Volz, and P. Royer, "Thermal conductivity of silicon bulk and nanowires: Effects of isotopic composition, phonon confinement, and surface roughness," *Journal of Applied Physics*, vol. 107, no. 8, p. 083503, 2010.

[49] P. Klemens, "Thermal conductivity and lattice vibrational modes," *Solid state physics*, vol. 7, pp. 1–98, 1958.

[50] P. M. Morse and K. Ingard, "Theoretical acoustics," *Princeton University Press, 949p*, vol. 4, p. 150, 1968.

[51] P. Mello, P. Pereyra, and N. Kumar, "Macroscopic approach to multichannel disordered conductors," *Annals of Physics*, vol. 181, no. 2, pp. 290 – 317, 1988. [Online]. Available: http://www.sciencedirect.com/science/article/pii/0003491688901698

[52] C. Herring, "Theory of the thermoelectric power of semiconductors," *Physical Review*, vol. 96, no. 5, p. 1163, 1954.

[53] G. Mahan and L. Woods, "Multilayer thermionic refrigeration," *Physical review letters*, vol. 80, no. 18, pp. 4016–4019, 1998.

[54] A. Shakouri, "Thermoelectric, thermionic and thermophotovoltaic energy conversion," in *Thermoelectrics, 2005. ICT 2005. 24th International Conference on*. IEEE, 2005, pp. 507–512.

[55] A. Shakouri and J. E. Bowers, "Heterostructure integrated thermionic coolers," *Applied Physics Letters*, vol. 71, no. 9, pp. 1234–1236, 1997.

[56] H. Frederikse, "Thermoelectric power of germanium below room temperature," *Physical Review*, vol. 92, no. 2, p. 248, 1953.

[57] L. Weber and E. Gmelin, "Transport properties of silicon," *Applied Physics A*, vol. 53, no. 2, pp. 136–140, 1991.

[58] J. Sadhu and S. Sinha, "Room-temperature phonon boundary scattering below the casimir limit," *Physical Review B*, vol. 84, no. 11, p. 115450, 2011.

[59] J. Sadhu, M. Seong, and S. Sinha, "Partially coherent phonon transport in two-dimensionally rough nanowires," *Journal of Computational Electronics*, vol. 11, no. 1, pp. 1–7, 2012.

[60] W. A. Harrison, *Electronic structure and the properties of solids: the physics of the chemical bond*. Courier Dover Publications, 2012.

[61] R. E. Peierls, *Quantum theory of solids*. Oxford University Press, 1955.

[62] J. Zou and A. Balandin, "Phonon heat conduction in a semiconductor nanowire," *Journal of Applied Physics*, vol. 89, no. 5, pp. 2932–2938, 2001. [Online]. Available: http://link.aip.org/link/?JAP/89/2932/1

[63] S. Yu, K. W. Kim, M. A. Stroscio, and G. J. Iafrate, "Electron˘acoustic-phonon scattering rates in cylindrical quantum wires," *Phys. Rev. B*, vol. 51, pp. 4695–4698, Feb 1995. [Online]. Available: http://link.aps.org/doi/10.1103/PhysRevB.51.4695

[64] R. P. Feynman and A. R. Hibbs, *Quantum mechanics and path integrals: Emended edition*. DoverPublications. com, 2012.

[65] F. Bass, V. Freulicher, and I. Fuks, "Propagation in statistically irregular waveguides–part i: Average field," *Antennas and Propagation, IEEE Transactions on*, vol. 22, no. 2, pp. 278–288, 1974.

[66] T. R. Kirkpatrick, "Localization of acoustic waves," *Phys. Rev. B*, vol. 31, pp. 5746–5755, May 1985. [Online]. Available: http://link.aps.org/doi/10.1103/PhysRevB.31.5746

[67] I. Savić, N. Mingo, and D. A. Stewart, "Phonon transport in isotope-disordered carbon and boron-nitride nanotubes: Is localization observable?" *Phys. Rev. Lett.*, vol. 101, p. 165502, Oct 2008. [Online]. Available: http://link.aps.org/doi/10.1103/PhysRevLett.101.165502

[68] M. G. Holland, "Analysis of lattice thermal conductivity," *Phys. Rev.*, vol. 132, pp. 2461–2471, Dec 1963. [Online]. Available: http://link.aps.org/doi/10.1103/PhysRev.132.2461

[69] S. Ito, "Analysis of scalar wave scattering from slightly rough random surfaces: A multiple scattering theory," *Radio Sci.*, vol. 20, no. 1, pp. 1–12, 1985.

[70] V. Schmidt, H. Riel, S. Senz, S. Karg, W. Riess, and U. Gösele, "Realization of a silicon nanowire vertical surround-gate field-effect transistor," *Small*, vol. 2, no. 1, pp. 85–88, 2006.

[71] B. Tian, X. Zheng, T. J. Kempa, Y. Fang, N. Yu, G. Yu, J. Huang, and C. M. Lieber, "Coaxial silicon nanowires as solar cells and nanoelectronic power sources," *Nature*, vol. 449, no. 7164, pp. 885–889, 2007.

[72] M. D. Kelzenberg, D. B. Turner-Evans, B. M. Kayes, M. A. Filler, M. C. Putnam, N. S. Lewis, and H. A. Atwater, "Photovoltaic measurements in single-nanowire silicon solar cells," *Nano letters*, vol. 8, no. 2, pp. 710–714, 2008.

[73] K.-Q. Peng and S.-T. Lee, "Silicon nanowires for photovoltaic solar energy conversion," *Advanced Materials*, vol. 23, no. 2, pp. 198–215, 2011.

[74] C. K. Chan, H. Peng, G. Liu, K. McIlwrath, X. F. Zhang, R. A. Huggins, and Y. Cui, "High-performance lithium battery anodes using silicon nanowires," *Nature nanotechnology*, vol. 3, no. 1, pp. 31–35, 2007.

[75] K. Peng, J. Jie, W. Zhang, and S.-T. Lee, "Silicon nanowires for rechargeable lithium-ion battery anodes," *Applied Physics Letters*, vol. 93, no. 3, pp. 033 105–033 105, 2008.

[76] Z. Huang, N. Geyer, P. Werner, J. De Boor, and U. Gösele, "Metal-assisted chemical etching of silicon: A review," *Advanced materials*, vol. 23, no. 2, pp. 285–308, 2011.

[77] X. Li, "Metal assisted chemical etching for high aspect ratio nanostructures: A review of characteristics and applications in photovoltaics," *Current Opinion in Solid State and Materials Science*, vol. 16, no. 2, pp. 71–81, 2012.

[78] W. Chern, K. Hsu, I. S. Chun, B. P. d. Azeredo, N. Ahmed, K.-H. Kim, J.-m. Zuo, N. Fang, P. Ferreira, and X. Li, "Nonlithographic patterning and metal-assisted chemical etching for manufacturing of tunable light-emitting silicon nanowire arrays," *Nano letters*, vol. 10, no. 5, pp. 1582–1588, 2010.

[79] H. Masuda and K. Fukuda, "Ordered metal nanohole arrays made by a two-step," *Science*, vol. 268, pp. 1466–1468, 1995.

[80] K. Peng, M. Zhang, A. Lu, N.-B. Wong, R. Zhang, and S.-T. Lee, "Ordered silicon nanowire arrays via nanosphere lithography and metal-induced etching," *Applied physics letters*, vol. 90, no. 16, pp. 163 123–163 123, 2007.

[81] B. Azeredo, J. Sadhu, J. Ma, K. Jacobs, J. Kim, K. Lee, J. Eraker, X. Li, S. Sinha, N. Fang et al., "Silicon nanowires with controlled sidewall profile and roughness fabricated by thin-film dewetting and metal-assisted chemical etching," *Nanotechnology*, vol. 24, no. 22, p. 225305, 2013.

[82] J. P. Feser, J. S. Sadhu, B. P. Azeredo, K. H. Hsu, J. Ma, J. Kim, M. Seong, N. X. Fang, X. Li, P. M. Ferreira et al., "Thermal conductivity of silicon nanowire arrays with controlled roughness," *Journal of Applied Physics*, vol. 112, no. 11, pp. 114 306–114 306, 2012.

[83] S. Cruz, A. Hönig-dOrville, and J. Müller, "Fabrication and optimization of porous silicon substrates for diffusion membrane applications," *Journal of the Electrochemical Society*, vol. 152, no. 6, pp. 418–424, 2005.

[84] M. Schade, N. Geyer, B. Fuhrmann, F. Heyroth, P. Werner, and H. S. Leipner, "High-resolution analytical electron microscopy of silicon nanostructures," *physica status solidi (c)*, vol. 6, no. 3, pp. 690–695, 2009.

[85] A. I. Hochbaum, D. Gargas, Y. J. Hwang, and P. Yang, "Single crystalline mesoporous silicon nanowires," *Nano letters*, vol. 9, no. 10, pp. 3550–3554, 2009.

[86] K. Balasundaram, J. S. Sadhu, J. C. Shin, B. Azeredo, D. Chanda, M. Malik, K. Hsu, J. A. Rogers, P. Ferreira, S. Sinha et al., "Porosity control in metal-assisted chemical etching of degenerately doped silicon nanowires," *Nanotechnology*, vol. 23, no. 30, p. 305304, 2012.

[87] M. Seong, J. Sadhu, J. Ma, M. Ghossoub, and S. Sinha, "Modeling and theoretical efficiency of a silicon nanowire based thermoelectric junction with area enhancement," *Journal of Applied Physics*, vol. 111, no. 12, pp. 124 319–124 319, 2012.

[88] T. Harman, "Special techniques for measurement of thermoelectric properties," *Journal of Applied Physics*, vol. 29, no. 9, pp. 1373–1374, 1958.

[89] R. Singh, Z. Bian, A. Shakouri, G. Zeng, J.-H. Bahk, J. E. Bowers, J. M. Zide, and A. C. Gossard, "Direct measurement of thin-film thermoelectric figure of merit," *Applied Physics Letters*, vol. 94, no. 21, pp. 212 508–212 508, 2009.

[90] Z. Bian, Y. Zhang, H. Schmidt, and A. Shakouri, "Thin film zt characterization using transient harman technique," in *Thermoelectrics, 2005. ICT 2005. 24th International Conference on.* IEEE, 2005, pp. 76–78.

[91] E. E. Castillo, C. L. Hapenciuc, and T. Borca-Tasciuc, "Thermoelectric characterization by transient harman method under nonideal contact and boundary conditions," *Review of Scientific Instruments*, vol. 81, no. 4, pp. 044 902–044 902, 2010.

[92] B. Yang, J. Liu, K. Wang, and G. Chen, "Simultaneous measurements of seebeck coefficient and thermal conductivity across superlattice," *Applied Physics Letters*, vol. 80, no. 10, pp. 1758–1760, 2002.

[93] D. G. Cahill, "Thermal conductivity measurement from 30 to 750 k: the 3ω method," *Review of Scientific Instruments*, vol. 61, no. 2, pp. 802–808, 1990.

[94] A. I. Persson, Y. K. Koh, D. G. Cahill, L. Samuelson, and H. Linke, "Thermal conductance of inas nanowire composites," *Nano letters*, vol. 9, no. 12, pp. 4484–4488, 2009.

[95] M. Ghossoub, K. Valavala, M. Seong, B. Azeredo, K. Hsu, J. Sadhu, P. Singh, and S. Sinha, "Spectral phonon scattering from sub-10 nm surface roughness wavelengths in metal-assisted chemically etched si nanowires," *Nano letters*, vol. 13, no. 4, pp. 1564–1571, 2013.

[96] D. G. Cahill, "Analysis of heat flow in layered structures for time-domain thermoreflectance," *Review of scientific instruments*, vol. 75, no. 12, pp. 5119–5122, 2004.

[97] L. Shi, D. LI, C. Yu, W. Jang, D. Kim, Z. Yao, P. Kim, and A. Majumdar, "Measuring thermal and thermoelectric properties of one-dimensional nanostructures using a microfabricated device," *Journal of heat transfer*, vol. 125, no. 5, pp. 881–888, 2003.

[98] J. P. Feser, "Scalable routes to efficient thermoelectric materials," Ph.D. dissertation, 2010.

[99] V. Schmidt, J. Wittemann, and U. Gosele, "Growth, thermodynamics, and electrical properties of silicon nanowires," *Chemical reviews*, vol. 110, no. 1, pp. 361–388, 2010.

[100] S. M. Sze and K. K. Ng, *Physics of semiconductor devices*. Wiley. com, 2006.

[101] P. Pichanusakorn and P. Bandaru, "Nanostructured thermoelectrics," *Materials Science and Engineering: R: Reports*, vol. 67, no. 2, pp. 19–63, 2010.

[102] E. Conwell and V. Weisskopf, "Theory of impurity scattering in semiconductors," *Physical Review*, vol. 77, no. 3, p. 388, 1950.

[103] R. Dingle, "The electrical conductivity of thin wires," *Proceedings of the Royal Society of London. Series A. Mathematical and Physical Sciences*, vol. 201, no. 1067, pp. 545–560, 1950.

[104] P. Klemens, "Theory of phonon drag thermopower," in *Thermoelectrics, 1996., Fifteenth International Conference on.* IEEE, 1996, pp. 206–208.

[105] T. Geballe, C. Herring, and J. Kunzler, "Phonon-drag thermomagnetic effects in n-germanium," *Journal of Physics and Chemistry of Solids*, vol. 8, pp. 347–353, 1959.

[106] P. Price, "Theory of transport effects in semiconductors: The nernst coefficient, and its relation to thermoelectric power," *Physical Review*, vol. 102, no. 5, p. 1245, 1956.

[107] K. D. Cole, *Heat conduction using Green's functions.* CRC Press, 2011.